DESIGN METHOD TO REPAIR CORROSION-DAMAGED OFFSHORE STEEL STRUCTURES UNDER WATER

CHEN Xiao

DESIGN METHOD TO REPAIR CORROSION-DAMAGED OFFSHORE STEEL STRUCTURES UNDER WATER

CHEN Xiao

Department of Civil Engineering

Nagoya University

2011

ACKNOWLEDGEMENTS

Many wonderful people have supported me on this study. Firstly, I am deeply grateful to my academic supervisor Professor Yoshito Itoh for guiding me and encouraging me along the research. I still remember that when I came to Nagoya University, he told me that research is very difficult but fun. I am happy that I overcame some difficulties under his supervision and yes, he was right, the research is interesting, and I love this study.

During my stay in Japan, Associate Professor Yasuo Kitane provided many valuable discussions and advice on my study and daily life, and I learned a lot from him. His various supports are greatly appreciated.

I wish to thank Assistant Professor Mikihito Hirohata for the constructive comments on this thesis. Thanks also go to Professor Katashi Fujii of Hiroshima University for the measurement data of corroded sheet piles used in this study, and Professor Hanbin Ge of Meijo University, Associate Professor Akira Kasai of Kumamoto University, Professor Fusheng Zhu, and Professor Bin Liu of Northeastern University in China for encouragement when I study in Nagoya University.

I would like to thank the members of my dissertation committee, Professor Yoshito Itoh, Professor Kazuo Tateishi, Professor Makoto Obata, Associate Professor Minoru Kunieda, and Associate Professor Yasuo Kitane. Their careful review and constructive comments on this work are highly appreciated.

This study would not be possible without the scholarship from the China Scholarship Council (CSC) under The Postgraduates' Oversea Study Program for High-Level University Building (file No. 2008608035). I also wish to thank Nagoya University for the tuition waiver during my doctoral program study.

I want to thank all the student members, both current and former ones, in Itoh Laboratory, Dr. Naohiko Watanabe, Dr. Xi Chen, Dr. Paramashanti, Dr. Haeyong Kim, Mr. Kazuo Furunishi, Ms. Kulkarni Nishigandha, Mr. Zhirong Lin, Mr. Keisuke Kaneko, Mr. Yuuki Sugiura, Mr. Akihiro Hosoi, Mr. Thanh Huu Le, Mr. Seiha Ung, Mr. Seiji Itoh, Mr. Shinya Ohkura, Mr. Tatsuya Mori, and Mr. Koji Kurita for enjoyable experiences shared together. Sincere thanks go to Mrs. Makoto Iwanaga for the kind assistance in the documentary works during my study.

I am indebted to my parents, parents-in-law, and younger brother for their selfless devotion to helping me. My wife Dan Zheng showed me love, optimism, and understanding all the way in times of happiness as well as sorrow. My grandfather, who passed away just before I came to Japan, gave me a lot of care when I was in China. This thesis is dedicated to them.

TABLE OF CONTENTS

LIST OF TABLES

LIST OF FIGURES

ABSTRACT

This dissertation presents a study on the design method to repair corrosion-damaged steel structures in offshore and port environments, with particular focus on underwater application. Two repair techniques are examined in this study. One is steel patch plate welding, and the other is carbon fiber reinforced polymer (CFRP) bonding.

Mechanical properties of underwater wet fillet welds used in the welding repair were investigated through static tension tests on forty-six double-lapped fillet welded specimens with various weld assemblies. Weld profiles, hardness distribution, and weld microstructures were also carefully examined. It was found that underwater fillet welds, compared with their counterpart in-air ones, had a strength increase from 6.9% to 41% depending on different weld assemblies and a ductility decrease about 50% for the most weld assemblies. In addition, underwater welds showed considerable large hardness in heat affected zone (HAZ).

Based on the experimental findings, two finite element (FE) modeling methods were proposed to facilitate numerical analysis on mechanical behavior of underwater wet fillet welds and the repaired steel structures using patch plate welding. Taking advantage of the proposed weld model, the current design method to repair the corrosion-damaged pipe piles under axial compressive loads was evaluated numerically through forty-eight analyses. It was found that the current calculation on patch thickness according to the Japanese design manual could not recover the structural performance due to the underestimation of the load share ratio of patch plates. An accurate calculation of patch thickness considering the stiffness of fillet welds was proposed, and a structurally favorable welding pattern, which has many patch slits, was pointed out.

Moreover, a set of FE analysis and the complementary analytical study were carried out to investigate the repaired performance of pipe piles repaired by patch welding considering the effect of the existing loads on the structural performance and on the repair design. A minimum patch thickness that recovers both the initial stiffness and the design strength of the corrosion-damaged pipe piles under different existing loads was obtained. By integrating all the findings, the design method towards an efficient repair using underwater wet welding was then proposed.

In this study, an innovative method to repair offshore steel structures, CFRP bonding using underwater epoxy as adhesive, was investigated experimentally. Sixteen CFRP strand sheet-

bonded steel plates with a uniform thickness reduction in steel were tested in tension and compression. Four sets of epoxy coupons were tested in different curing times to examine the curing effect on mechanical properties of underwater epoxy and consequently on the structural behavior of CFRP-bonded steel plates.

It was found that the underwater epoxy used in this study was not appropriate due to long curing time and small initial stiffness and strength. In spite of this, the repaired stiffness and the yielding loads of CFRP-bonded steel plates could be recovered to 0.90 and 0.95 times, respectively, of the design values when one CFRP layer is used. In addition, the second CFRP layer was found to be not effective in the repair when the bond provided by the epoxy adhesive was weak. Some suggestions were proposed to use this repair method in practice.

CHAPTER 1
INTRODUCTION

1.1 GENERAL

Offshore structures are essential parts of civil infrastructures. With the exploitation of energy resources pushing into the seas, engineering structures for oil and gas exploration, production, processing, and transportation are common scene today on ocean waters. Coastal and port structures serve as forts from natural disasters such as floods and tsunami, and they are the hubs for international as well as national trade. It is reported that the total volume of cargo handled in coastal ports is about 3.17 billion tons in Japan in 2004[1.1)]; while it is reported to be 4.75 and 3.43 billon tons in China and European Union (27 countries), respectively, in 2009[1.2), 1.3)]; and the volume of worldwide international oceanborne cargo reached more than 8 billion tons in 2007, and during the past decades, the annual average growth rate was about 3 percent[1.4)].

Because of the severe corrosive environment encountered, offshore, coastal and port structures in the sea areas are plagued by deterioration of materials and degradation of structural performance. It is reported that the unprotected steel in the splash zone can be corroded at a rate of about 0.3 mm/year[1.5)], and a higher corrosion rate can be expected depending on different locations, structural type, water temperature, wave condition, etc[1.6)]. Particularly in Japan, a large amount of offshore and port structures were built during 1970s to 1980s, most of them have been working for nearly 40 years, and their corrosion problem is very severe.

Fig. 1.1 shows two photos, taken in 2009, of corrosion-damaged steel pipe piles at an offshore pier in Japan, which was built in 1971. At the time of construction, no corrosion-proof measure was employed and the raw steel was directly exposed to seawater. The corrosion has been continuing for nearly 40 years. From the late 1980s, the cathodic protection for steel structures in the seawater zone, and the coating protection for those in the splash zone and the tidal zone were gradually employed in Japanese offshore and port steel strucutres[1.7)]. To confront severe corrosion problem, some costly strategies are employed as an example in the construction project of the D-runway of the Tokyo International Airport. In this project, stainless steel is used in the

pipe piles at the splash zone and the tidal zone to protect them from seawater corrosion. Fig. 1.2 shows photos of the application of stainless steel in the project.

Fig. 1.1 Corrosion-damaged pipe piles at an offshore pier

(a) Aerial view of D-runway

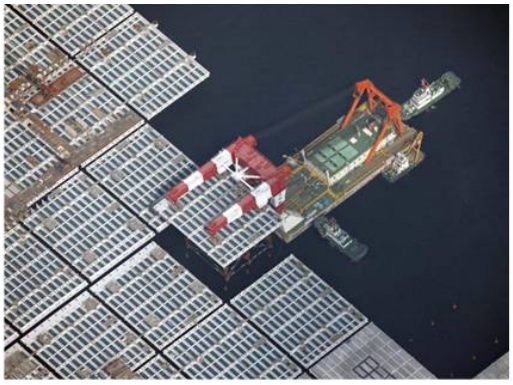

(b) Assembly of steel jacket

(c) Transport of steel jacket

(d) Pipe piles covered with stainless steel

Fig. 1.2 Application of stainless steel in the offshore steel structures*

*Source: The website of The Tokyo International Airport Runway D Exterior Construction: http://www.haneda-d.jp/

As the seawater corrosion of offshore steel structures is a worldwide issue, other countries are also suffering from this engineering problem. Take China for example, the situation is not better although the large amount of investment from the government to the construction of offshore and port infrastructures initialized mainly from the late 1980s. It is specified in the Chinese Industry Standard that the annual corrosion rate for carbon steel at the splash zone is 0.2~0.3 mm/year for shielded sea areas and 0.4~0.5 mm/year for unshielded ones, and the corrosion rate at the tidal zone is specified to be 0.12 mm/year[1.8)]. With these corrosion rates, it is very challenging for engineers because a rapid growth of international cargo transportation of China in recent two decades demands offshore and port structures to be not only structurally safe but also functionally sound during their expected long service time, i.e., 100 years, although they were not designed and constructed according to the modern standards.

Many organizations, including international, national, as well as regional, are dedicating to corrosion survey and the corrosion countermeasures for offshore and port structures, such as International Navigation Association (PIANC), Maritime Navigation Commission (MarCom), The International Association of Ports and Harbors (IAPH), The International Council of Marine Industry Association (ICOMIA), and the Port and Harbor Research Institute (PARI) in Japan. These organizations prompt the technical advancement of offshore and port engineering by conducting various surveys and tests both in-field and at laboratory. It is noted that an oceanic field exposure test of 19.5 years was conducted by the committee of structural engineering, Japan Society of Civil Engineers (JSCE), and the long term corrosion features of steel angle members in the seawater environment were captured and reported[1.9), 1.10)]. Fig. 1.3 shows the facilities of the long term field test in the seawater.

Fig. 1.3 Facilities of the long-term (19.5 years) field exposure test[1.10)]

Considering that corrosion damage of offshore and port structures is inevitable, and in the cases the closure of the offshore and port areas due to the concern of structural safety or service functions may cause severe financial penalties. A life cycle management (LCM) strategy was introduced to offshore and port structures since the late 1980s. The LCM contributes to a realistic approach of maintenance policy, including decision-making, planning, budgeting, and funding of inspection and repair activities during the life-time of structures[1.11)].

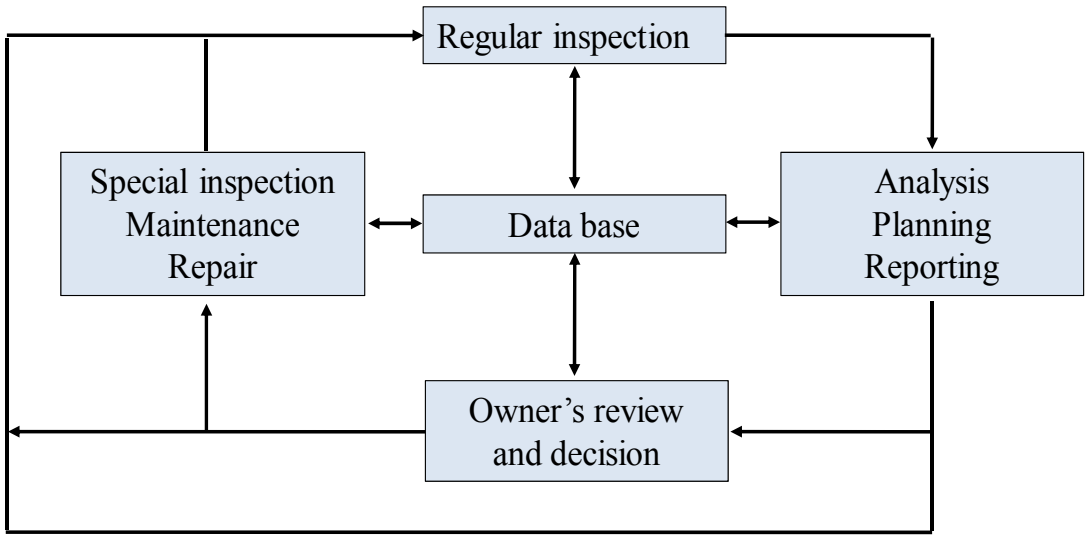

Fig. 1.4 Regular key tasks of LCM[1.11)]

Fig. 1.4 shows regular key tasks of LCM. In this figure, the Data base is shown in the center as hub and memory of the system. All information gathered and actions carried out are reported to the Database, and all analyses, decisions and activities made in the LCM context are based on information drawn therefrom. Starting from the top of the figure, the box indicates a Regular inspection which is carried out periodically. Findings from the inspection are analyzed and possible necessary remedial actions are planned. If the analysis concludes that no specific actions are needed, the cyclic process can continue via the lower line in the diagram without involving the Owner, upwards to the left and return to the next Regular inspection after the selected period. If certain problems are found, a report will be prepared to the Owner and passed on for his review and decision. This decision may be not to take any special action at this time, whereafter the cycle will continue to the left and upwards towards the next Regular inspection.

When a repair work is regarded to be necessary, for example, to maintain the required structural performance of an offshore or port structure, there are several repair methods available. More specifically, to repair corrosion-damaged steel pipe piles and steel sheet piles, two common methods are used in the repair: one is concrete jacketing, and the other is steel patch plate welding. Compared with the former, the patch welding is more competitive in terms of working time. The patch welding can be further classified into two categories regarding whether welding procedure is carried out in dry or wet environment. When underwater dry welding is applied, a chamber system for welders must be built so that welding work can be carried out in a dry condition as the same as those on land. However, building suitable chambers for different structural types increases the cost and working time, especially when there are many structures to be repaired, such as pipe piles of the pier as shown in Fig. 1.1. In this case, the chamber has to be built, disassembled, moved, and rebuilt for different piles, and more importantly, for some piles, there may be no much space to build a chamber.

To solve these problems associated with the dry welding repair, a wet welding, which is originated from the repair and salvage of ships, is considered to be satisfactory because it can be mobilized quickly and completed easily in areas where construction of a dry chamber for welders is impossible. Therefore, the repair cost can be significantly reduced. However, there are still some technical concerns when employing underwater wet welding. Because underwater wet welds are more susceptible to defects, such as pores, cracks, inclusions, etc. In addition, mechanical properties of wet welds are not fully understood yet, resulting in the substantially conservative application of this technique. Because of these concerns, the underwater wet welding repair has long been regarded just as a temporary fix method[1.12)]. With the great demand for the repair of corrosion-damaged structures with low cost, the underwater wet welding gains more popularity in the recent decades, and the mechanical properties of wet welds therefore have to be understood in order to use this repair technique with confidence.

With the clear understanding of the mechanical properties of wet welds, the welding repair design is possible by following the available design manual. Fig. 1.5 shows a general procedure to repair a corrosion-damaged pipe pile by welding patch plates over the base steel. All the problems regarding the welding repair work, however, are not solved completely, and there are some pending issues to be examined towards an efficient repair design. Because the provisions on welding patch repair in the current design manual in Japan is based on tests on forty-six fillet

welded specimens conducted in 1985 as presented in the manual of the previous version[1.13)], considering the rapid technical advancement in underwater wet welding in recent decades, the specification needs to be re-examined through the updated test results.

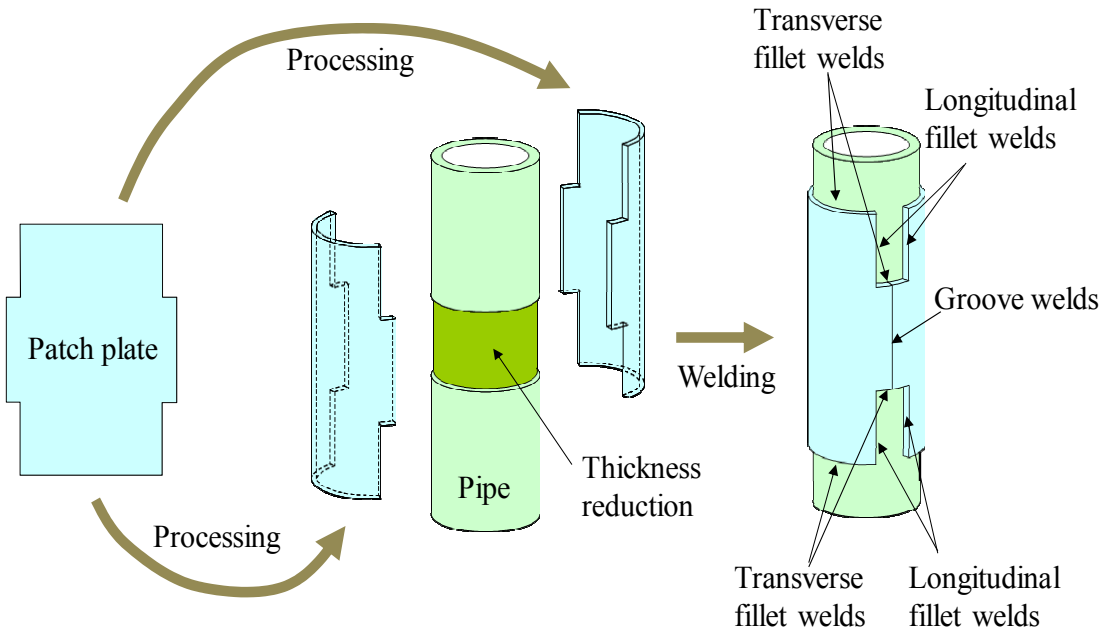

Fig. 1.5 A general procedure of welding patch repair

In addition, the design manual does not specify how and why the welding patch plates should be prepared to achieve satisfactory repair, which means that any patch pattern is acceptable as long as the total weld length meets the requirement. This ambiguity in the design manual pushes the engineers to a difficult position, and they have to determine the repair design basically counting on their experience, and sometimes even their preferences.

Moreover, to achieve cost-effective functionality and quality of offshore and port structures during their life cycle, it is necessary to evaluate the structural performance not only in the deteriorating phase, but also in the phase after repair. The repaired performance of welding patch repair is not quite understood especially taking into account of the existing loads applied to the structures before repair. In addition, how these existing loads would affect the repair method and the consequent structural performance has to be investigated.

Based on the discussions above, this study firstly presents a thorough experimental work on the mechanical properties of underwater fillet welds, which are used in the wet welding repair; secondly, two FE modeling methods are proposed according to the test results on fillet welds; and then, a comparative numerical study is presented on welding patch patterns using the proposed weld model in the FE analysis; and following with a series of analytical study, a cost-effective design method using welding patch repair is proposed, and the structural performance after repair is also addressed considering the existing loads; finally, the design method using underwater wet welding to repair corrosion-damaged pipe piles is proposed.

In addition to underwater welding repair, an innovative repair method using CFRP with underwater epoxy as adhesive is examined experimentally through sixteen CFRP-bonded steel plates. The study provides fundamental experimental results to apply this method in the practice.

1.2 THE-STATE-OF-THE-ART REVIEW

1.2.1 Properties of Underwater Wet Welds

Underwater wet welding repair of submerged steel structures in offshore and port environments is an economical and especially more time-independent procedure[1.14)]. In the past decades, many researchers were dedicating to improving the quality of wet welds, and trying to understand their metallurgical as well as mechanical properties. Compared with their counterpart in-air welding, underwater wet welding is not at all an easy task. Because the welding procedure is directly exposed to the surrounding seawater, the rapid cooling in water would harden and embrittle the molten weld metal, cause hydrogen-assisted cracking depending on the strength of the base steel and filler metal, and induce porosity in the weldment[1.15) ~ 1.22)]. In addition to these intrinsic drawbacks associated with underwater wet welding, the adverse welding environment of poor visibility and wave disturbance encountered by the underwater welders may also degrade the welding quality.

A thorough experimental study on the strength of underwater wet fillet welds was conducted in 1985 in Japan by Coastal Development Institute of Technology. Forty-six double-lapped fillet welded specimens were tested under tension, and the base steels were STK41 (now STK400) for pipe pile and SY30 (now SY295) for sheet pile specified in Japanese Industry Standard (JIS), and

two weld orientations were considered as longitudinal welds and transverse welds. Compared with the counterpart in-air welds, the underwater wet welds were found to[1.13)]:

1) have more irregular weld bead shapes and more welding defects, such as insufficient fusion at the root, and the undercut;
2) have a Vickers hardness close to 600 Hv at the boundary between weld deposit and base metal; and
3) exhibit a comparable weld strength to that of in-air welds with the average strength ratios of 0.81-1.30 and 0.93-1.18 for longitudinal welds and transverse welds, respectively.

As a result, it was specified in the repair design manual that the strength of underwater fillet welds is 80% of that of in-air welds[1.5), 1.13)]. The similar treatment posed to underwater welds can be found in other design manual, such as ANSI/AWS D3.6 specification[1.23)], where wet welds are classified as Class B welds, while Class A welds are specified to have quality comparable to that of welds made in a dry environment.

Over more than two decades, the underwater welding technique has been improving due to advances in the material science and the welding technology. The use of high performance electrodes results in better quality of underwater welds and hence improves their mechanical performance. The conclusions from the weld strength test carried out more than twenty years ago may not applicable to the current practice. Moreover, the underwater weld specimens in the original test were produced in a water pool filled with tap water instead of seawater, the welding environment was different from the one when repair work is performed on the actual offshore and port structures, which are usually exposed to the saline seawater. In addition, the old test only examined mechanical properties of wet welds in terms of strength, other properties such as ductility and force-displacement relationships are also important to understand their mechanical behavior. Regarding the above concerns, there is therefore great demand to update the experimental results and to provide more reliable and complete information on the mechanical properties of underwater wet welds used in the welding repair.

1.2.2 FE Analysis on Underwater Fillet Welds

FE analysis, also known as FE method, is a powerful numerical methodology extensively used in structural engineering, and it has great advantage in analyzing physical fields of structures, such as mechanical and thermal responses, especially when either the actual experimental study is time-consuming and costly, or the classical analytical solutions of the problem in the concern are almost impossible. Particularly, FE analysis is extremely efficient once the generalized model is created and validated, and the model can be used for parametric study, which is beyond the coverage of the limited experimental cases.

Although it can provide so many advantages, the FE analysis particularly focused on fillet welds made underwater is rarely reported. This may be because the modeling of fillet welds is rather difficult with the presence of local effects such as geometrical irregularities, residual stresses, material inhomogeneities and weld defects. More likely, the material properties of weld details are not readily available. This situation for in-air welds is better considering the material properties of weld deposit (DEPO) and the heat affected zone (HAZ) can be tested using tensile coupons extracted from the welds according to the test standards, such as JIS Z3111[1.24)]. However, when it comes to underwater welds, the tensile coupon tests would be, if not impossible, extremely expensive, because the extraction and the testing of coupons are rather difficult due to the small size of HAZ, which is the region mainly characterizing the properties of underwater welds. It is therefore necessary to find an alternative method to estimate the material properties of underwater welds according to the readily available information of weld materials.

Meanwhile, when the performance of the welding repaired structures is in the concern, it is usually assumed in the FE analysis that the welds in the structures are too strong to fail or to have nonlinear behavior[1.25), 1.26)]. This assumption is generally acceptable as long as the mechanical properties of welds are fully understood and the proper welding design procedure is followed. However, when these two premises are not satisfied with certainty, the ignorance of nonlinear behavior and the possible failure of welds is questionable, and in the worst case, it would cause the failure of the whole structure due to the poor weld design. Consequently, there is imperative demand to develop an effective as well as concise model to present the nonlinear behavior and to estimate the possible failure of the welds used in the repaired structures.

1.2.3 Design Method of Welding Repair

Basically, the design work to repair corrosion-damaged offshore and port structures follows the design manual issued by Coastal Development Institute of Technology in Japan[1.5)]. The current vision was issued in 2009 and the design concept was changed from allowable stress design to reliability based design. In addition to this change, specifically in welding repair, the discount rate of weld strength due to field welding was set to 10% in place of its previous value of 20%, consequently, weld strength of field underwater welding is specified as 70% of that of in-air shop welding, which was 60% in the previous manual[1.13)].

In addition to the questionable weld strength specified in the manual, the design method and some provisions need to be re-examined. Because the current design manual does not provide any guidance on the choice of welding patch patterns, there are many candidates to repair one structure. In addition, the determination of patch thickness is based on the load share ratio of patch plates, which is simply calculated as a ratio between patch thickness t_p and the summation of t_p and the residual thickness of the corrosion-damaged base steel t_r, i.e., $t_p/(t_p+t_r)$. However, the actual load share ratio is smaller than this calculation due to the deformation of fillet welds as well as patch plates at slits, and this overestimation of load share ratio in patch plates in the design would cause more loads to transfer to the corrosion-damaged base steel than expected, and consequently would lower the repair effect of structures.

Meanwhile, it is specified in the manual that the strength of transverse fillet welds is not expected when calculating a total length of fillet welds used in the repair. This provision needs to be verified considering that transverse welds are usually provided in the repair to seal patch plates and hence protect the damaged base steel from further corrosion. Furthermore, the effect of the existing loads and the residual load-carrying capacity of the corrosion-damaged base steel on the repair design and the structural performance after patch repair are not clarified yet, which impedes the complete assessment of life cycle performance of the structures.

It is hence essential to conduct a series of studies to answer the pending questions in the current design and accordingly to propose a more reliable and efficient design method using the welding patch repair.

1.2.4 CFRP for Underwater Repair

As an innovative method to repair corrosion-damaged offshore structures, CFRP bonding is gaining more and more attention in underwater application. CFRP has superior material properties, such as high stiffness, high strength, light weight, ease of handing and good corrosion resistance[1.27), 1.28)], and there are many successful examples using CFRP bonding to repair and retrofit structures[1.29) ~ 1.31)]. However, the repaired performance and the durability are reported to be adversely affected when CFRP bonding is used in the environment with large humidity or underwater[1.32) ~ 1.35)].

In spite of the noticed drawbacks, the CFRP bonding is still regarded to be a promising alternative to repair offshore structures when the conventional repair methods, for example, concrete jacketing and steel patch plate welding, could not be performed cost-effectively, especially when the Whole Life Cost (WLC) or Life Cycle Cost (LCC) has to be taken into account. Motivated by the imperative demand from offshore and port industry, some researchers studied the feasibility and the repair performance of CFRP-bonded concrete structures with emphasis to underwater application[1.36) ~ 1.38)], while there is only a few study reported the application of CFRP to repair steel structures underwater. It was found that the flexural stiffness and the load-carrying capacity of steel tubes warped and cured underwater cannot reach the values obtained in the in-air application[1.39)].

Because many offshore structures, such as oil platforms, are mainly constructed by steel members, the research on the underwater application of CFRP to repair steel structures is inadequate. Consequently, it is necessary to perform more studies to characterize the repair effectiveness and to possibly promote the application of this new technique through a proper design. Experimental investigation is essential to provide fundamental results and to verify the future numerical models and design calculations.

1.3 OBJECTIVES AND SCOPE

In recognition of the current research demand and necessity, the main objective of this study is devoted to fulfilling an efficient repair design method of corrosion-damaged offshore steel structures with particular attention paid to underwater application. The research work includes the

experimental investigation on mechanical properties of underwater wet welds, the numerical examination on pipe piles repaired by patch welding, the corresponding analytical derivation for design formulas. and a fundamental experimental study on mechanical behavior of CFRP-bonded steel plates by underwater epoxy.

More specifically, this study:

(1) quantifies and updates the strength and the ductility of underwater wet fillet welds used in the welding repair work,

(2) proposes a method to model wet fillet welds and a nonlinear weld model to analyze fillet welded structures using finite element method,

(3) evaluates the current design method on welding patch repair of steel pipe piles under compression,

(4) investigates the repaired performance of welding patched pipe piles considering the existing loads,

(5) proposes design formulas and a design method towards a more efficient repair using welding patches, and

(6) assesses the repair effect of CFRP-bonded steel plates using underwater epoxy as adhesive.

The thesis is organized as shown in Fig. 1.6, and it consists of seven chapters:

Chapter 1 introduces corrosion problem of offshore structures, the current repair design practice, the state-of-the-art research activities, research needs and the objectives of this study.

Chapter 2 presents an experimental study on mechanical properties, geometrical features, hardness distributions, as well as microstrucutral compositions of underwater fillet welds considering weld orientations, base steels, and corrosion effects. The study highlights the unique properties of underwater wet welds used in the repair work through the comparison of results between wet welds and their counterpart in-air welds.

Chapter 3 proposes two finite element models to construct fillet welds in numerical analysis. One model is used to reproduce the experimental tests presented in Chapter 2 based on the estimation of material properties and a geometrical assumption of underwater fillet welds; and the other model, utilizing the generalized results from weld strength tests, is used to analyze fillet welded structures where the nonlinear behavior is of importance. Two models provide tools to study fillet welds and welded structures by finite element analysis.

Chapter 4 presents a numerically study on welding patch repaired pipe piles under compression using the weld model proposed in Chapter 3. The current design method is evaluated in terms of structural behavior of pipe piles with different welding patterns, the contribution of transverse fillet welds, and the load share ratio of patch plates. Corresponding equations and formulas are proposed to revise the calculations in the current design.

Chapter 5 studies the repaired performance of pipe piles repaired by patch welding under compression with emphasis on the effect of the existing loads applied to pipe piles. By integrating the findings obtained from Chapter 4 and Chapter 5, the design method and the corresponding flow chart for welding patch repair are proposed.

Chapter 6 presents an experimental study on an innovative method to repair offshore steel structures using CFRP strand sheet and underwater epoxy. The curing effect of epoxy and the repaired performance of steel plates are discussed, and the necessity of considering the curing effect and conditions of epoxy in the repair design is emphasized.

Chapter 7 serves as a summary of conclusions of this study as well as suggestions for future research in this area.

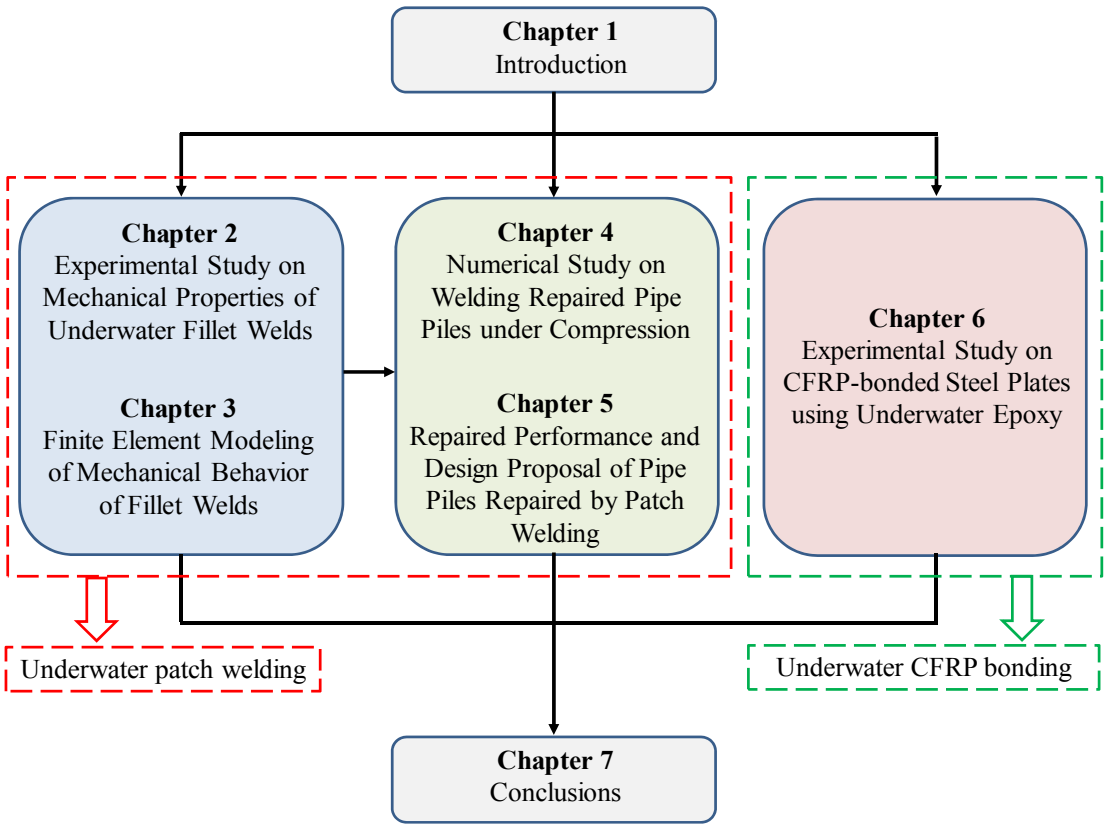

Fig. 1.6 Structural organization of the thesis

REFERENCES

1.1) The website of The Statistics Bureau and the Director-General for Policy Planning of Japan, "9.2 Survey on Port and Harbour (Designated Statistical Survey)", *http://www.stat.go.jp/English/index/official/209.htm#2*, [Retrieved 20 May 2011].

1.2) The website of The National Bureau of Statistics of China, "16-30 Volume of Freight Handled in Coastal Ports above Designated Size", *http://www.stats.gov.cn/tjsj/ndsj/2010/html/P1630e.htm*, [Retrieved 20 May 2011].

1.3) The Eurostat website, "File:Gross weight of seaborne goods handled in all ports (in million tonnes), 1997-2009 (table).PNG", *http://epp.eurostat.ec.europa.eu/statistics_explained/index.php? title=File:Gross_weight_of_seaborne_goods_handled_in_all_ports_(im_million_tonnes),_1997-2009_(table).PNG&filetimestamp=20110209143810*, [Retrieved 20 May 2011].

1.4) Research and Innovative Technology Administration, *Freight Transportation: Global Highlights, 2010*, Bureau of Transportation Statistics, U.S. Department of Transportation, US, 2010.

1.5) Coastal Development Institute of Technology, *Port Steel Structure Corrosion-Prevention and Repair Manual (version 2009)*, Coastal Development Institute of Technology, Japan, 2009 (in Japanese).

1.6) Zen, K. Corrosion and life cycle management of port structures, *Corrosion Science*, 47, pp. 2353-2360, 2005.

1.7) Task Committee on Evaluation of Corrosion Protection and Durability for Steel and Composite Structures under Offshore Environment, *Guidelines for Evaluation of Durability and Load-Carrying Capacity for Steel Structures under Marine Environment*. Committee of Structural Engineering, JSCE, Japan, 2009.

1.8) Department of Transportation, China, *JTS 153-3-2007*: *Technical Specification for Corrosion Protection of Steel Structures for Sea Port Constructions*, *Chinese Industry Standard*, Department of Transportation, China, 2007.

1.9) Yamasawa, T., Nogami, K., Itoh, Y., Watanabe, E., Sugiura, K., Fujii, K., and Nagata, K., Corrosion shapes of steel angle member under oceanic exposure during 19.5 years, *Doboku Gakkai Ronbunshuu A*, JSCE, 64(1), pp. 27-37, 2008 (in Japanese).

1.10) Public Works Research Institute, *Research report on technologies for durability improvement of marine structures: Results of twenty years' exposure test*, Public Works Research Institute, Japan,

2006 (in Japanese).

1.11) PIANC PTC-II WG31, *Life cycle management of port structures-general principles*, *Supplement to Bulletin no. 99*, International Navigation Association, 1998.

1.12) Perez-Guerrero, F., and Liu, S., Maintenance and repair welding in the open sea, *Welding Journal*, 84(11), pp. 54-59, 2005.

1.13) Coastal Development Institute of Technology, *Port Steel Structure Corrosion-Prevention and Repair Manual (version 1997)*, Coastal Development Institute of Technology, Japan, 1997 (in Japanese).

1.14) Wernicke, R., and Pohl, R., Underwater wet repair welding and strength testing on pipe-patch joint, *Journal of Offshore Mechanics and Arctic Engineering*, ASME, 120(11), pp. 237-242, 1998.

1.15) Wernicke, R. and Billingham, J., Underwater wet repair welding and strength testing on pipe-patch joints, *Journal of Offshore Mechanics and Arctic Engineering*, ASME, 120(4), pp. 237-242, 1998.

1.16) Kinugawa, J., and Fukushima, S., Influence of equivalent carbon contents of steels on proportions of martensite, hardness and susceptibility to cold cracking at coarse-grained regions in underwater wet welding, *Welding Society Journal*, 51(3), pp. 45-51, 1982 (in Japanese).

1.17) Ibarra, S., Grubbs, C. E. and Olson, D. L., Metallurgical aspects of underwater welding, *Journal of Metals*, 40(12), pp. 8-10, 1988.

1.18) Pope, A., Teixeira, J., Dos Santos, V., Paes, M., and Liu, S., The effect of nickel on the mechanical properties of high-oxygen underwater wet welds, *Journal of Offshore Mechanics and Arctic Engineering*, ASME, 118(2), pp. 165-168, 1996.

1.19) West, T. C., Mitchell, G., and Lindberg, E., Wet welding electrode evaluation for ship repair, *Welding Journal*, 69(8), pp. 46-56, 1990.

1.20) Rowe, M. D., Liu, S., and Reynolds, T. J., The effect of ferro-alloy additions and depth on the quality of underwater wet welds, *Welding Journal*, 81(8), pp. 156S-166S, 2002.

1.21) Akselsen, O. M., Fostervoll, H., Harsvaer, A., and Aune, R., Weld metal mechanical properties in hyperbaric GTAW of X70 pipeline, *International Journal of Offshore and Polar Engineering*, 16(3), pp. 233-240, 2006.

1.22) Zhang, X. D., Chen, W. Z., Ashida, E., and Matsuda, F., Metallurgical and mechanical properties of underwater laser welds of stainless steel, *Journal of Material Science & Technology*, 19(5), pp. 479-483, 2003.

1.23) AWS Technical Activity Committee, *ANSI/AWS D3.6M: Underwater welding code*, American

Welding Society (AWS), United States, 2010.

1.24) Japanese Industry Standards Committee, *JIS Z 3111: Methods of tension and impact tests for deposited metal*, Japanese Industry Standards Committee, Japan, 2005 (in Japanese).

1.25) Kitane, Y., Itoh, Y., Watanabe, N., and Matsuoka, K., Compressive and flexural tests of thickness-reduced steel pipes repaired with patch plates using underwater wet welding, *Journal of Structural Engineering*, JSCE, 55A, pp. 889-902, 2009 (in Japanese).

1.26) Khedmati, M. R., Rastani, M., and Ghavami, K., Numerical study on the permissible gap of intermittent fillet welds of longitudinally stiffened plates under in plane axial compression, *Journal of Constructional Steel Research*, 63, pp. 1415-1428, 2007.

1.27) Bakis, C. E., Bank, L. C., Brown, V. L., Cosenza, E., Dayalos, J. F., Lesko, J. J., Machisa, A., Rizkalla, S. H., and Triantafillou, T. C., Fiber-reinforced polymer composites for construction-state-of-the-art review. *Journal of Composites for Construction*, ASCE, 6(2), pp. 73-87, 2002.

1.28) Zhao, X. L., and Zhang, L., State-of the art review on FRP strengthened steel structures. *Engineering Structures*, 29, pp. 1808-1823, 2007.

1.29) Chaallal, O., Shahawy, M., and Hassan, M., CFRP Repair and strengthening of structurally deficient piles: design issues and field application, *Journal of Composites for Construction*, ASCE, 2(1), pp. 26-34, 2006.

1.30) Walker, R., A., and Karbhari, V. M., Durability based design of FRP jackets for seismic retrofit, *Composite Structures*, 80, pp. 553-568, 2007.

1.31) Luccioni, B., and Rougier, V. C., In-plane retrofitting of masonry panels with fibre reinforced composite materials, *Construction and Building Materials*, 25, pp. 1772-1788, 2011.

1.32) Abanilla, M. A., Karbhari, V. M., and Li, Y., Interlaminar and intralaminar durability characterization of wet layup carbon/epoxy used in external strengthening. *Composites, Part B: Engineering*, 37, pp. 650-661, 2006.

1.33) Abanilla, M. A., Li, Y., and Karbhari, V. M., Durability characterization of wet lay-up carbon/epoxy composites used in external strengthening. *Composites, Part B: Engineering*, 37, pp. 200-212, 2006.

1.34) Frigione, M., Aiello, M. A., and Naddeo, C., Water effects on the bond strength of concrete/concrete adhesive joints. *Construction and Building Materials*, 20, pp. 957-970, 2006.

1.35) Frigione, M., Lettieri, M., and Mecchi, A. M., Environmental effects on epoxy adhesives employed for restoration of historical buildings. *Journal of Materials in Civil Engineering*, 18, pp. 715-722, 2006.

1.36) Sen, R, Advances in the application of FRP for repairing corrosion damage, *Progress in Structural Engineering and Materials*, 5, pp. 99-113, 2003.

1.37) Sen, R., and Mullins, G., Application of FRP composites for underwater piles repair, *Composites, Part B: Engineering*, 38, pp. 751-758, 2007.

1.38) Yi, N. H., Nam, J. W., Kim, S. B., Kim, I. S., and Kim, J. H. J., Evaluation of material and structural performances of developed aqua-advanced-FRP for retrofitting of underwater concrete structural members. *Construction and Building Materials*, 24, pp. 566-576, 2010.

1.39) Seica, M.V., and Packer, J. A., FRP materials for the rehabilitation of tubular steel structures for underwater applications, *Composite Structures*, 80, pp. 440-450, 2007.

CHAPTER 2
EXPERIMENTAL STUDY ON MECHANICAL PROPERTIES OF UNDERWATER FILLET WELDS

2.1 INTRODUCTION

Underwater wet welding has long been recognized as one of the most common techniques to build, and particularly to repair offshore steel structures, such as oil platforms, pier piles, and pipelines. Due to its high efficiency in time and relatively low cost, underwater wet welding is gaining more popularity for recent energy explorations into the sea[2.1), 2.2)]. Not surprisingly, over the past decades, a number of studies have been done on underwater wet welds on their metallurgical features[2.3), 2.4)], influence of quenching[2.5)], development of electrodes suitable for underwater wet welding[2.6)], etc. Although some studies have examined mechanical properties of underwater welds, they mainly focused on properties of weld materials[2.7) ~ 2.9)]. Few studies have been carried out stressing on the mechanical properties of underwater fillet welds as structural joints, which are crucial parts of the structures to be built or repaired. Fig. 2.1 shows a typical work to repair offshore steel pipe piles and steel sheet piles by welding patch steel plates over corrosion-damaged areas. The structural portions to be repaired are usually located at splash and tidal zones, where severe corrosion damages occur.

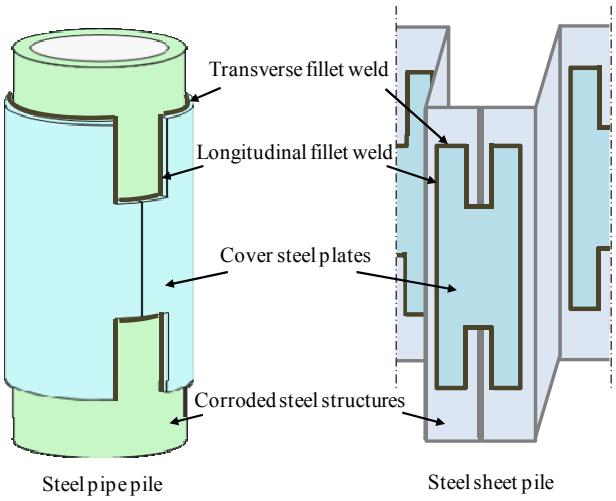

Fig. 2.1 Repaired offshore steel structures using underwater patch welding

The present *Port Steel Structure Corrosion-Prevention and Repair Manual* in Japan[2.10], based on tests on forty-six fillet welded specimens conducted in 1985, discounts strength of fillet welds made in underwater wet environment by specifying as 80% of that of in-air welds when designing weld joints to repair corrosion damaged offshore structures for any base steels. Hence, the allowable stress of underwater welds ranges from 62 MPa for SS400, SM400, and SMA400 base steels to 94 MPa for SM490Y, SM520, and SMA490 base steels. In addition, in *U.S. Navy Underwater Cutting & Welding Manual*[2.11], the strength of underwater welds, which ranges from 34 MPa for mild base steels to 62 MPa for high strength base steels, is defined as the electrode strength divided by a safety factor of 6.

There are many offshore steel structures constructed more than 40 years ago in Japan, many of which may require repair work in the near future. To achieve an efficient and effective repair design for welding patch plates in underwater wet environment over corrosion-damaged areas, the performance of the repaired structures has to be accurately evaluated in the design process. One of goals of this research is to identify mechanical behavior of underwater fillet welds to be considered in the repair design and to propose design recommendations for efficient repair work. As the first step towards the goal, this chapter presents an experimental study on the strength and ductility of underwater fillet weld joints, and differences in mechanical properties between underwater welds and their counterpart in-air welds are investigated qualitatively as well as quantitatively. Vickers hardness tests and microstructure examinations are also performed on the welds to examine their material features, which enable comprehensive understanding of mechanical properties of underwater wet welds.

2.2 EXPERIMENTAL PROGRAM

Table 2.1 presents the test matrix indicating different weld assemblies with their designations and parameters. In total, fourteen types of different fillet weld assemblies are tested with respect to two welding environments of in-air and underwater, two weld orientations of transverse and longitudinal fillet welds, and four base steels of SY295, SYW295, and corroded SY295 for steel sheet piles, and STK400 for steel pipes. SY295, SYW295, and STK400 are specified to have minimum yield stresses of 295 MPa, 295 MPa, and 235 MPa in JIS A5528, A5523, and G3444, respectively. Test results for STK400, presented in Ref. 2.12), are listed here for comparison.

In this study, the number following the weld designation is a specimen's number, and the number following the mark "#" is a weld bead number in the specimen. For example, LYA1#2 means No. 2 weld bead on the first specimen of LYA assembly type.

Table 2.1 Test matrix

Specimen designation	No. of specimen	Structural type	Welding environment	Weld orientation	Base steel	Base plate thickness (mm)	Weld length (mm)	Cover plate
TYA	3	Sheet pile	In-air	Transverse	SY295	13 mm	40 mm	SM490A (t=9mm)
TWA	3				SYW295			
LYA	3			Longitudinal	SY295			
LWA	3				SYW295			
LCA	3				CSY295	6-8 mm	20 mm	
TYW	3		Underwater	Transverse	SY295	13 mm	40 mm	
TWW	3				SYW294			
LYW	3			Longitudinal	SY295			
LWW	3				SYW295			
LCW	2				CSY295	6-8 mm	20 mm	
TKA	4	Pipe (Φ216.3mm)	In-air	Transverse	STK400	12.7 mm	40 mm	SM400B (t=9mm)
LKA	4			Longitudinal				
TKW	4		Underwater	Transverse				
LKW	4			Longitudinal				

2.2.1 Test Specimens and Material Properties

Two configurations of specimens with different weld orientations according to JIS Z3131 and JIS Z3132 are used for sheet pile specimens as well as pipe specimens as illustrated in Fig. 2.2. The weld leg length is specified as 6 mm. Two welders, with working experience of 24 years and 27 years, are assigned to in-air and underwater welding work, respectively. Fig. 2.3 shows two welders assigned to conduct the welding work in this study.

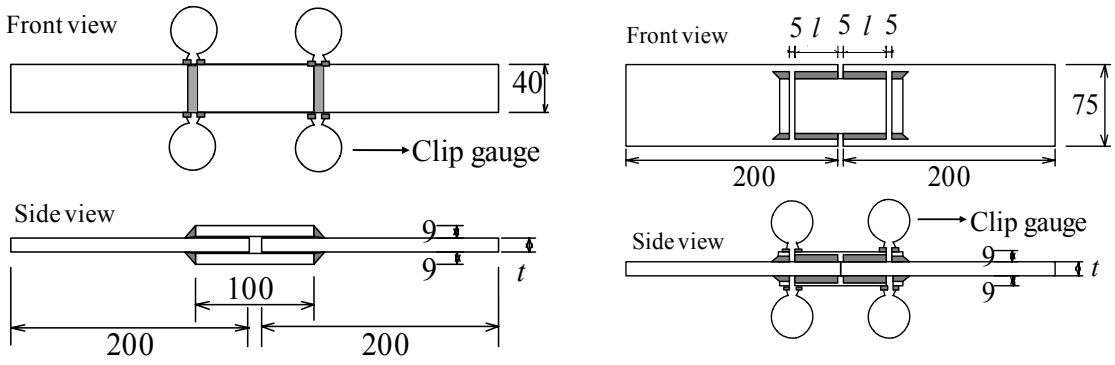

(a) Transverse specimen (b) Longitudinal specimen

Fig. 2.2 Specimen configuration (unit in mm)*

*Curvature of the pipe base is not depicted. t = 13 or 6-8 for sheet base plates, t = 12.7 for pipe base plates; and l = 40 for pristine base plates, l = 20 for corroded base plates.

(a) In-air welder (b) Underwater welder

Fig. 2.3 Welders assigned to conduct welding work in this study

One weld pass is used in welding process as used in the real repair work, and the welding direction is specified in the same way for both underwater welds and in-air welds, that is from lower to upper for longitudinal welds and from left to right for transverse welds. Longitudinal welding is performed in the vertical position, while transverse welding is performed basically in the horizontal position which is close to the flat position for upper sides of transverse welds and the overhead position for lower sides of transverse welds. Welding of underwater specimens is performed in a 3-m deep seawater pool to simulate underwater welding performed on structural portions at the tidal zone. Fig. 2.4 shows the seawater pool used for underwater welding in this

study. Welding conditions used in the study are specified to simulate those in the real repair welding, and they are shown in Table 2.2.

Fig. 2.4 Seawater pool used for underwater welding

Table 2.2 Welding details

Case	Welding environment	Orientation	Current(A)	Voltage(V)	Welding velocity(mm/min)	Temperature (℃)	pH	Salinity (wt-%)
Sheet pile	In-air	Longitudinal	70-80	12-16	65-85	17	-	-
		Transverse	55-70	10-20	145-200			
	Underwater	Longitudinal	80-95	19-23	60-70	14	7.9	2.6
		Transverse	75-95	16-23	120-160			
Pipe pile*	In-air	Longitudinal	100-110	20-30	79	*Not measured*	-	-
		Transverse	90-100	20-40	88			
	Underwater	Longitudinal	120-140	20-40	79	25.6	8.2	2.1
		Transverse	120-140	20-40	88			

*Data for pipe pile are from Watanabe et al.[2.12)]

Table 2.3 Material properties of steels

Material	Mechanical properties					Chemical compositions (wt-%)					
	Young's modulus, E(GPa)	Poisson's ratio, ν	Yield stress, σ_y (MPa)	Ultimate strength, σ_u (MPa)	Elongation, Δl (%)	C	Si	Mn	P	S	CE_{IIW}*
SY295	213	0.29	273**	497	41	0.30	0.06	0.72	0.016	0.020	0.430
CSY295	212	0.29	349	531	34	0.27	0.02	0.96	0.013	0.019	0.433
SYW295	213	0.28	392	513	42	0.10	0.23	1.41	0.020	0.005	0.379
STK400	203	0.28	362	394	41	0.12	0.10	0.56	0.013	0.006	0.230
SM490A	209	0.28	361	532	39	0.16	0.34	1.44	0.015	0.007	0.457
SM400B	213	0.28	290	416	46	0.12	0.23	1.02	0.013	0.003	0.328
Electrode***	-	-	410	460	30	0.10	0.10	0.43	0.015	0.007	0.188

*CE_{IIW} = C+(Si+Mn)/6+(Cr+Mo+V)/5+(Ni+Cu)/15, only first two terms are used except SYW295. **Tested 273 MPa is smaller than specified 295 MPa. Verifications with steel manufacturer suggest that this is caused by variations in sampling regions on sheets coupled with differences between loading rates in coupon tests. ***Catalogue values provided by the manufacturer.

Mechanical properties of steels, listed together with chemical compositions in Table 2.3, are obtained from static tensile coupon tests using a 500 kN MTS material testing machine. Fig. 2.5 shows the tensile test curves of steels. It is noted that the test curves shown in the figure are not completely recorded due to the failure of strain gauges at the middle span of the test coupons before the fracture of steels. The ultimate strength of steels is accurately captured by MTS machine although it is not necessarily indicated in the curves.

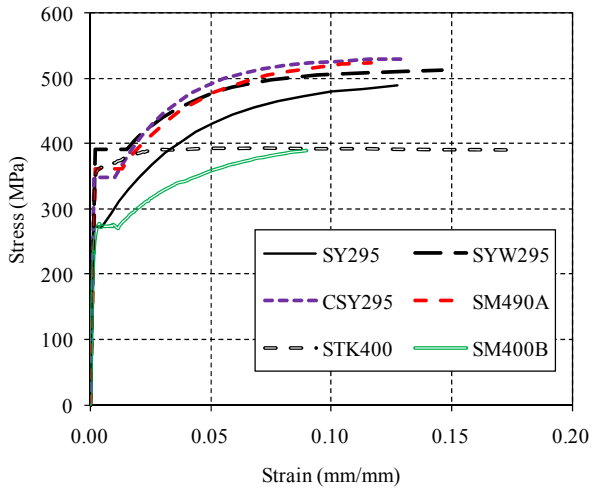

Fig. 2.5 Representative results from steel tensile coupon tests

To distinguish corroded and uncorroded SY295 base plates, the corroded SY295 base plate is referred to as CSY295 in this study. It should be noted that CSY295 base plates with thickness varying from 6 to 8 mm are cut from in-situ steel sheet piles, which has been exposed to marine environment for about 35 years at Kimitsu Works, Nippon Steel Corporation, Japan. The corroded sheet piles are shown in Fig. 2.6. CSY295 base plates are prepared to study corrosion effects, which are thickness reduction and surface roughness in this study, on weld properties. Corrosion products on the base plates are removed completely by sand blasting.

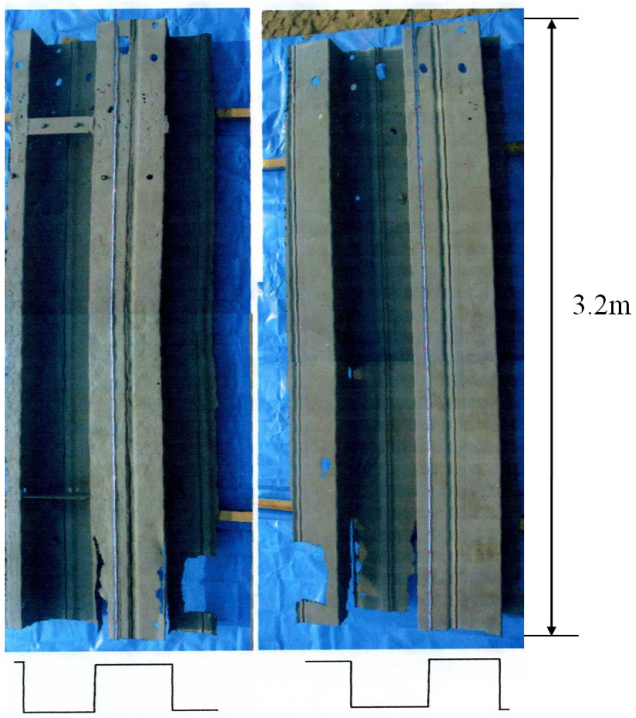

Fig. 2.6 Steel sheet piles SY295 corroded for 35 years

Table 2.4 lists thickness and surface roughness parameters of corroded SY295 steels. Only the parameters of base steels with patch plates are shown in the table, because the thickness and roughness of steel beyond welding patched areas are regarded to have no influence to mechanical properties of fillet welds. Surface roughness parameters are calculated based on surface profile data measured at Hiroshima University. Prior to the weld strength tests, weld profiles are measured by a laser displacement sensor. Five equidistant cross sections along each weld bead are measured, and the weld leg length, the size of throat, and weld size of each bead are calculated by averaging the five sections.

Table 2.4 Thickness and roughness of patched area on corroded bases (unit in mm)

Patched area of specimen	Thickness parameter		Roughness parameter*					
	Average thickness	Standard deviation	Sea side			Soil side		
			Ra	*Rz*	*Rq*	*Ra*	*Rz*	*Rq*
LCA1	5.37	0.66	0.23	1.98	0.29	0.11	0.69	0.13
LCA2	6.69	0.69	0.23	1.85	0.30	0.19	1.11	0.22
LCA3	7.22	0.51	0.19	1.43	0.24	0.14	0.87	0.16
LCW1**	6.28	0.66	0.14	1.04	0.17	0.08	0.52	0.09
LCW2	6.51	0.57	0.19	1.41	0.23	0.06	0.50	0.07
LCW3	7.51	0.82	0.33	2.01	0.40	0.07	0.64	0.09

*Notation for roughness parameters is specified in JIS B 0601: 2001. *Ra*: Arithmetic mean height of the rough surface, *Rz*: Maximum height of the rough surface, *Rq*: Root mean square height of the rough surface. **LCW1 specimen is not used in the test due to misproduction.

2.2.2 Test Setup

The specimens are tested under a quasi-static tensile loading. Since there are two weld orientations, longitudinal welds are tested in shear while transverse welds are in tension. Deformation of individual weld is measured by clip gauges placed at the ends of each weld bead shown in Fig. 2.2. Fig. 2.7 illustrates the test setup. In this study, weld strength is defined as Eq. (2.1) according to JIS Z3131 and Z3132:

$$\sigma_w = \frac{P_{\max}}{n\bar{a}l} \tag{2.1}$$

where, σ_w is the average strength of fillet weld despite of nonuniform distribution of shear stress in longitudinal welds, P_{max} is the maximum load, $\bar{a}$ is the average throat size of all welds in each specimen, l is the average weld length, and n is the number of welds in one cross section of the specimen, which is 2 for transverse weld specimens and 4 for longitudinal weld specimens. By adopting n, the formula implicitly assumes that the total load is shared equally by welds in the same cross section of specimen in spite of slight asymmetry in the weld shape.

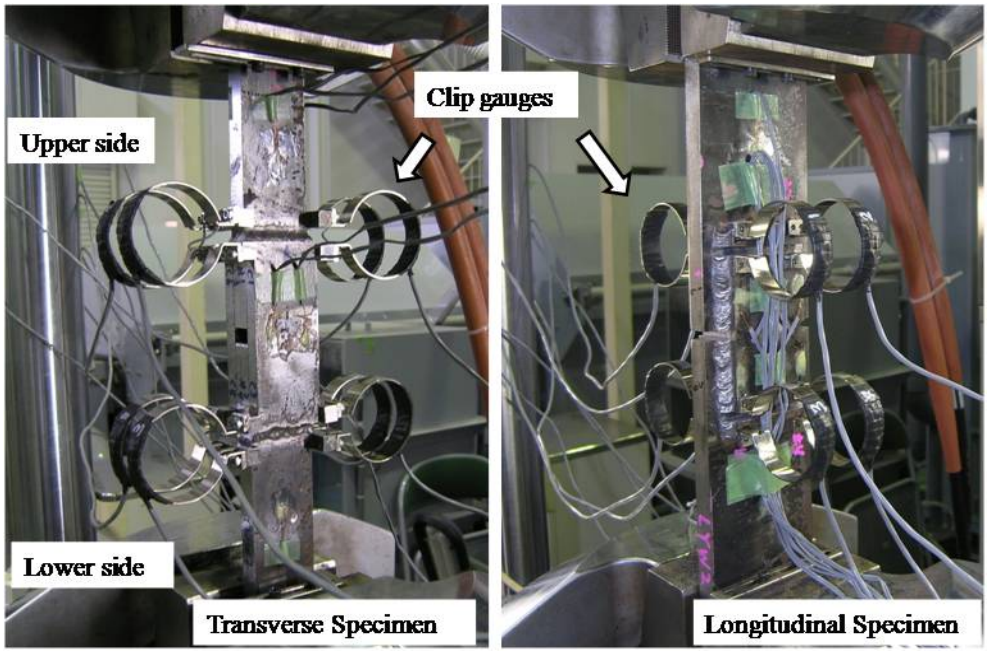

Fig. 2.7 Test setup

Weld ductility, a normalized deformation factor, is defined as:

$$\gamma = \frac{\Delta_{\max}}{s} \tag{2.2}$$

where, γ is the ductility factor, Δ_{max} is the measured weld deformation of the first fractured weld at its maximum applied load, and s is the weld size of the first fractured weld. The definition of the weld size (JIS Z3001) is illustrated in Fig. 2.8.

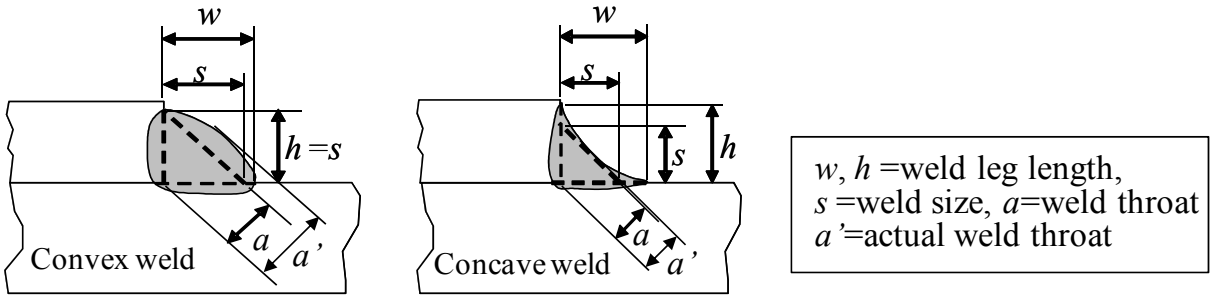

(a) Convex weld (b) Concave weld (c) Notation of weld size

Fig. 2.8 Definition of weld size

2.3 INSPECTION ON FILLET WELDS

Profile features of fillet welds are examined through three-dimensional surface profile data measured by laser displacement sensor. Weld defects, such as pits and blow holes are inspected through the dye penetration test (JIS Z2343) and the radiographic examination (JIS Z3104). The radiographic examination is only performed on STK400 specimens. After weld strength tests, visual inspection is also conducted to examine weld undercut and weld penetration at weld roots.

2.3.1 Weld Profile Features

One obvious finding is that profiles of underwater welds are more irregular and deviated from the idealized shape of an isosceles triangle when compared with those of in-air welds as shown in Fig. 2.9. Moreover, although the weld leg length is specified as 6 mm for both leg lengths h and w, weld profiles exhibit distinct trends related to welding environments and welding positions. Fig. 2.10 shows h and w of all the weld beads, Table 2.5 summarizes an average h/w value of each weld assembly type.

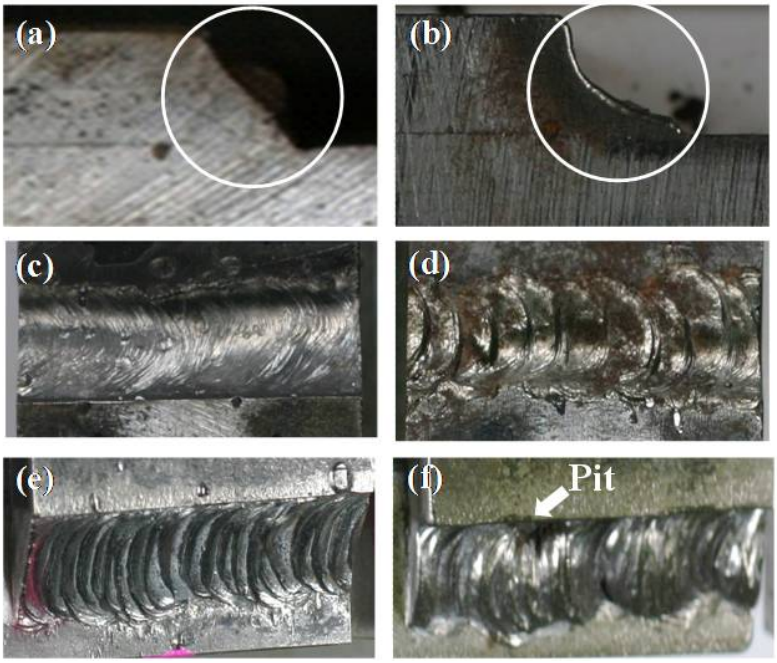

(a) TKA (b) TKW (c) TYA (d) TYW (e) LYA (f) LYW

Fig. 2.9 Weld profiles

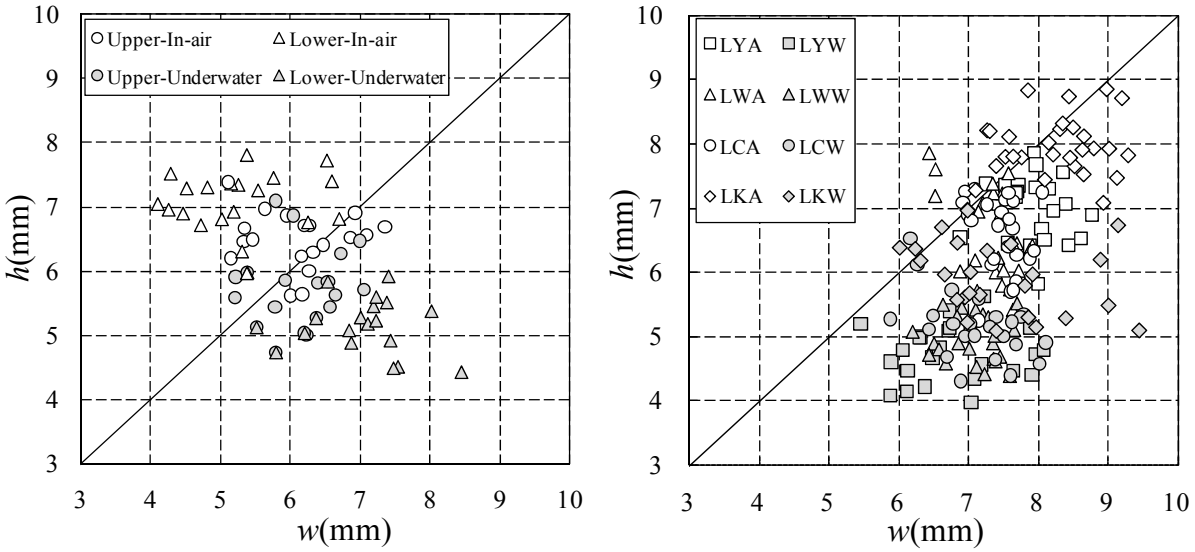

(a) Transverse weld (b) Longitudinal weld

Fig. 2.10 Measurement data of weld leg length

Table 2.5 *h*/*w* values of welds

Welding environment	Structural type	Transverse		Longitudinal
		Upper	Lower	
In-air	Sheet pile	1.10	1.36	0.89
	Pipe pile	1.43	1.03	0.97
Underwater	Sheet pile	0.94	0.78	0.71
	Pipe pile	0.96	0.72	0.81

Generally, underwater welds show *h* smaller than *w* in both weld orientations, with all *h*/*w* values being smaller than 1. Note that there are an upper side and a lower side of the cover plate in a transverse weld specimen, as previously indicated in Fig. 2.7. In underwater cases, transverse welds on the upper side exhibit *h*/*w* values close to 1, with 0.94 for the sheet pile case and 0.96 for the pipe case, while transverse welds on the lower side and longitudinal welds exhibit *h*/*w* values ranging from 0.72 to 0.81. This can be explained by welding positions and electrode angles in welding process, the better welding visibility and workability in the upper sides of transverse welds would favor welders to produce welds closer to what is specified.

The weld number system and notations, which will be used the size measurement, are demonstrated in Fig. 2.11.Weld dimensions of the sheet pile specimens are shown in Fig. 2.12

along with the first fractured weld and maximum load obtained in the weld strength tests. In sheet pile specimens, in-air transverse welds on the upper side with bead numbers #1 and #3 exhibit concave profiles comparing with the ones on the lower side with bead numbers #2 and #4 which exhibit convex profiles. It is observed that although not always failing at the smallest weld, transverse welds made in air are found to be unlikely to fail on the lower side, where actual weld throat *a*' as defined in Fig. 2.8 is considerably larger than weld throat *a* defined in JIS Z3001 as shown in Figs. 2.12(a) and (b). However, no similar observation is found in underwater transverse welds which do not show a typical failure mode at weld deposit (DEPO) in the strength tests as will be discussed in Section 2.4.3.

As for different base steel materials and structural types, there is no obvious correlation found either between weld profiles and base steels or between weld profiles and structural types. Curvature of the pipe (with an outer diameter of 216.3 mm) used in this study does not seem to affect weld profiles significantly.

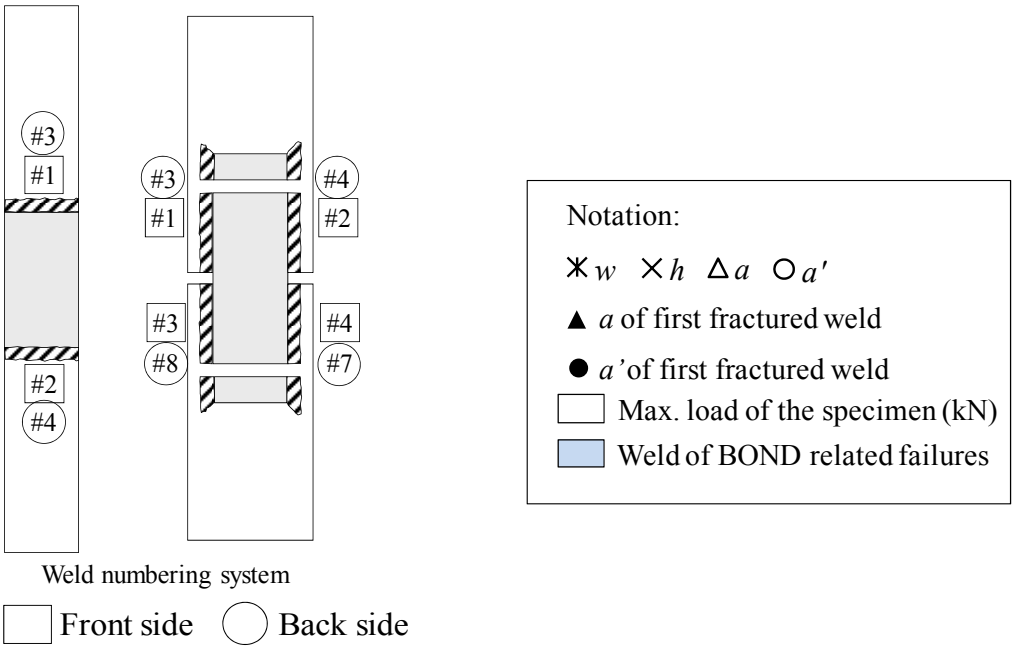

(a) Weld number system (b) Notation of markers and symbols

Fig. 2.11 Demonstration details of fillet welds

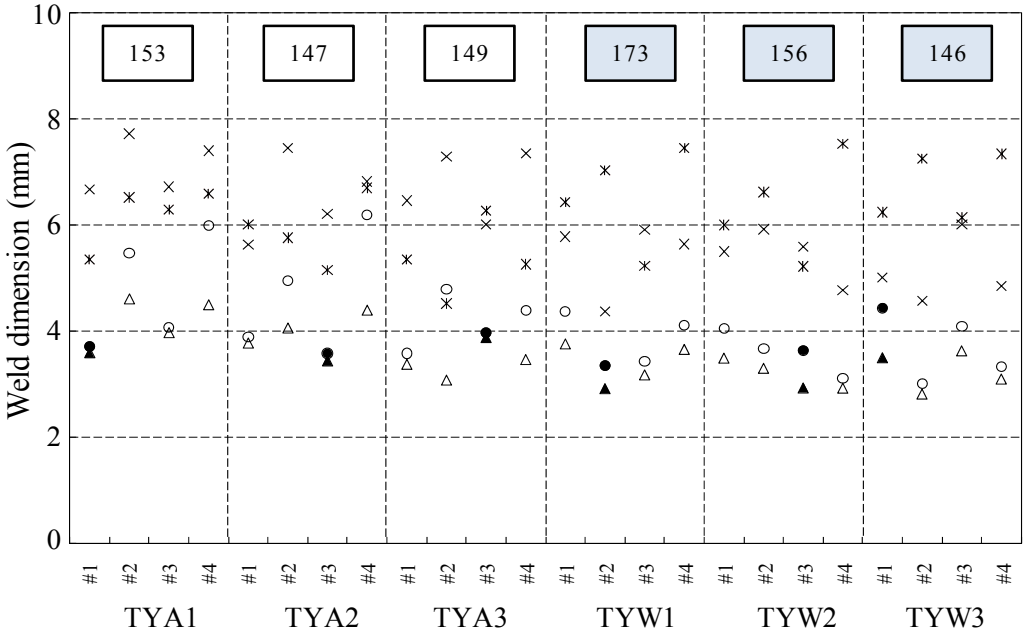

(a) Transverse welds on SY295 steel plate

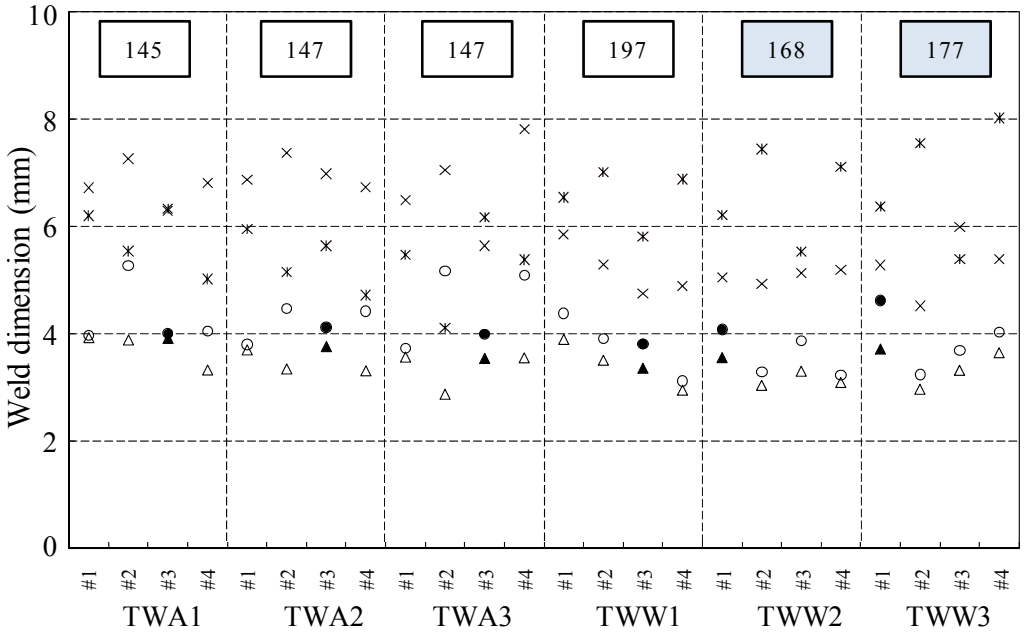

(b) Transverse welds on SYW295 steel plate

Fig. 2.12 Weld dimensions and first fractured welds for steel sheet pile specimens

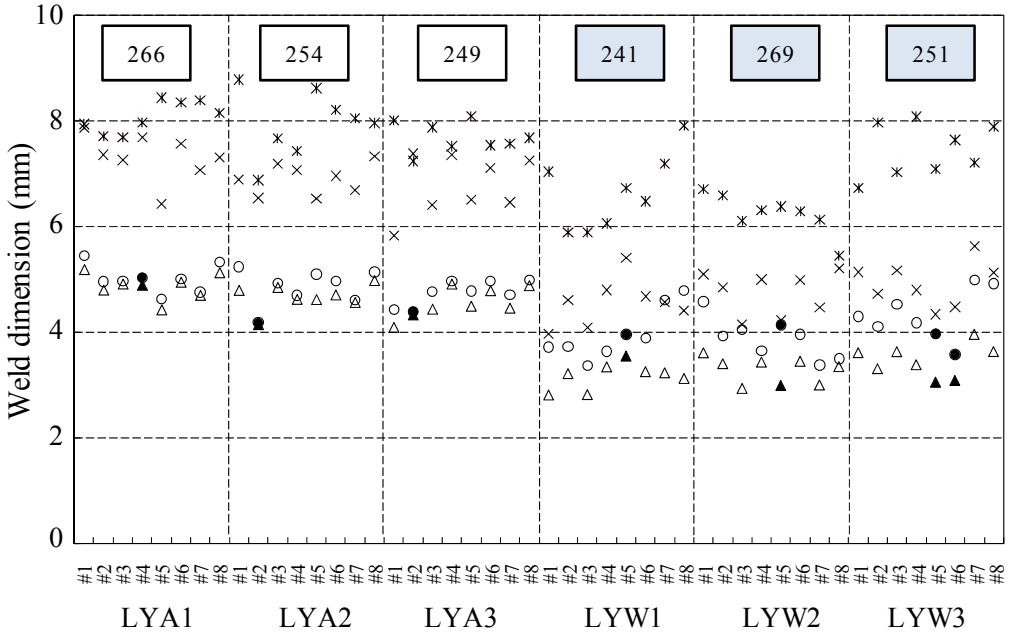

(c) Longitudinal welds on SY295 steel plate

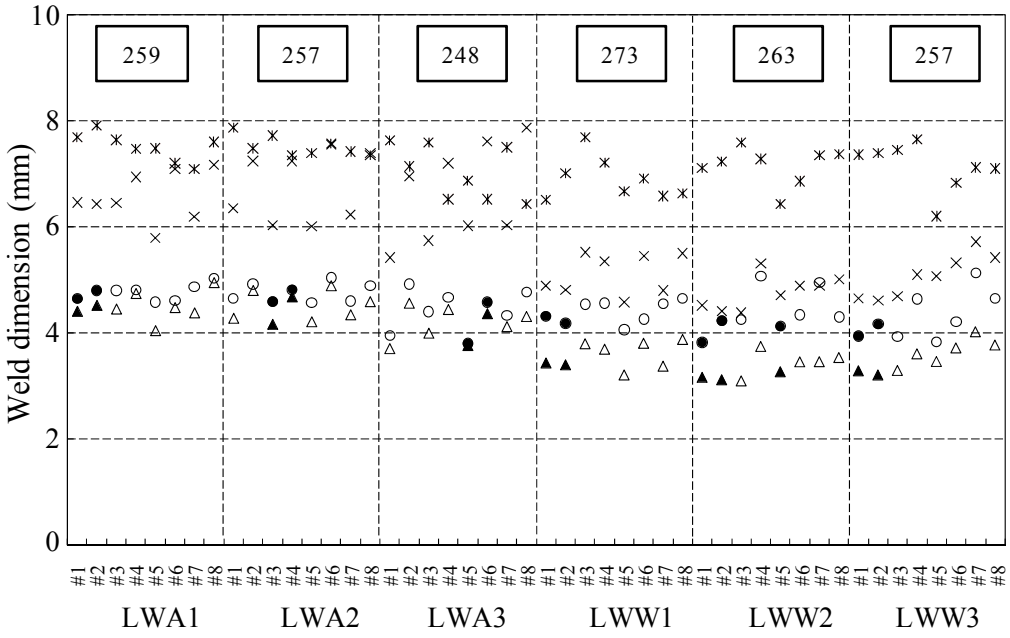

(d) Longitudinal welds on SYW295 steel plate

Fig. 2.12 Weld dimensions and first fractured welds for steel sheet pile specimens (continued)

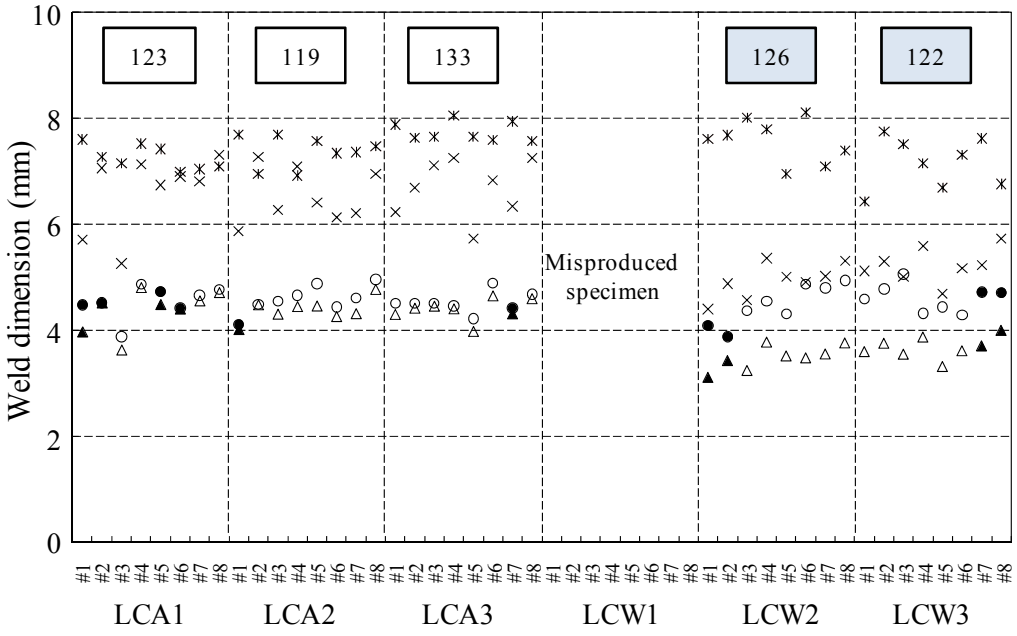

(e) Longitudinal welds on corroded SY295 steel plate

Fig. 2.12 Weld dimensions and first fractured welds for steel sheet pile specimens (continued)*

2.3.2 Weld Defects

Eleven surface-breaking defects, including circular ones with a diameter 1 to 3 mm and line-shaped ones with a length around 2 mm, are found in eight specimens out of twenty-two underwater weld specimens. There is no defect found in in-air welds. It is shown that more defects are found in longitudinal welds than transverse welds in this study. Two blow holes are found in LKW2#2 and TKW2#4 with diameters of 1.2 and 2.0 mm, respectively, by the radiographic examination.

Regardless of welding environments, slight weld undercut is found at base plates of transverse welds on the upper side and at cover plates of transverse welds on the lower side, while no noticeable weld undercut is found in longitudinal welds. After the strength tests, specimens are cut, and weld cross sections are inspected visually. It is observed that most underwater welds, regardless of weld orientations, bear incomplete weld penetration at roots to a slight extent.

Weld defects are expected to reduce weld strength. Some welds with defects fail in the strength tests, but others do not. In the similar manner, welds with defects do not show any

obvious correlations with weld failure mode, strength, or ductility factor in this study. Plausible causes may include that the weld defects are just too small and few to present significant effects.

2.4 EXPERIENTIAL RESULTS AND DISCUSSIONS

2.4.1 Load-Deformation Responses

Load-deformation curves of the first fractured weld in the weld assembly, one of each assembly type, are plotted in Fig. 2.13. Generally, welds in the same assembly exhibit similar load-deformation responses for most assembly types. The load in this figure is the total load in the specimen, and the deformation is the displacement measured at the end of the first fractured weld by clip gauges.

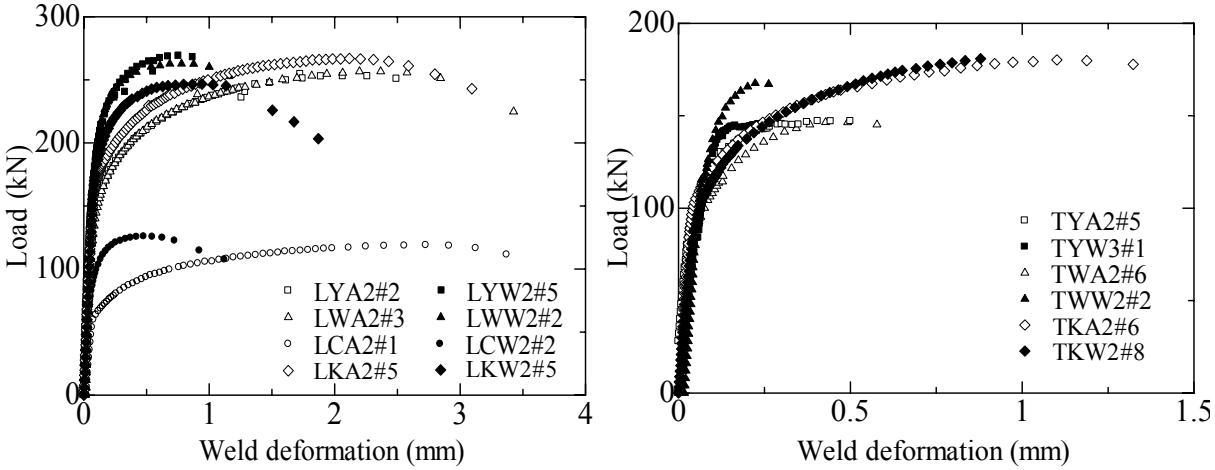

(a) Longitudinal weld (b) Transverse weld

Fig. 2.13 Load-deformation curves

Most of underwater welds show a larger ultimate load than that of their counterpart in-air welds. However, due to the significantly smaller weld throat, LKW with an average weld throat of 3.7 mm has a smaller ultimate load than LKA with an average weld throat of 5.0 mm.

It is also observed that all underwater weld specimens show significantly smaller fracture deformation than their counterpart in-air welds. In the load-deformation curves, there is always a

large plastic deformation before in-air welds fail, while for underwater welds, fracture comes soon after their maximum loads.

2.4.2 Weld Strength and Ductility

Weld strengths and ductility factors previously defined are plotted for all specimens in Fig. 2.14. For the sake of comparison between in-air and underwater welds, strength increase and ductility decrease of underwater welds are calculated in percent when compared with their counterpart in-air welds as shown in Fig. 2.15. Underwater welds show a strength increase ranging from 6.9% to 41%, while ductility decrease is about 50% for most weld assemblies. The weld strength and ductility are examined in terms of base steel materials, weld orientations, and corrosion of base steel in the following.

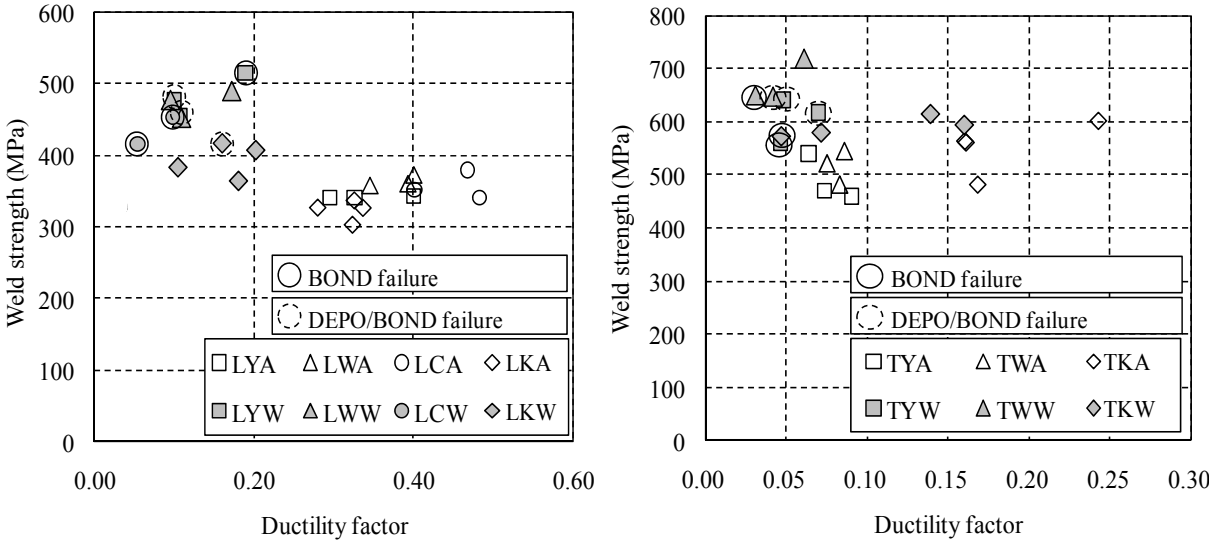

(a) Longitudinal weld (b) Transverse weld

Fig. 2.14 Weld strength versus ductility factor

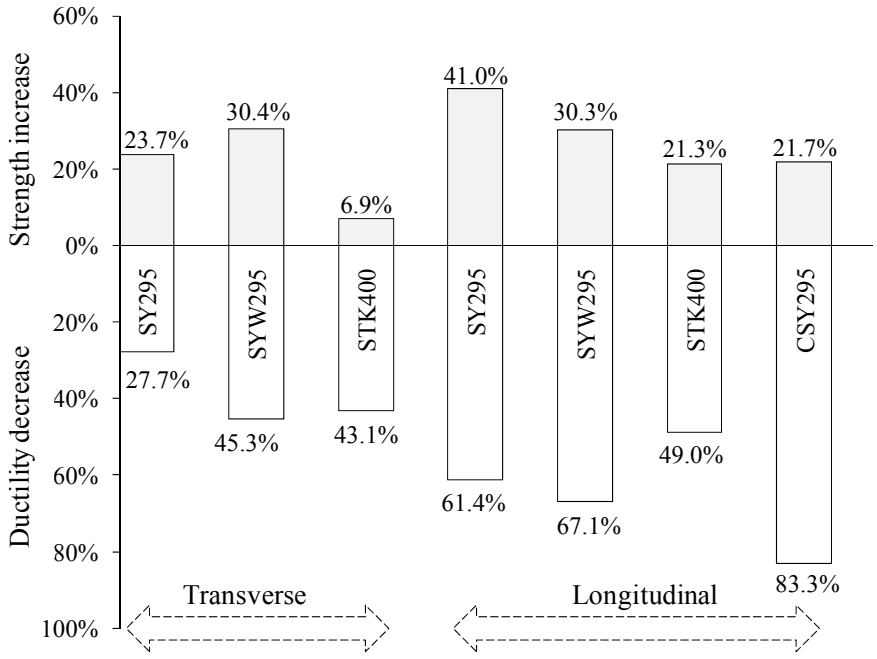

Fig. 2.15 Relative changes of strength and ductility from in-air welds to underwater welds

(1) Material types of base plates

Whether base plates are flat sheet pile or curved pipe, the shape difference of base plates is not found to be influential to either weld strength or ductility. On the other hand, differences in chemical compositions do affect strength and ductility significantly. As listed in Table 2.3, for sheet piles, SY295, SYW295, and CSY295, the carbon equivalent ranges from 0.379 to 0.433, which is much higher than 0.230 of the pipe material, STK400. Strength increase of underwater welds on sheet pile materials is 30% on the average, which is about twice as large as 14% of the pipe material, while ductility decreases for different materials are nearly the same at around 50% except transverse welds on SY295 and longitudinal welds on CSY295. The longitudinal welds on CSY295 exhibit a strength increase of 22% but a drastic ductility decrease of 83%, are not discussed here because they will be discussed in detail in the following section (3).

(2) Weld orientations

Mechanical properties of fillet welds are affected by weld orientations to a different degree as observed in Fig. 2.15. As for welds on SY295, when the weld orientation is changed from

transverse to longitudinal direction, strength increase and ductility decrease are nearly doubled from 24% to 41% and from 28% to 61%, respectively. Welds on STK400 show a greater change in strength but smaller in ductility, with strength increase tripled from 6.9% to 21% and ductility decrease remained at around 50%. However, welds on SYW295 are not affected by weld orientations and strength increase is about 30% for both directions.

Moreover, longitudinal fillet welds exhibit more sensitivity to wet welding environment, with a strength increase of 29% and a ductility decrease of 65% on average, than transverse fillet welds with a strength increase of 20% and a ductility decrease of 49%. It should be noted that the strength of welds produced in air, which fail at weld deposit (DEPO), tends to increase with ductility factor as shown in Figs. 2.14(a) and (b). This shows that weld strength is affected by how much weld beads can deform before they reach their maximum loads. For longitudinal welds, it is known that shear stress is non-uniform along the weld beads and the shear stress is larger at two ends and smallest at the center[2.13]. The small weld ductility will prevent additional load from being shared by weld in the central region because the two ends of the weld bead fracture soon after they yield. Consequently, the smaller the deformation capacity at weld ends in a longitudinal weld, the smaller weld strength will be. The same explanation is not applicable to the welds produced underwater because they do not show a typical DEPO failure as will be discussed later.

(3) Corrosion effects

It can be observed from Fig. 2.15 that underwater welds on corroded SY295 steel exhibit a strength increase of 22%, but a drastic ductility decrease of 83% when compared with their counterpart in-air welds. As indicated in Fig. 2.14(a), the LCA welds have the largest ductility factor with an average value of 0.45, but their counterpart LCW welds have the smallest ductility factor with an average value of 0.08 among all longitudinal welds.

To examine the corrosion effects on strength and ductility of fillet welds, CSY295 and SY295 are compared. Although the chemical compositions of CSY295 and SY295 are quite similar as shown in Table 2.3, LCW welds with an average strength of 435 MPa exhibit a smaller strength by 11% than LYW welds with an average strength of 482 MPa. However, for corresponding in-air welds, LCA welds have slightly larger strength with an average strength of 357 MPa than LYA

welds with an average strength of 342 MPa. This phenomenon can be explained by ductility of those welds. LCW welds show a ductility factor of 0.08, while LYW welds show 0.13, which is 1.6 times larger than LCW. As for LCA and LYA welds, the ductility factors are 0.45 and 0.34, respectively. The smaller ductility of LYA results in the smaller strength than LCA welds. The ductility factor of LCW is turned out to be the smallest among all longitudinal welds, which will be examined in the following sections of failure modes and hardness distribution.

One observation from the visual inspection after the strength tests is that LCW3#3 shows incomplete weld fusion due to corrosion pits in the base plate. Besides the incomplete fusion, there is no obvious correlation found between weld mechanical properties and specimen conditions, such as corrosion effects, thickness reduction and surface roughness of base plates. Considering only five specimens with corroded base plates are used in this study, more study may be needed to draw a further conclusion.

2.4.3 Failure Modes of Fillet Welds

In Fig. 2.14, failure modes are also indicated. It is observed that all in-air welds exhibit ductile fracture at DEPO, but underwater welds indicated with circles in Fig. 2.14 fail either at the boundary (BOND) between DEPO and base metal or with a combination of DEPO and BOND. Different failure modes of fillet weld joints are representatively shown in Fig. 2.16. All six underwater specimens with SY295 as the base steel, TYW and LYW, fail at BOND or DEPO/BOND regardless of the weld orientations. All two underwater specimens of CSY295, LCW, exhibit brittle fractures at BOND with little deformation observed in weld metals as shown in Fig. 2.16(c), resulting in low ductility of LCW welds.

With base steels of STK400 and SYW295, two out of eight specimens of TKW and LKW and two out of six specimens of TWW and LYW fail at BOND or DEPO/BOND. Considering the differences in carbon equivalent as shown in Table 2.3, the findings in failure modes suggest that “milder” steels STK400 and SYW295 with lower carbon equivalents of 0.230 and 0.379, respectively, have better weldability in underwater environments than SY295 and CSY295 steels with higher carbon equivalents of 0.430 and 0.433, respectively, although all the base steels do not show any problem in open air welding.




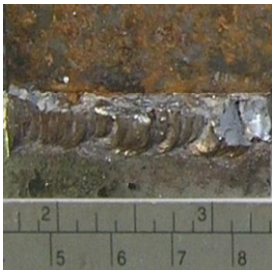

TYA1#1 LWA2#4 TWW2#1 LYW1#1

(a) DEPO failure (b) DEPO/BOND failure

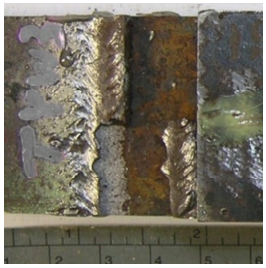
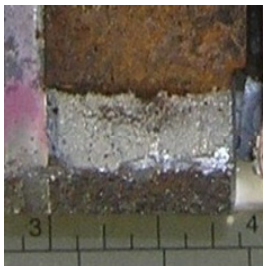

TYW3#1 LCW3#8

(c) BOND failure

Fig. 2.16 Comparison of failure modes

2.5 WELD HARDNESS AND MICROSTRUCTURES

Welding is a thermo-mechanical process, and weld properties are closely related to thermal conditions which affect weld microstructures and in turn mechanical properties. This section discusses results from Vickers hardness tests (JIS Z2244) and metallographic examinations of fillet welds. The specimens for hardness tests are produced simultaneously with specimens for the strength tests to ensure the same welding conditions.

2.5.1 Hardness Distribution

Fig. 2.17 shows the representative photos of polished and etched cross sections of LCA and LCW welds with Vickers hardness results superimposed. Points for data acquisition are located along the arrows in the figure. The hardness results on the side of base plate are summarized in Fig. 2.18. Three windows in each photo of Fig. 2.17 signify the areas where microstructure images, shown in Fig. 2.19, are taken.

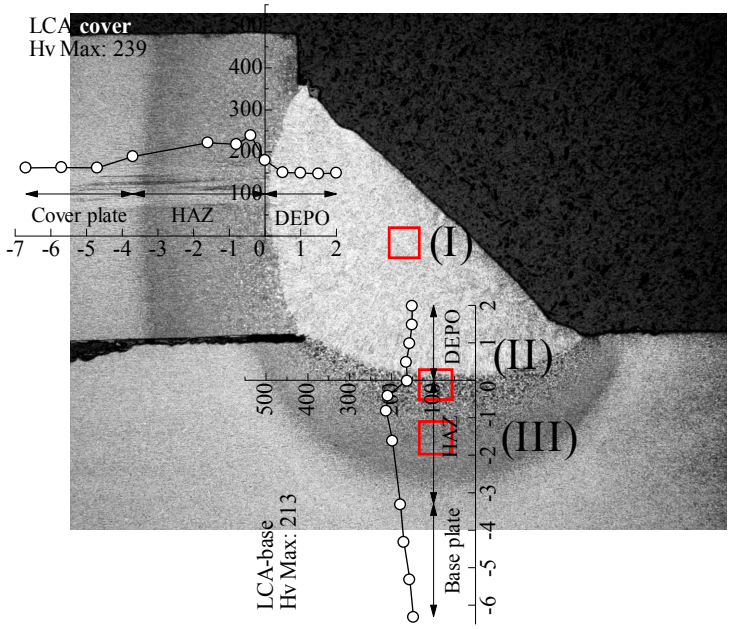

(a) LCA (in-air weld)

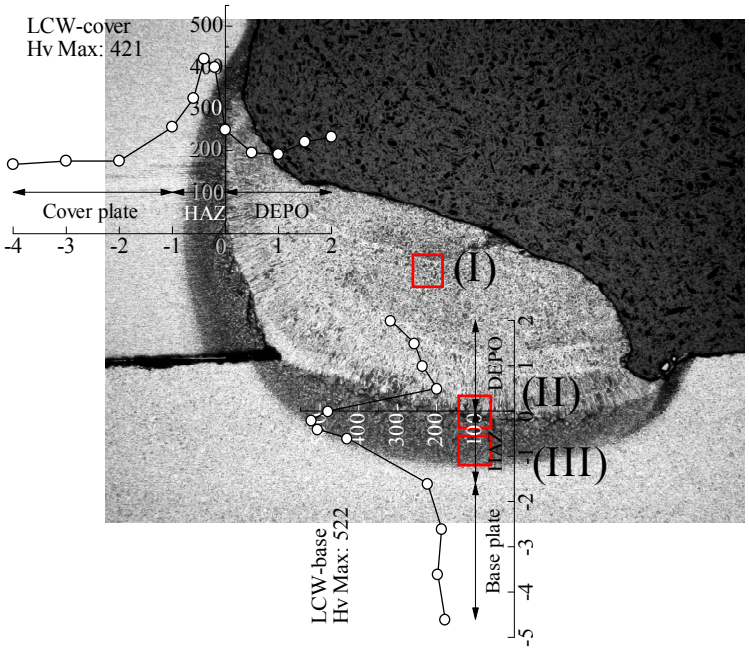

(b) LCW (underwater weld)

Fig. 2.17 Hardness distribution in welds

As shown in Fig. 2.17, hardness peaks can be found in the coarse grained region of HAZ in both in-air and underwater welds except LKA and TKA of STK400. By referring to Table 2.3, the positive correlations between hardness peak values and carbon equivalents of base steels are found to be more pronounced in underwater welds. Underwater welds on SY295 that has the

largest carbon equivalent of the three base steels show the highest hardness, 526 Hv for LYW, 522 Hv for LCW, and 514 Hv for TYW, while underwater welds on STK400 that has the lowest carbon equivalent, show only 255 Hv for LKW and 304 Hv for TKW.

Moreover, underwater welds are observed with a hardness decrease, referred to as softening, in the boundary regions between DEPO and HAZ as indicated in Fig. 2.18. Due to the rapid quenching in the wet environment, heat transfer is limited in a small region, resulting in a smaller HAZ size of 1 to 2 mm and higher HAZ hardness of 310 to 526 Hv for underwater welds, whereas they are 3 to 4 mm and 198 to 375 Hv, respectively for in-air welds.

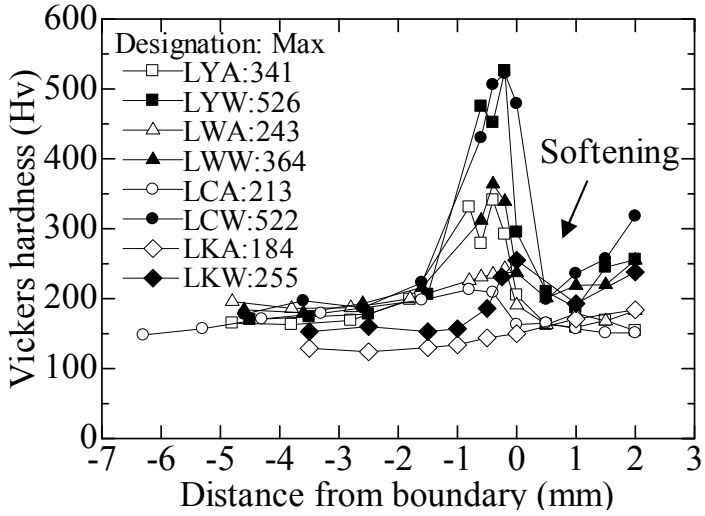

(a) Longitudinal weld

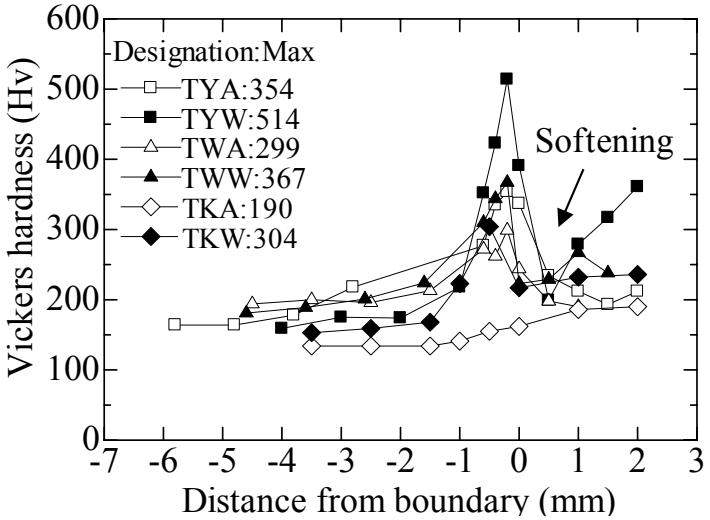

(b) Transverse weld

Fig. 2.18 Hardness distribution on the base plate side

In addition, as indicated in Fig. 2.19(b)(II), there are underbead cracks found in the boundary areas between DEPO and HAZ in underwater welds of TYW, LYW, and LCW welds, which are on SY295 and corroded SY295 steels. It should be noted that there are more underbead cracks in LCW welds than the other two. Whereas no crack is observed in underwater welds of TWW, LWW, TKW, and LKW welds, which are on SYW295 and STK400.

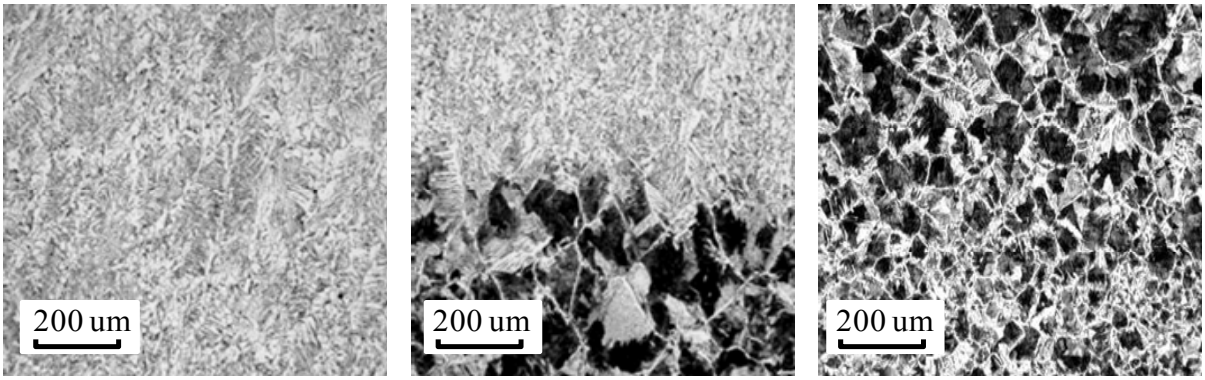

(I) DEPO (II) BOND (III) HAZ

(a) LCA (in-air weld)

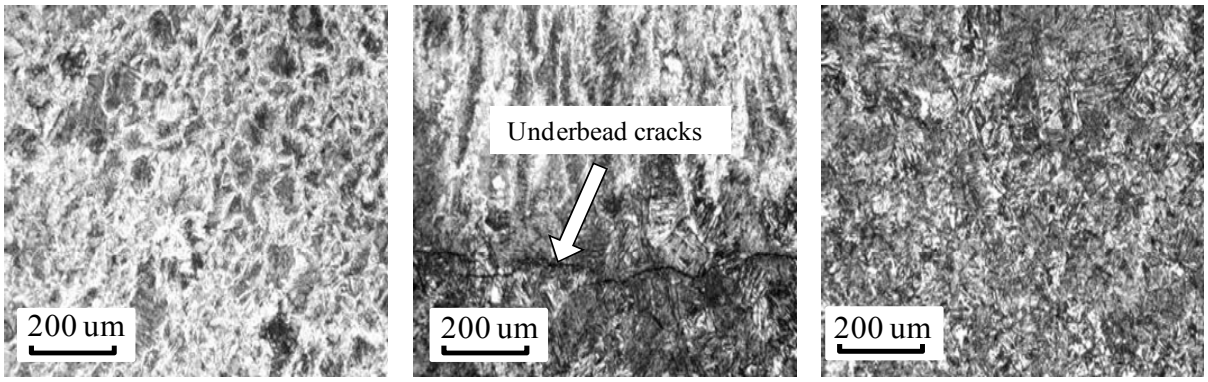

(I) DEPO (II) BOND (III) HAZ

(b) LCW (underwater weld)

Fig. 2.19 Weld microstructures

It is known that the thickness of base plate affects cooling rate and weld hardness since the base plate acts as a heat sink[2.14), 2.15)]. This can be observed in LYA and LCA. LCA welds on CSY295 with the base plate thickness varying from 6 to 8 mm have the maximum hardness of 213 Hv in HAZ, while LYA welds on SY295 with the larger base plate thickness of 12.7 mm have the maximum hardness of 341 Hv in HAZ. However, for underwater welds the thickness of

base plate has little influence on the peak hardness. As shown in Fig. 2.18(a), the hardness distributions of LCW and LYW are quite similar, and the maximum values are 522 Hv and 526 Hv, respectively. One explanation for this hardness insensitivity to the base plate thickness in the underwater welding is that the base plate, which plays an important role as a self-quenching source in open air welding, is greatly substituted by ambient water; therefore, the effect of the base plate thickness is not obvious in the underwater welding.

2.5.2 Weld Microstructures

There are similar tendencies of microstructure distributions within welds made in the same environment despite of differences in base steels. As representatives, microstructures of LCA and LCW welds are shown in Fig. 2.19. The microstructures of DEPO are shown in Figs. 2.19(a)(I) and (b)(I). DEPO in LCA is mainly composed of ferrite and pearlite with 150 Hv, and DEPO in LCW is also composed of ferrite and pearlite with hardness ranging from 180 to 300 Hv, where hardness is lower near the boundaries between DEPO and HAZ, and higher at the center of weld metal as previously shown in Fig. 2.18(a). HAZ in LCA, as shown in Fig. 2.19(a)(III), is composed of ferrite and perlite with 200 Hv, while HAZ in LCW, as shown in Fig. 2.19(b)(III), is dominated by martensite with 500 Hv. This distinct mechanical mismatching over base steel CSY295 with 150 Hv is reported to have detrimental effects to weld joints with presence of cracks in BOND regions and HAZ[2.16]. In addition, underwater welds on thinner base steels are observed to have more underbead cracks. Based on the findings in hardness distributions and weld microstructures, low ductility of LCW welds would be caused by underbead cracks and hardness mismatching in BOND regions.

2.6 CONCLUSIONS

Fillet weld joints made by underwater wet welding were studied experimentally together with their counterpart weld joints made in open air with respect to weld strength, ductility, and failure modes in this study. Differences in mechanical properties of fillet welds between in-air and underwater welds were investigated through the strength tests of fourteen weld assembly types featuring two welding environments, two base steel structural types, four base steels, two weld

orientations, and corrosion effect. The Vickers hardness tests and microstructure examinations were complemented for further insights into underwater weld joints. Main conclusions of this chapter are:

(1) Underwater fillet weld joints have larger strength but smaller ductility than their counterpart in-air weld joints. Strength increases vary from 6.9% to 41% depending on weld assembly types, while ductility decrease is about 50% for the most weld assemblies. The discount factor of 80% of weld strength for underwater environment specified in the current Japanese repair manual is on the safe side when designing the total length of underwater fillet welds.

(2) When welds change from transverse orientation to longitudinal orientation, strength increases due to underwater environment are nearly doubled from 23.7% to 41.0% on SY295 steels, tripled from 6.9% to 21.3% on STK400 steels and unchanged at around 30% on SYW295 steels.

(3) Underwater welds on corroded SY295 steel show a drastic 83% decrease in ductility factor when compared with those on virgin SY295 steels. This is caused by underbead cracks coupled with hardness mismatching which incur brittle fractures in BOND of underwater weld joints on the thinner base plate.

(4) Underwater welds have considerably larger hardness, which can be over 500 Hv, in HAZ than in-air welds, especially for sheet pile steels, and the peak hardness and carbon equivalent of base steels show a positive correlation. The thickness of base plate exhibits little influence on the hardness distribution of underwater welds, which is different from the in-air case.

(5) Although all base steel materials used in this study do not exhibit any problem in in-air welding, their underwater weldabilities depend on their carbon equivalents, and SY295 has the lowest underwater weldability among STK400, SYW295, and SY295.

REFERENCES

2.1) Perez-Guerrero, F., and Liu, S., Maintenance and repair welding in the open sea, *Welding Journal*, 84(11), pp. 54-59, 2005.

2.2) Wernicke, R. and Billingham, J., Underwater wet repair welding and strength testing on pipe-patch joints, *Journal of Offshore Mechanics and Arctic Engineering*, ASME, 120(4), pp. 237-242, 1998.

2.3) Kinugawa, J., and Fukushima, S., Influence of equivalent carbon contents of steels on proportions of martensite, hardness and susceptibility to cold cracking at coarse-grained regions in underwater wet welding, *Welding Society Journal*, 51(3), pp. 45-51, 1982 (in Japanese).

2.4) Ibarra, S., Grubbs, C. E. and Olson, D. L., Metallurgical aspects of underwater welding, *Journal of Metals*, 40(12), pp. 8-10, 1988.

2.5) Pope, A., Teixeira, J., Dos Santos, V., Paes, M., and Liu, S., The effect of nickel on the mechanical properties of high-oxygen underwater wet welds, *Journal of Offshore Mechanics and Arctic Engineering*, ASME, 118(2), pp. 165-168, 1996.

2.6) West, T. C., Mitchell, G., and Lindberg, E., Wet welding electrode evaluation for ship repair, *Welding Journal*, 69(8), pp. 46-56, 1990.

2.7) Rowe, M. D., Liu, S., and Reynolds, T. J., The effect of ferro-alloy additions and depth on the quality of underwater wet welds, *Welding Journal*, 81(8), pp. 156S-166S, 2002.

2.8) Akselsen, O. M., Fostervoll, H., Harsvaer, A., and Aune, R., Weld metal mechanical properties in hyperbaric GTAW of X70 pipeline, *International Journal of Offshore and Polar Engineering*, 16(3), pp. 233-240, 2006.

2.9) Zhang, X. D., Chen, W. Z., Ashida, E., and Matsuda, F., Metallurgical and mechanical properties of underwater laser welds of stainless steel, *Journal of Material Science & Technology*, 19(5), pp. 479-483, 2003.

2.10) Coastal Development Institute of Technology, *Port Steel Structure Corrosion-Prevention and Repair Manual*, Coastal Development Institute of Technology, Japan, 1997 (in Japanese).

2.11) Department of The Navy Naval Sea Systems Command, *U.S. Navy Underwater Cutting & Welding Manual NAVSEA S0300-BB-MAN-010*, Direction of Commander, Navy Naval Sea Systems Command, Washington, D.C., 2002.

2.12) Watanabe, N., Kitane, Y., and Itoh, Y., Modeling of joint behavior of steel pipes repaired with steel plate by underwater wet welding, *Journal of Structural Engineering*, JSCE, 55A, pp. 903-914, 2009 (in Japanese).

2.13) Suzuki, H., *Recent Welding Engineering*, Corona Publishing Co., Ltd., Tokyo, Japan, 1982 (in Japanese).

2.14) Yang, L. J., The effect of specimen thickness on the hardness of plasma surface hardened ASSAB 760 steel specimens, *Journal of Materials Processing Technology*, 185, pp. 113-119, 2007.

2.15) Shehata, F., Technical report: Effect of plate thickness on mechanical properties of arc welded joints, *Material & Design*, 15(2), pp. 105-110, 1994.

2.16) Zhang, Z. L., Thaulow, C., and Hauge, M., Effects of crack size and weld metal mismatch on the HAZ cleavage toughness of wide plates, *Engineering Fracture Mechanics*, 57(6), pp. 653-664, 1997.

CHAPTER 3
FINITE ELEMENT MODELING OF MECHANICAL BEHAVIOR OF FILLET WELDS

3.1 INTRODUCTION

In Chapter 2, an experimental study on mechanical properties of fillet welds produced underwater as well as in air was presented. The experiment was time-consuming and costly. More importantly, the test results were limited to the investigated cases. In order to predict the mechanical behavior of fillet welds with various conditions beyond the coverage of tests, the generalized model, either analytical or numerical, is considered to be convenient and necessary. Due to the complexity in material properties and geometrical features of underwater fillet welds, it is not possible to investigate them analytically but numerically. However, underwater fillet welds are rarely studied in a numerical way although the powerful computers and many well-established methodologies are readily available in current days.

Considering these situations, this chapter proposes a modeling method of underwater fillet welds in the commercial finite element package, ABAQUS[3.1)], by estimating material properties of welds from Vickers hardness and assuming a uniform cross-section along the weld bead with average dimensions. The test results from Chapter 2 are reproduced in a three-dimensional FE analysis using solid elements to model the test specimens.

A three-dimensional FE model with solid elements is more accurate to capture the actual geometrical features and usually gives numerical results more close to the experimental ones. When analyzing a specimen or a component of a structure, it is usually reasonable to employ solid elements in the FE model. However, due to the large time expense in the detailed geometrical modeling as well as in the numerical computation, the FE model with solid elements is not efficient when a complex structure is analyzed, especially, those with hundreds and thousands of components. In this case, structural elements, such as beam elements, shell elements, etc. are more preferable in the FE model as long as they can well represent mechanical behavior of the component of concern.

Therefore, for the sake of the future usage in analyzing welded structures, a three-dimensional FE model with shell elements and connector elements is proposed taking advantage of the experimental results of fillet welds presented in Chapter 2. The weld model is then validated against the theoretical results of stress distributions in longitudinal fillet welds as well as the experimental results from the welding patch repaired pipes.

3.2 FE MODEL WITH SOLID ELEMENTS

The main objective of the FE analysis presented in this section is to develop finite element modeling procedures for underwater fillet welds, which can reproduce the experimental results and predict mechanical behavior of underwater fillet welds which are not examined in the experimental study.

Without introducing significant errors, HAZ is usually neglected in the FE model when analyzing in-air welds. However, it is the critical part to distinguish mechanical properties of underwater welds from those of in-air welds, and the modeling of HAZ in underwater welds is indispensable in order to predict their mechanical behavior accurately. For FE analysis, material properties of HAZ need to be prepared in the form of stress-strain relationships as input data. In this study, the yielding stress and the tensile strength of materials in welds are estimated from Vickers hardness values by using available empirical relationships. In the following, the constitutive relationships of HAZ and DEPO are derived from Vickers hardness values, and then geometric features of underwater weld details are modeled.

3.2.1 Constitutive Relations of HAZ and DEPO

This study assumes stress-strain relationships of HAZ and DEPO follow the power law as:

$$\sigma_t = A\varepsilon_t^n \tag{3.1}$$

where, σ_t is true stress, ε_t is true strain, n is hardening exponent, and A is hardening coefficient. To determine the power law in Eq. (3.1), three parameters are required: hardening exponent n, hardening coefficient, A, which defines the shape of the material constitutive curves, and true fracture strain ε_t^f or true fracture stress

σ_t^f, either of which defines the ending point of the material constitutive curves. Based on empirical equations proposed by Akselsen et al.[3.2)], the hardening exponent n can be determined from the cooling time of steel from 800°C to 500°C, $t_{8/5}$, as:

$$n = 0.065(t_{8/5})^{0.17} \tag{3.2}$$

where, $t_{8/5}$ is a function of Vickers hardness and chemical compositions of the metal, the derivation of $t_{8/5}$ from Vickers hardness and chemical compositions can be found in detail in Watanabe et al.[3.3)]. Hardening coefficient A, according to Eq. (3.1), can be derived as:

$$A = E^n / (\sigma_t^y)^{n-1} \tag{3.3}$$

where, E is Young's modulus of steel, and σ_t^y is true yielding stress, which can be estimated by the empirical equation from Akselsen et al.[3.2)] as:

$$\sigma_n^y = 3.1H_v(0.1)^n - 80 \tag{3.4}$$

where, σ_n^y is nominal yield stress in MPa, and H_v is Vickers hardness value.

The third parameter, ε_t^f, can be obtained from Eq. (3.5) which is derived from regression analysis based on the test data by Suzuki and Tamura[3.4)]. The regression curve and the test data are plotted in Fig. 3.1.

$$\varepsilon_t^f = 14.78\exp(-4.15\times10^{-3}UTS) \tag{3.5}$$

where, UTS is the ultimate tensile strength in terms of engineering stress in MPa, and can be obtained using Eq. (3.6) for HAZ and Eq. (3.7) for DEPO, which are proposed by Akselsen et al. in Ref. 3.2) and Ref. 3.5), respectively.

$$UTS_{(\mathrm{HAZ})} = 3.5H_v(1-n)\left(\frac{12.5n}{1-n}\right)^n - 92 \tag{3.6}$$

$$UTS_{(\mathrm{DEPO})} = 3.5H_{\mathrm{v}}(1-n)\left(\frac{12.5}{1-n}\right)^{n} - 50 \tag{3.7}$$

Given Vickers hardness values, the stress-strain relationship of HAZ and DEPO can be determined for the weld of interest based on the above equations.

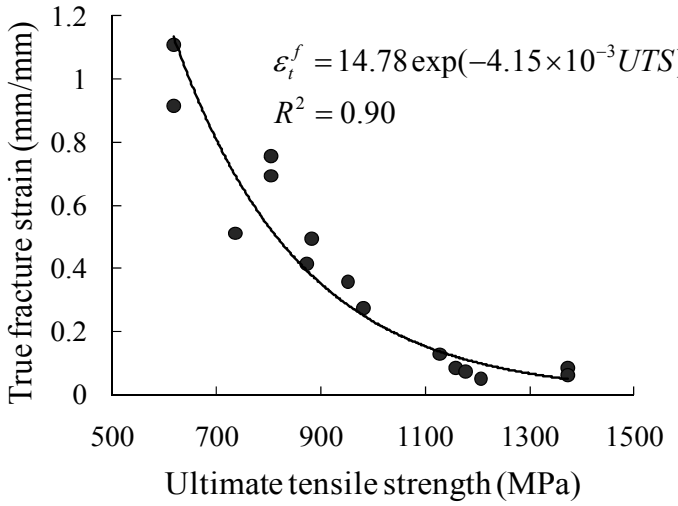

Fig. 3.1 Proposed equation using test data by Suzuki and Tamura[3.4)]

3.2.2 Geometric Models

Another difficulty in modeling is geometric complexity of welds. Modeling a precise weld bead is time consuming, hence, in this study, weld leg lengths, *h* and *w*, and weld throat, *a*, are used to define a weld cross section, which is assumed to be uniform along the weld bead. Weld penetrations and the regions with hardness softening in underwater welds are simplified as shown in Fig. 3.2. The size of each region is determined from pre-fracture macrostructural examination of specimens described in Chapter 2. The regions of penetration and softening are assumed to have the same chemical compositions as the weld metal even though the fusions from parent steel could change the chemical compositions in these parts to a small extent[3.6)].

Strictly speaking, specimens are not symmetric in geometry about the center lines or the mid-plane of the base steel due to geometrical differences among welds. However, for computational efficiency, only 1/8 of each specimen is modeled as shown in Fig. 3.3 by assuming the

asymmetry is too small to affect the overall mechanical behavior of welds, and by taking advantage of symmetries. In addition, the weld dimensions used in the FE analysis are the average values of all weld beads in the concerned specimen. Element type is C3D8R in the model.

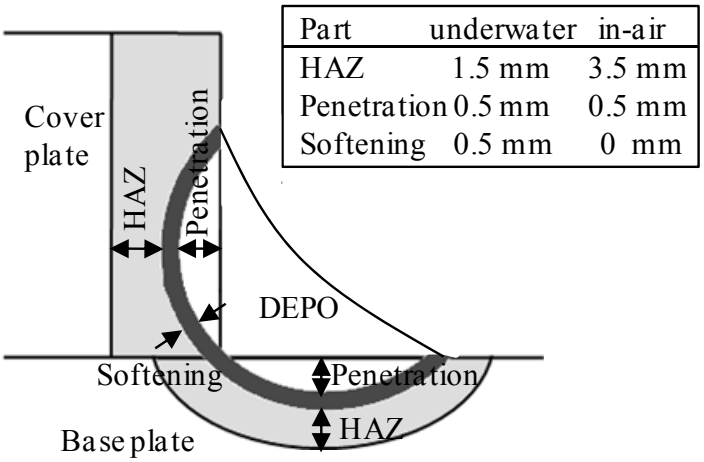

Part	underwater	in-air
HAZ	1.5 mm	3.5 mm
Penetration	0.5 mm	0.5 mm
Softening	0.5 mm	0 mm

Fig. 3.2 Geometrical model for welds

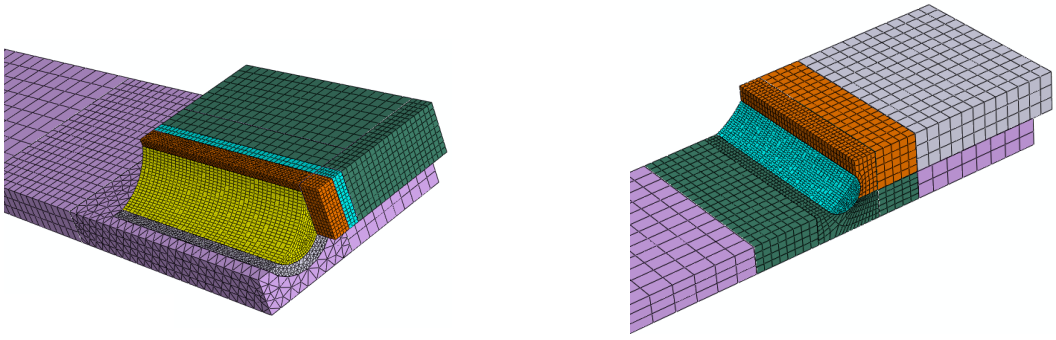

(a) Longitudinal fillet weld (b) Transverse fillet weld

Fig. 3.3 1/8 FE model of weld specimens

3.2.3 Finite Element Analysis Results

Applied load-weld deformation curves from analyzed results are plotted in Fig. 3.4 together with representative experimental results for weld specimens TKA3, TKW4, LYA1, and LCW2. It is found that generally, the FE model proposed in this study can predict the maximum load of a fillet welded specimen with good accuracy. In all examined cases, errors are found to be less than 10% of the test results.

Fracture deformation of longitudinal welds is predicted within 30% error, and that of transverse welds is considerably overestimated especially for underwater welds. This may be explained by a uniform stress distribution due to a uniform cross section along the transverse weld bead in the analyzed model. The uniform stress distribution causes every cross section along the bead to fracture simultaneously, resulting in larger weld deformation than that obtained in the experiment, where cross sections of a weld bead are actually not uniform along the weld bead and the failure of weld may not occur simultaneously at every cross section.

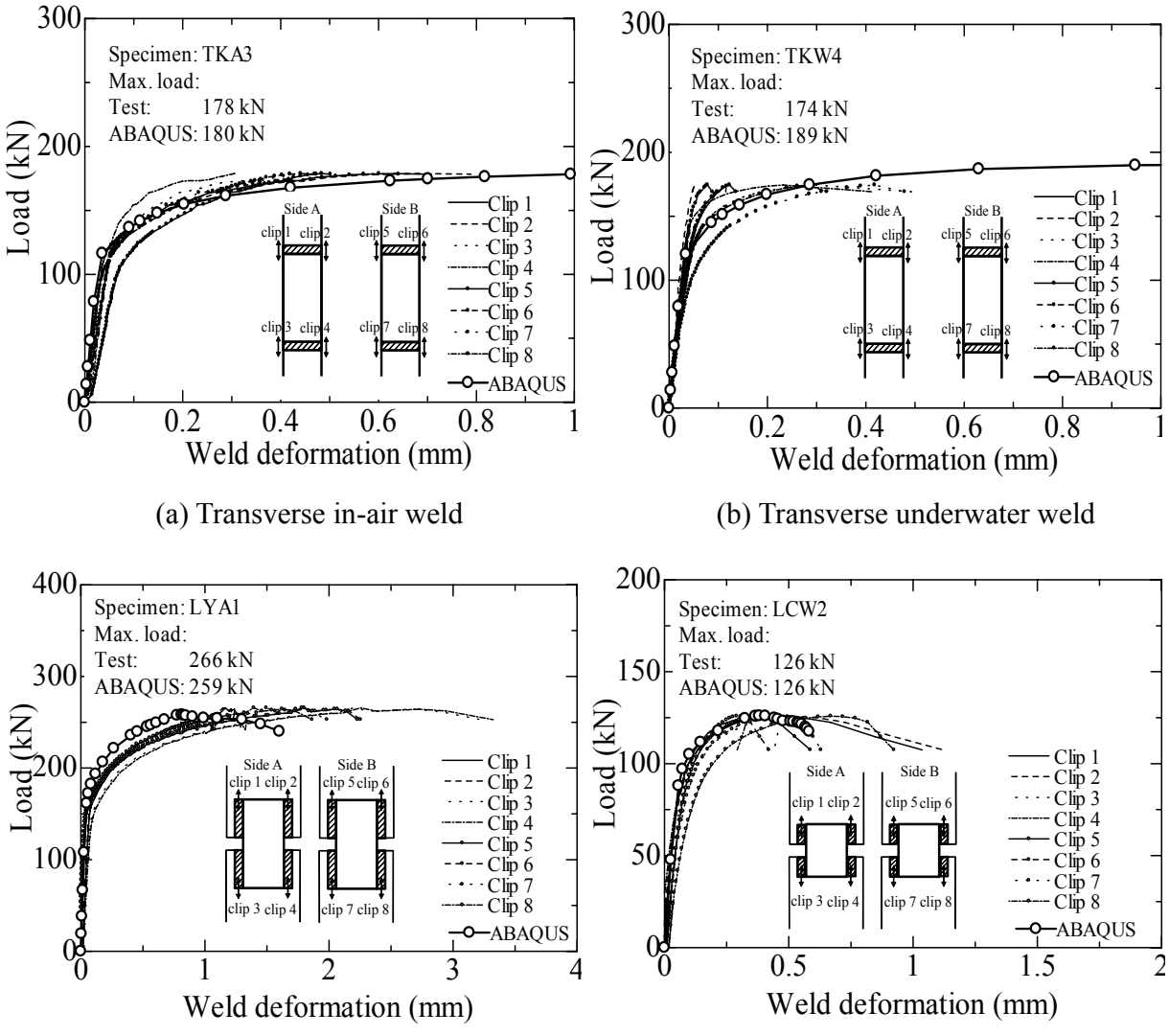

(a) Transverse in-air weld

(b) Transverse underwater weld

(c) Longitudinal in-air weld

(d) Longitudinal underwater weld

Fig. 3.4 Comparison of load-deformation relationships between experiment and FEA

3.3 FE MODEL WITH STRUCUTRAL ELEMENTS

Section 3.2 proposed a weld model using solid elements in elastic-plastic analysis, and that model could predict the maximum load of fillet welds with good accuracy. It is, however, not easy to use for the complex structures. To model fillet welds in structural analyses, Kitane et al.[3.7] used elastic beam elements to model fillet welds in welding patch repaired pipes and obtained good agreement with experiments when predicting the load-carrying capacity of repaired pipes; Khedmati et al.[3.8] used elastic-perfectly plastic shell elements to model fillet welds when studying the stiffened plates under in-plane axial compression. These two weld models failed to predict both the post-peak response and the possible failure of fillet welds, which would have significant influence on the stress redistribution and mechanical behavior of repaired structures once fillet welds fail.

In the repair design of corrosion-damaged offshore steel structures such as pipe piles, weld size and total length are determined by assuming that weld joints are too stiff and strong to have nonlinear behavior, and that base and patch plates would fail before welds fracture. However, with a study purpose to compare effectiveness of different weld patterns and to further assess the current repair design, there may be some cases where welds show nonlinear behavior or even fail, which is not expected according to the current design.

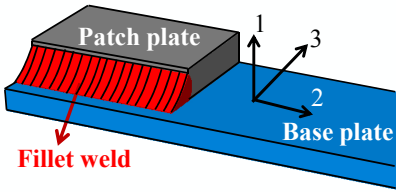

(i) 3D view

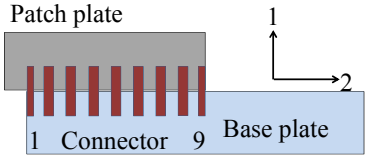

(ii) Analyzed model (side view)

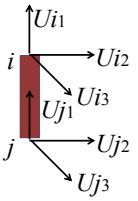

(iii) Connector element

(a) Longitudinal weld

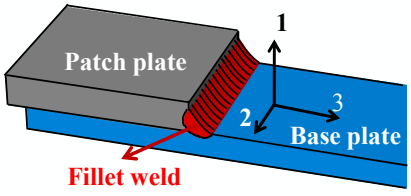

(i) 3D view

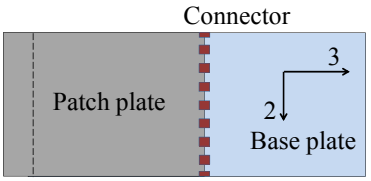

(ii) Analyzed model (top view)

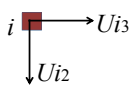

(iii) Connector element

(b) Transverse weld

Fig. 3.5 Weld model by connector elements

This section proposes a weld model to represent a nonlinear response of fillet welds to failure, which can be used in a complex structural model. In this model, a fillet weld bead is modeled as a number of connector elements, as shown in Fig. 3.5. Two steel plates are modeled using shell elements with surface contact, and the element type is S4. Due to geometrical and loading symmetry, 1/8 model is constructed and symmetrical boundary constrains are applied to the model. Connector element used is CONN3D2, a three-dimensional, 2-node element available in ABAQUS[3.1)], and the connector has three independent translational components, U_1, U_2, and U_3 in local Cartesian directions. Connector properties are defined in the form of an applied load-relative displacement curve for each translational component as shown in Fig. 3.6.

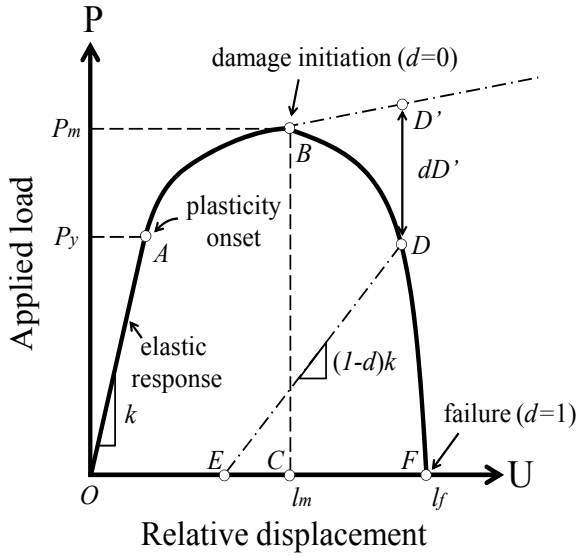

Fig. 3.6 Connector behavior[3.1)]

Connector behavior of each displacement component is determined by mechanical properties obtained in weld strength tests. Because the current study is focused on steel pipe piles, mechanical properties of fillet welds made on STK400 steels with SM400 patch plate are summarized from the weld strength test presented in Chapter 2 and they are shown in Table 3.1. The modeling procedures of connector behavior are as follows:

(1) The elastic response *OA* is characterized by linear stiffness $k=l_c \times k_{w0}$, where l_c is the weld bead length that is represented by one connector element;
(2) The plasticity onset Point *A* is determined by *k* and the yielding load $P_y=\sigma_y \times l_c \times a$, where *a* is

the size of weld throat;

(3) Point B is the maximum load point determined by $P_m=\sigma_w\times l_c\times a$, and l_m is the displacement equal to $\gamma_m\times 1.41a$;

(4) A power relation is assumed between Points A and B;

(5) Point B is also referred to as the damage initiation point with a damage index d=0. Beyond this point, e.g. Point D, the stiffness and load-carrying capacity of the defined component in the connector degrade from the undamaged state D', resulting in a softening post-peak response curve BDF, which is assumed to be a quarter of a sine curve decreasing from the peak load point B to the zero load point F with the increase of the relative displacement of the component in the connector;

(6) Point F, referred to as the failure point with a damage index d=1, is determined by the fracture displacement $l_f=\gamma_f\times 1.41a$, where the stiffness and the load-carrying capacity of the component in the connector become zero, and the connector element will be removed from the mesh in the analysis.

Table 3.1 Mechanical properties of fillet welds

Parameters*	In-air		Underwater	
	Transverse	Longitudinal	Transverse	Longitudinal
Stiffness k_{w0} (kN/mm/mm)	31	14	41	14
Yielding stress σ_y (MPa)	433	193	443	265
Weld strength σ_w (MPa)	553	324	591	393
Ductility factor γ_m	0.15	0.32	0.10	0.16
Ductility factor γ_f	0.16	0.41	0.12	0.19

*Note: k_{w0} is the weld stiffness in loading direction per unit length of a weld bead; σ_y is determined by 0.2% offset value; σ_w is the maximum applied load divided by weld throat area; γ_m is the weld deformation at the maximum applied load divided by weld size; and γ_f is the weld deformation at weld fracture divided by weld size.

Three translational components of displacement, U_1, U_2, and U_3, in the connector are assumed to be mechanically independent until one of them reaches the failure. The force-displacement relationship in the direction of U_2 is determined by mechanical properties of longitudinal welds, and that of U_3 is determined by those of transverse welds. The force-displacement relationship of

U_1, which is not available from the weld strength test, is assumed to be the same as that of $U3$. For rotational components in connector elements, several trail analyses are performed before considering different rotational stiffness of the components in the connectors, and it is found that whether there is rotational component or not does not affect the connector responses presented in this study. Therefore, the rotational components are not included in connector elements.

It is noted that although ABAQUS provides spring elements with nonlinear behavior by giving pairs of force-relative displacement to any degree of freedom[31.)], this study do not use spring elements to simulate fillet welds. This is based on the concern that ABAQUS assumes that the force remains as a constant with a value corresponding to the endpoint of the force-relative displacement curve. This results in a zero stiffness response but the load carried in the elements is not zero. However, the actual fillet welds after failure requires both stiffness and load carrying capacity of their simulating elements to be zero. This function can be realized by specifying the failure point F as shown in Fig. 3.6 in connector elements and thereafter they can be removed from the model, representing the failure of the fillet welds.

3.4 MODEL VALIDATION

An initial validation of the proposed weld model using connector elements is carried out for shear stress distribution in longitudinal fillet welds. Then, experimental results of two repaired pipes subjected to a compressive loading are used to further validate the model.

3.4.1 Stress Distribution in Longitudinal Fillet Welds

A theoretical distribution of shear stress in a longitudinal fillet weld in the elastic phase can be calculated by an existing formula[3.4)], and it is compared with results from FE analysis using the proposed weld model. A longitudinal fillet weld with a weld length of 40 mm is modeled by nine connector elements with a throat size a=4.2 mm. Two connector elements at the end of weld beads, as indicated as "1" and "9" in Fig. 3.5(a)(ii), are specified with l_c=2.5 mm, and the other seven connector elements are specified with l_c=5 mm. Comparisons of shear stress distributions at different applied load levels in connector "1", as noted as P_1, are shown in Fig. 3.7. The shear stress in longitudinal fillet welds is normalized by yielding stress of longitudinal fillet welds

made underwater, i.e, 265 MPa as shown in Table 3.1. It is found that distributions from the FE analysis have good agreement with the theoretical ones along the weld bead although there is a small overestimation of about 6% at the end of the weld bead in the relative location "1".

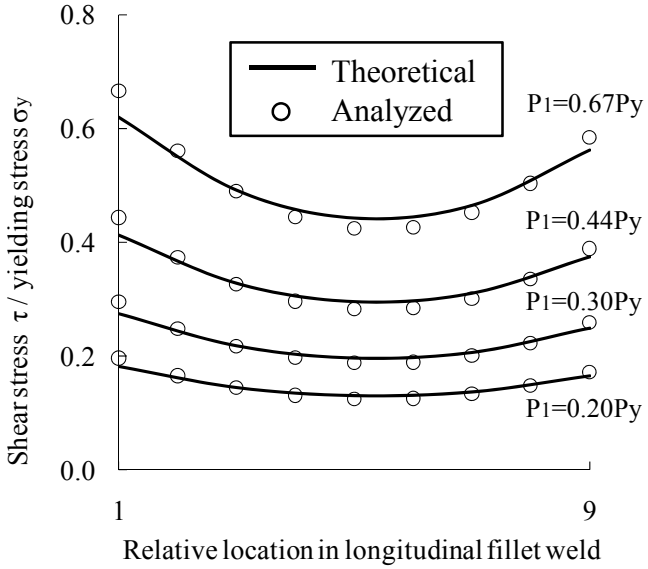

Fig. 3.7 Comparison in shear stress distributions in elastic phase

3.4.2 Validation against Repaired Pipe Tests

Results from compressive tests of repaired pipes from Ref. 3.7) are used for further validation on the proposed weld model. Two specimens, KA2C and KW2C, with welds made in air and underwater, respectively, are selected. These two specimens have the same dimensions, and are indicated as Type #0 as shown in Fig. 3.8(a). The uniform thickness reduction in the pipe, Δt, is 6 mm, the length of a thickness-reduced portion ($=2l_r$) is 150 mm, and the thickness of patch plate t_p is 6 mm. Other parameters can be found in Table 3.2. In the FE analysis, fillet welds are modeled by connector elements as proposed, and groove welds used to joint two patch plates are modeled by shell elements with a thickness of 9 mm. The yielding stress of groove welds is estimated to be 600 MPa by assuming Vickers hardness of 200 Hv. Welding details and its modeling are illustrated in Fig. 3.8(b).

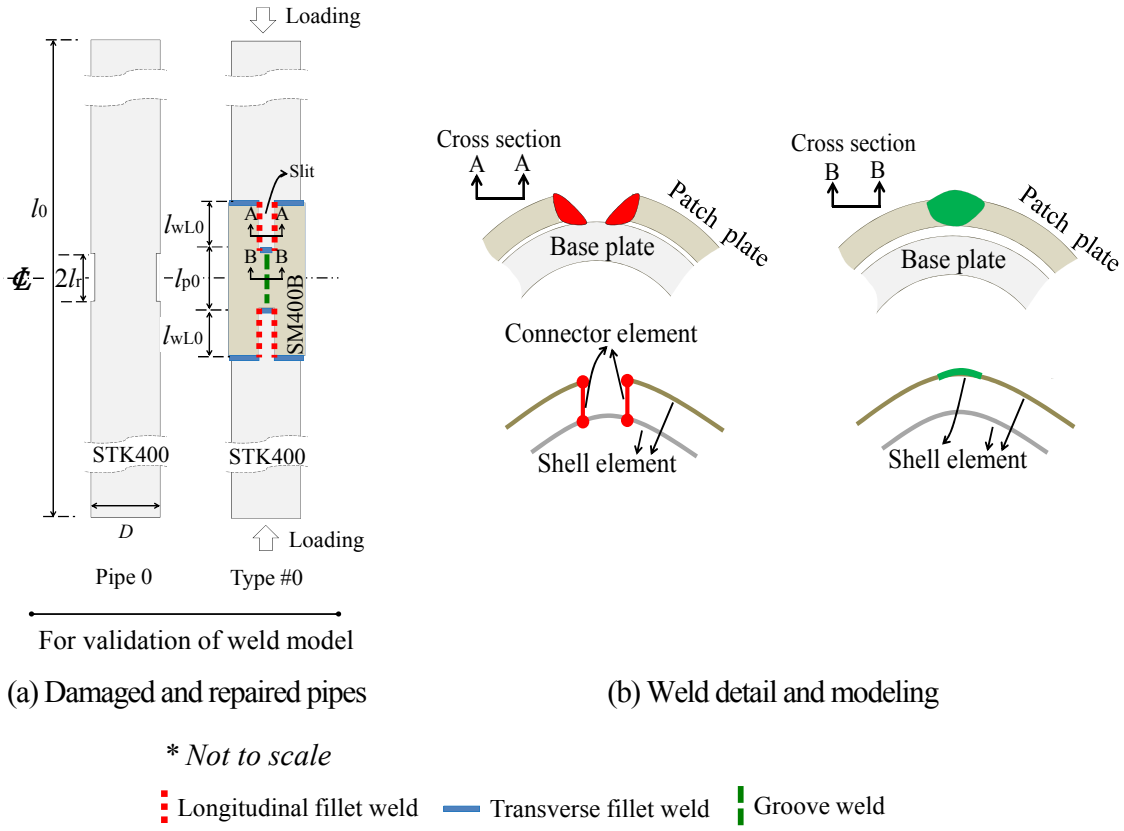

(a) Damaged and repaired pipes (b) Weld detail and modeling

Fig. 3.8 Examined pipes and weld details

Table 3.2 FE model information in the model validation analysis

Pipe	Pipe length	Pipe outer diameter	Wall thickness	D/t_b ratio	Theoretical yielding load	Theoretical shortening at yielding load	Stiffness of intact pipe with $2l_r$'s length	Repair type	Length of each weld line	No. of slits
	l_0 (mm)	D (mm)	t_b (mm)		P_{y0} (kN)	δ_{y0} (mm)	K_{r0} (kN/mm)		l_{wL0} (mm)	n
Pipe0	1,300	216.7	12.3	17.6	2,815	2.32	10,684	#0	140	2

A quarter of specimen is modeled taking advantage of symmetry in the structural geometry as well as the loading condition. The size of weld throat used in the analysis is the measured value in the tests. Results from FE analysis are compared with those from the tests as shown in Fig. 3.9. In the test, pipe shortening was measured for a length of 1,300 mm, and weld deformation was measured by clip gauges placed on transverse welds at the end of patch plates as indicated in Fig. 3.10(b). Applied load P and pipe shortening δ are normalized by the theoretical yielding load of the intact pipe P_{y0}=2,815 kN, and the corresponding theoretical yield shortening δ_{y0}=2.32 mm, respectively, as listed in Table 3.2.

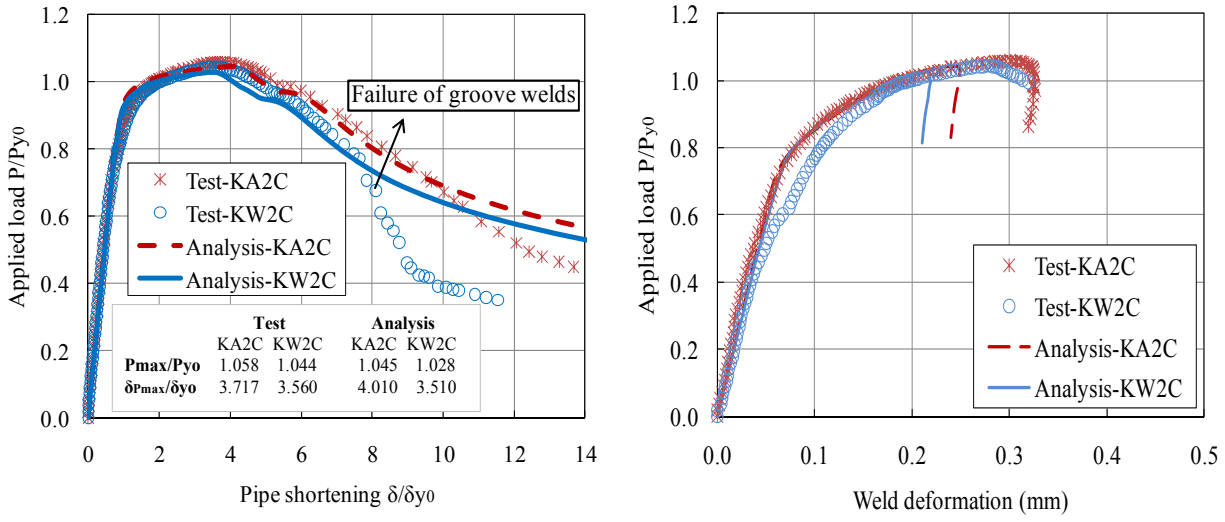

(a) Global responses of repaired pipes (b) Local responses of weld deformation

Fig. 3.9 Results comparison of the model validation tests

It can be found that the FE analyses with the proposed weld model predict global responses of two repaired pipes very well as shown in Fig. 3.9(a) until pipe shortening δ/δ_{y0} is about 8 for KW2C and 10 for KA2C. A sudden decrease in the applied load in the test of KW2C at δ/δ_{y0}=8 was found to be caused by the failure of groove welds, which are not considered to fail in the current FE model. As for the local responses of fillet welds, it is found that the overall transverse weld behavior is predicted well as shown in Fig. 3.9(b) although there is an underestimation of the maximum weld deformation by about 20%.

A contour plot of equivalent plastic strains from the FE analysis at P/P_{y0}=0.8 in the post-peak phase as shown in Fig. 3.10(c) is used to examine failure mode of KW2C. It is found that both the test and the analysis show that local buckling occurs at the thickness-reduced portion and that fillet welds fail at the corner of a slit in patch plates. An examination on the damage index d of fillet welds in the analysis, as shown in Fig. 3.11, indicates that transverse weld elements #1 and #2 in the inner transverse weld line as indicated in Fig. 3.10(d) reach their ultimate load first at δ/δ_{y0}=3.64. The longitudinal weld #1 adjacent to them then reaches the ultimate load at δ/δ_{y0}=4.33, followed by the longitudinal weld #2 at δ/δ_{y0}=5.95. A transverse weld line on a patch plate which constitutes a re-entrant corner of a slit is referred to as an inner transverse weld.

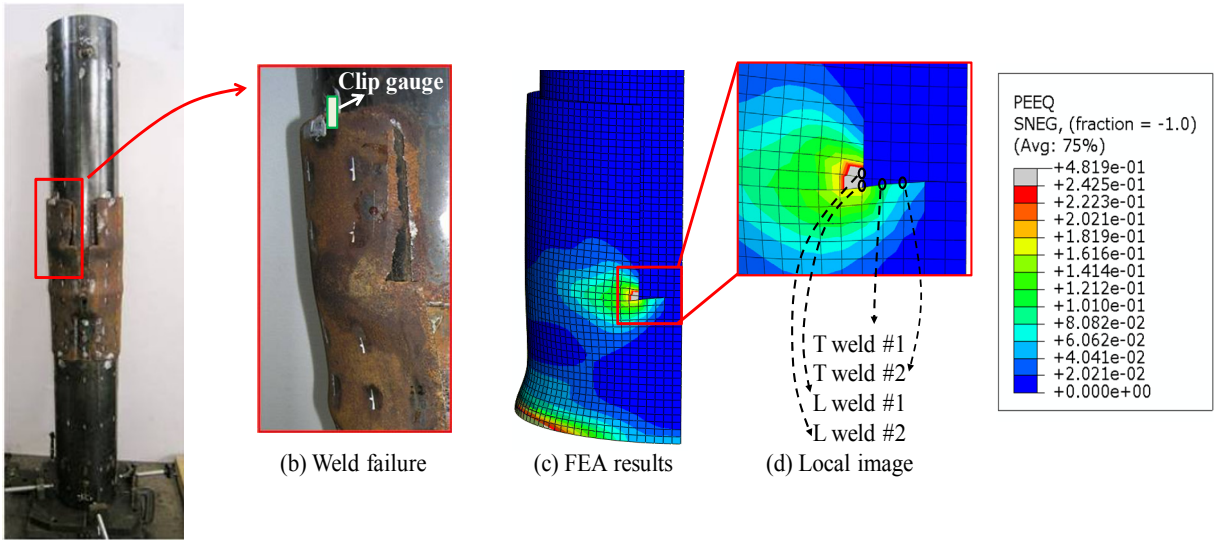

(a) Tested KW2C (b) Weld failure (c) FEA results (d) Local image

Fig. 3.10 Comparison of failure modes

By comparing with δ_{pmax}, pipe shortening at P_{max}, It is found that the repaired pipe, KW2C, reaches its maximum load when local buckling of the thickness-reduced portion of the pipe occurs at $\delta_{pmax}/\delta_{y0}$=3.51, and that buckling causes deformation of the pipe to increase. The increased relative deformation between the pipe and patch plates triggers the failure of the inner transverse weld, and the adjacent longitudinal weld then becomes the damage-front. After that, weld failure progresses along the longitudinal weld bead, causing a total failure of the repaired pipe.

It is noted that although the failure of groove welds is not modeled in the analysis, it is possible to estimate the occurrence of the failure. From the FE analysis, it is found that the equivalent plastic strain of 5.7% at groove welds obtained from KW2C at δ/δ_{y0}=8, as indicated in Fig. 3.9(a), can be used as a criterion, which will be employed in the comparative numerical study presented in the next chapter.

In the validation against both theoretical solutions and experimental results, it was shown that the proposed weld model is capable of predicting nonlinear behavior of fillet welds to failure as well as global strucutral responses of repaired pipes under compression.

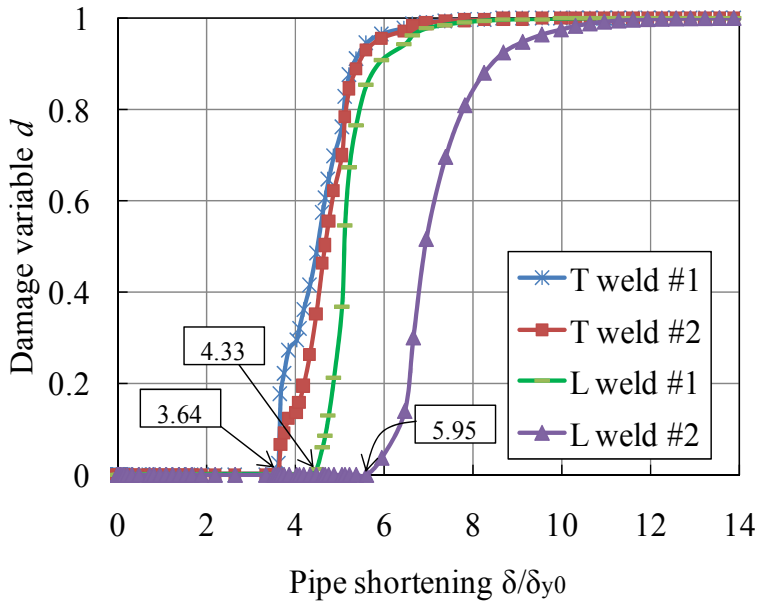

Fig. 3.11 Damage progress of fillet welds in KW2C

3.5 CONCLUSIONS

This chapter proposed a method to estimate material properties of underwater welds according to their Vickers hardness and chemical compositions, and then a three-dimiensinal FE model with solid elements was constructed to reproduce the experimental results presented in Chapter 2. In addition, a FE model of fillet welds with connector elements, facilitating the structural analysis, was proposed and validted against the thoretical and experiemntal results. The findings of this chapter are summerized as follow:

(1) By estimating material properties of welds from Vickers hardness and assuming a uniform cross-section along the weld bead with average dimensions, the maximum load of fillet weld joints can be accurately predicted in the FE analysis for both in-air dry and underwater wet welds.

(2) The proposed fillet weld model using connector elements is accurate in representing the mechanical behavior of fillet welds and can be used in the analysis of welded structures where nonlinear behavior of welds may be important.

When weld geometry and materials are different from the examined conditions as presented in this study, it is possible to predict the load-displacement relationships up to the maximum load of underwater fillet welds using the same procedure proposed in the solid element model. Once the relationships are obtained and generalized, the connector weld model can be used to estimate the

mechanical behavior of welded structures. Two proposed models used in the finite element analysis pave the way for numerical study on underwater fillet weld joints, and the weld model using connector elements will be used in the following research of this study.

REFERENCES

3.1) Dassault Systèmes Simulia Corp. *ABAQUS/Standard user's manual*, *version* 6.8, 2008.

3.2) Akselsen, O.M., Rorvik, G., Onsoien, M.I., and Grong, Ø, Assessment and predictions of HAZ tensile properties of high-strength steels, *Welding Journal*, 68(9), pp. 356-362, 1989.

3.3) Watanabe, N., Kitane, Y., and Itoh, Y., Modeling of joint behavior of steel pipes repaired with steel plate by underwater wet welding, *Journal of Structural Engineering*, JSCE, 55A, pp. 903-914, 2009 (in Japanese).

3.4) Suzuki, H. and Tamura, H., Weldability of high-strength steels evaluated by ductility test on synthetic heat-affected zone, *Iron and Steel*, 47(3), pp. 482-484, 1961 (in Japanese).

3.5) Akselsen, O. M. and Grong, Ø., Prediction of weld metal Charpy V notch toughness, *Materials Science and Engineering*, A159, pp. 187-192, 1992.

3.6) Mellor, B. G., Rainey, R. C. T., and Kirk, N. E., The static strength of end and T fillet weld connections, *Materials and Design*, 20, pp. 193-205, 1999.

3.7) Kitane, Y., Itoh, Y., Watanabe, N., and Matsuoka, K., Compressive and flexural tests of thickness-reduced steel pipes repaired with patch plates using underwater wet welding, *Journal of Structural Engineering*, JSCE, 55A, pp. 889-902, 2009 (in Japanese).

3.8) Khedmati, M. R., Rastani, M., and Ghavami, K., Numerical study on the permissible gap of intermittent fillet welds of longitudinally stiffened plates under in plane axial compression, *Journal of Constructional Steel Research*, 63, pp. 1415-1428, 2007.

CHAPTER 4
NUMERICAL STUDY ON PIPE PILES REPAIRED BY PATCH WELDING UNDER COMPRESSION

4.1 INTRODUCTION

Due to its high efficiency and cost-effectiveness, patch plate welding in underwater wet environment is commonly used in repairing offshore and port steel strucutres[4.1), 4.2)]. The current repair design manual in Japan, *Port Steel Structure Corrosion-Prevention and Repair Manual*, was issued in 2009[4.3)], where the major update from its previous version was the change of design concept from allowable stress design to reliability based design. Regarding the patch plate welding repair, there is also a change where the discount rate of weld strength due to field welding is set to 10% in place of its previous value of 20%[4.3), 4.4)]. Since the discount rate due to underwater welding environments is 20%, weld strength of field underwater welding is specified as 70% of that of in-air shop welding, which was 60% in the previous manual.

To examine how much strength underwater welds have, a series of double-lapped joint tests on fillet welds was presented in Chapter 2, and it was found that underwater fillet welds, depending on their base steels, have a strength increase ranging from 6.9% to 41% and a ductility decrease of about 50% compared with their counterpart in-air welds, implying that the current manual is on the safe side by discounting underwater weld strength by 20% from in-air weld strength.

However, this does not mean the current repair design is perfect. On the contrary, there are still some other issues which need to be examined to achieve structurally efficient and cost-effective repair design. The first issue is the welding pattern. A required thickness of a patch plate and a required weld length can be determined according to the current repair design manual when a corrosion-damaged structure is given. However, different welding patterns can be designed to provide the required weld length. The choice of the welding pattern appears to be arbitrary and is largely dependent on the preference of the individual designer because there is no provision or guidance provided for the repair design. The situation is basically due to the fact that how the

difference in welding patterns would change structural performance and which pattern gives better structural performance are not understood yet.

The second issue is the minimum required thickness of patch plates for the given corrosion-damaged structure to recover its original stiffness and strength. According to the current design, the thickness of patch plates can be determined based on the load share ratio of patch plates, which is assumed to be equal to a ratio between the patch thickness t_p and the summation of the patch thickness t_p and the residual thickness t_r of the corroded base steel, i.e., the load share ratio of patch plates equals to $t_p/(t_p+t_r)$. This concept is simple and easy to apply in the repair design, but the rationality is questionable because the different welding patch patterns may change the load transfer paths and consequently change the structural performance of the repaired system, resulting in different load share ratios. Moreover, due to the deformation of welds and in the patch plate, the actual load shared by patch plates should be smaller than the design calculation, where rigid welds and equal strains in base and patch plates are implicitly assumed.

The third issue is the contribution of transverse fillet welds to structural performance of a repaired structure by welding patch plates. It is specified in the repair design manual that the strength of transverse welds is not counted when determining a total length of fillet welds in design, although transverse welds are usually provided in the repair to make the corrosion-damaged portion watertight. It is necessary to check whether this treatment is too conservative in the design and whether the reduction of the total weld length by counting the transverse welds is possible to cut down the repair cost.

To have better understanding on these issues, this chapter presents a comparative numerical study on the compressive behavior of repaired pipe piles with different welding patterns, taking advantage of the fillet weld model proposed in Chapter 3. Four baseline repair designs with different welding patterns to repair the thickness-reduced steel pipe piles are modeled. The structural behavior of the repaired pipe piles under compression is examined in terms of stiffness, load-carrying capacity as well as failure modes. Through the comprehensive study, design implications are highlighted and the complementary analytical study is followed towards a more efficient repair of pipe piles by patch welding.

4.2 EXAMINED REPAIR DESIGNS

When designing a patch plate repair for corrosion-damaged pipe piles, there can be different welding patterns as long as a total length of longitudinal welds meets design requirements of the current repair manual. In this section, how different welding patterns affect structural performance of pipe piles repaired by welding patches is examined by FE analysis.

A uniform thickness reduction in a portion of a pipe pile is assumed to represent corrosion damages. Four possible welding patterns are examined to repair six pipe piles with different dimensions as listed in Table 4.1.

Table 4.1 FE model information of comparative study

Pipe	Pipe length l_0 (mm)	Pipe outer diameter D (mm)	Wall thickness t_b (mm)	D/t_b ratio	Theoretical yielding load P_{y0} (kN)	Theoretical shortening at yielding load δ_{y0} (mm)	Stiffness of intact pipe with $2l_r$'s length K_{r0} (kN/mm)	Repair type	Length of each weld line l_{wL0} (mm)	No. of slits n
Pipe1	3,360	300.0	14.0	21.4	4,554	5.99	5,104	#1	1,180	0
								#2	880	2
								#3	440	4
								#4	220	8
Pipe2			12.0	25.0	3,930		4,406	#1	1,180	0
								#2	880	2
								#3	440	4
								#4	220	8
Pipe3	5,600	500.0	14.0	35.7	7,738	9.99	8,674	#1	1,760	0
								#2	1,460	2
								#3	730	4
								#4	370	8
Pipe4			12.0	41.7	6,660		7,465	#1	1,760	0
								#2	1,460	2
								#3	730	4
								#4	370	8
Pipe5	7,860	700.0	14.0	50.0	10,922	14.02	12,243	#1	2,340	0
								#2	2,040	2
								#3	1,020	4
								#4	510	8
Pipe6			12.0	58.3	9,389		10,525	#1	2,340	0
								#2	2,040	2
								#3	1,020	4
								#4	510	8

Examined pipe piles with thickness reduction are designated as Pipe 1, 2, 3, 4, 5, and 6, and their four repair designs are Type #1, #2, #3, and #4 as illustrated in Fig. 4.1(a). Outer diameters and wall thicknesses of pipe piles are selected from JIS A5525 for the pipe pile SKK400, which is a typical type of piles used in offshore structures in Japan. Parameters listed in Table 4.2 are fixed for all pipe piles in the study. A uniform thickness reduction Δt is set to 6 mm by assuming 20 years' corrosion at a severe splash zone with a length of 500 mm at offshore environment, where a corrosion rate of 0.3 mm/year is expected[4.3)]. Slenderness ratio is set to 16.5 to avoid global buckling at a specified threshold value of 18 for SKK400 steels[4.3)].

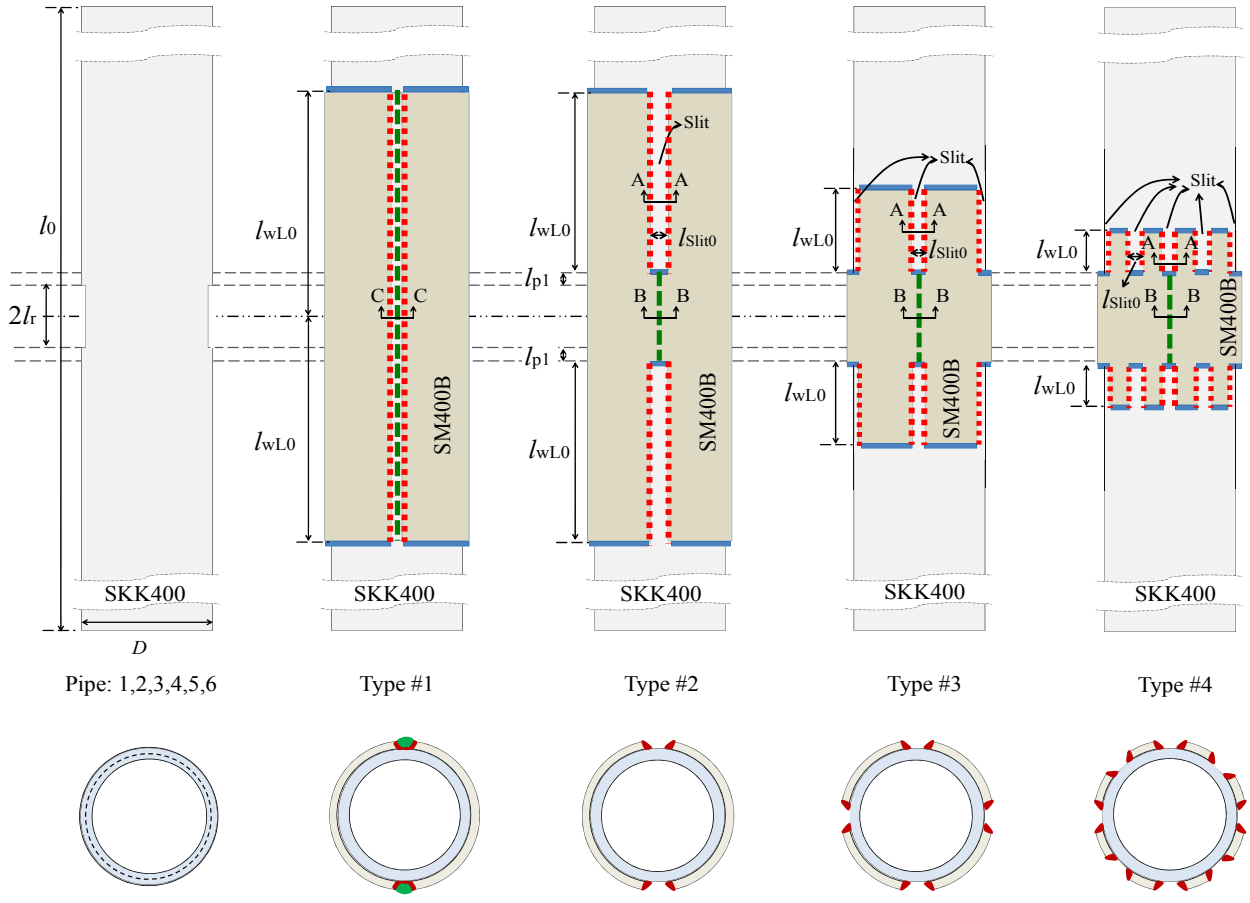

(a) The thickness-reduced and the repaired pipe piles with different welding patterns

Fig. 4.1 Examined pipes and weld details in comparative study

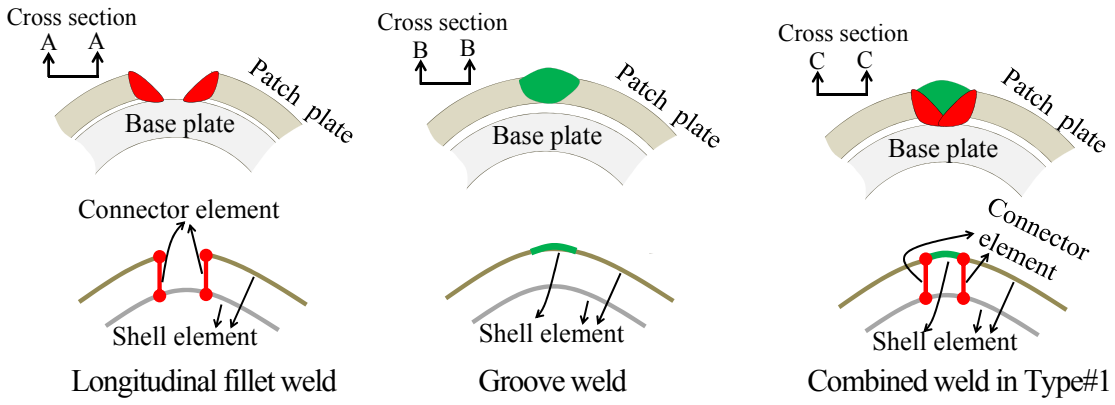

(b) Weld detail and modeling

Fig. 4.1 Examined pipes and weld details in comparative study (continued)

Table 4.2 Fixed parameters in comparative study

Thickness reduction Δt (mm)	6
Thickness of patch plates t_p (mm)	6
Length of thickness-reduced portion $2l_r$ (mm)	500
Length of over-patch l_{p1} (mm)	50
Slit width l_{slit0} (mm)	50
Slenderness parameter of pipe piles	0.215
Slenderness ratio of pipe piles	16.5
Effective length factor	0.5

The target of all repair designs is to recover the structural performance in terms of stiffness and load-carrying capacity of corrosion-damaged pipe piles to the level of intact ones. Characteristic values of material strength are listed in Table 4.3. Standard values of partial factors for materials, applied load (dead load), and structural analysis are $\gamma_{\sigma y}$=1.00, γ_q=1.00, and γ_a=1.00, respectively[4.5)]. In this study, live load is not considered.

In order to compare four different repair types, a baseline design is used for all four types, where repair designs just meet the minimum requirements of the repair design manual, and the additional redundancy is not introduced in the design. Based on this rule, a total length of longitudinal weld lines is determined so as to be just above the minimum required length, and the

thickness of patch plate is set equal to the thickness reduction in the pipe piles. Therefore, even though their welding patterns are different, the four repair designs from Type #1 to #4 are all baseline designs.

Table 4.3 Characteristic values of material strength (MPa)[4.3)]

	Steel pipe SKK400	Patch plate SM400B	Weld metal (underwater welding on site)
Tension and Compression	235	235	-
Shear	136	136	136×0.7=95.2

Type #1 design uses two patch plates fillet-welded on a pipe pile, and two patch plates are further groove-welded together as shown in Fig. 4.1(a). Longitudinal welds in this type are made not only on the intact pipe portion but also on the thickness-reduced portion. Groove welds overlap two longitudinal weld beads and are modeled as shell elements with a thickness of 6 mm and a yielding stress of 600 MPa as illustrated in Fig. 4.1(b). Type #2 design uses two slits, each with two weld lines, in patch plates, which are fillet-welded to the pipe pile along slits. Two patch plates are groove-welded over the thickness-reduced portion. Type #3 and #4 designs use four and eight slits in patch plates, respectively, resulting in a length of one weld line l_{wL0} being a half and a quarter of Type #2.

It should be noted that in Type #1, the length of longitudinal welds at the thickness-reduced portion is not counted in the design because the quality of longitudinal welds may be not as good as those at the intact portion. However, all longitudinal welds of Type #1 are modeled as the same regardless of the potential difference in quality depending on pipe pile conditions. Therefore, Type #1 has longer longitudinal welds than Type #2 due to the extra length of $2l_r$ at the thickness-reduced portion. This treatment in the analysis would result in an upper bound condition of Type #1 repair design.

4.3 FE ANALYSIS ON REPAIR DESIGNS

4.3.1 FE Models

For all the repair types, underwater fillet welds are modeled by the proposed weld model using connector elements in the FE analysis program ABAQUS[4.6)], using a weld throat size a=4.2 mm, representing a target weld leg length of 6 mm, which is one of the most commonly used leg lengths in the underwater repair work. Moreover, to examine the effectiveness of transverse welds in the patch plate repair design, another set of four repair types without transverse welds are also modeled since transverse welds are not included in the weld strength calculation in the current design practice.

In this comparative study, initial stresses due to dead load are not considered in all analytical cases since the main focus of the comparative study is a relative comparison of repaired performance between different baseline repair designs. In the actual conditions, steel pipe piles are part of a structure, and when they corrode, stresses in corroded pipe piles due to dead load may increase or decrease depending on the rest of structure. It is usually difficult to determine the working initial stresses in corroded pipe piles to be repaired. However, if these initial stresses can be estimated, it is possible to design the repair as will be discussed in the next chapter.

Residual stresses in steel due to welding and geometrical imperfections are not considered in the FE model. Because in this study, the structural performance of the damaged pipe piles and the repaired ones are mainly controlled by the damaged region in the base steel, where no welding work is applied and a uniform thickness reduction of 6 mm is considerable large compared with the initial geometrical imperfection such as out-of-straightness of pipe piles.

Therefore, 1/8 of FE model is constructed considering geometrical and loading symmetry. Symmetrical boundary constraints are applied to the model and contact surfaces between base and patch plates are introduced to the model.

Since there are 24 analytical cases (= 6 pipe types x 4 repair designs) with transverse welds and another 24 cases without transverse welds, in total, forty-eight cases of repaired pipe piles are applied with a compressive loading in the FE analysis.

4.3.2 Results and Discussions

The results form FE analysis on pipe piles with different repair designs are summarized and discussed in the following:

(1) Global responses of different repair types

All repaired pipe piles show similar relationships between applied load and pipe shortening under compression. Therefore, global responses of Pipe 4 are plotted in Fig. 4.2 to represent typical results. Applied load P and pipe shortening δ of a total pipe length are normalized by the theoretical yielding load of the intact pipe P_{y0} and the corresponding theoretical yield shortening δ_{y0}, respectively. They are calculated based on yielding stress of steel from tensile coupon test and are listed in Table 4.1. It can be seen that all repaired types have higher stiffness and larger load-carrying capacity than the unrepaired pipe pile. However, the target of a repair design which is to recover structural performance back to its intact level is not reached by any repair type except the overall stiffness after repair. Another finding is that there appears no significant difference in terms of load-carrying capacity between repaired types with and without transverse welds, and all repair types have P_{max}/P_{y0} ratios ranging approximately from 0.8 to 0.9.

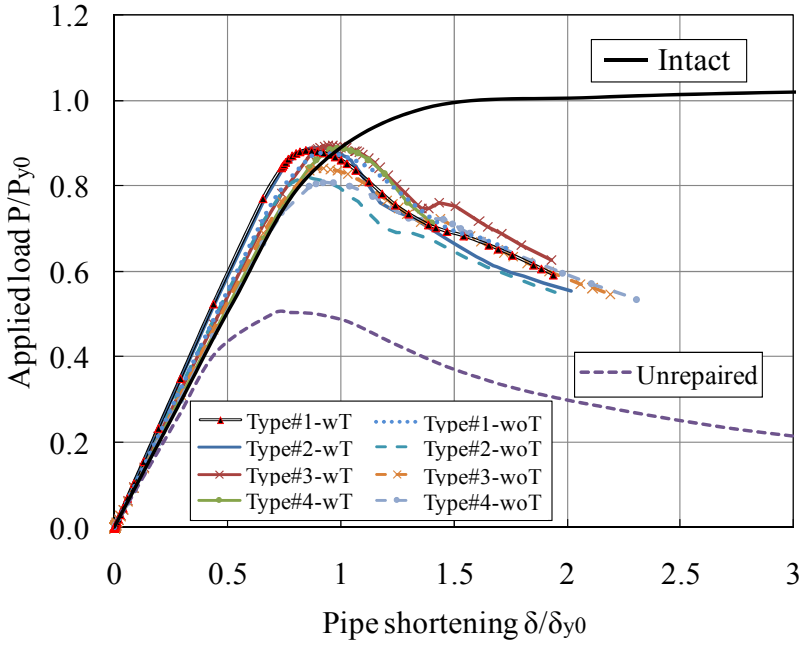

Fig. 4.2 Global responses of Pipe 4 with different conditions

(2) Stiffness of the thickness-reduced portion after repair

This section compares the stiffness of the thickness-reduced portion with a length of $2l_r$ after repair, referred to as K_r, in lieu of overall stiffness for a total pipe length l_0. The ratio between K_r and the stiffness of the intact pipe pile with a length of $2l_r$, K_{r0}, is defined as stiffness recovery, indicating how much stiffness of the thickness-reduced portion is recovered after repair. The definition of K_{r0} and K_r is illustrated in Fig. 4.3. K_{r0}, as shown in Table 4.1, is calculated according to basic structural mechanics. K_r is calculated as a ratio between a total applied load on the repair piles and the shortening displacement of the thickness-reduced base steel. The total load level to calculate K_r is selected to be $0.5P_{max}$, at which all steels are in the elastic phase.

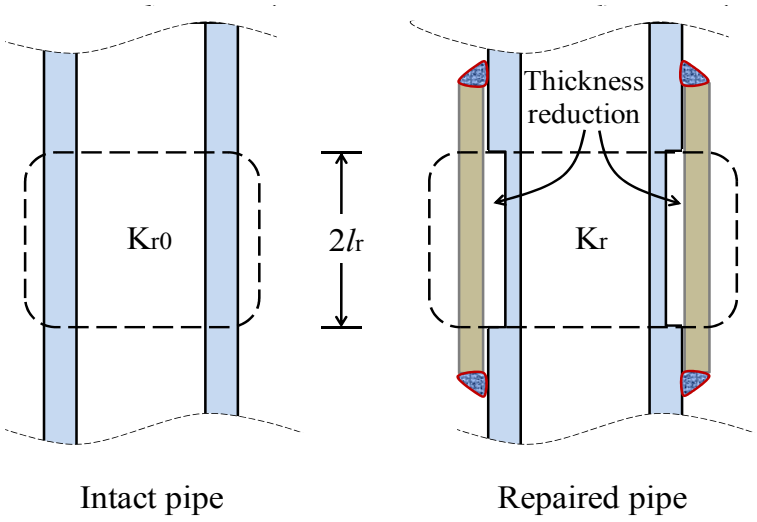

Fig. 4.3 Illustration of K_{r0} and K_r

Stiffness recoveries of all analytical cases are summarized in Fig. 4.4. The discussion on the results is firstly focused on repaired types with transverse welds. In general, all these baseline repair designs fail to fully recover the stiffness of the thickness-reduced portion. The recovery rate ranges approximately from 0.85 to 0.95 among all examined cases. Comparing four repair types within one pipe type, it is found that stiffness recovery rate increases with the number of slits in patch plates. This increase is found to be more significant on pipes with a larger D/t_b ratio. For example, Pipe 6 with a D/t_b ratio of 58.3 has a maximum difference of 8.1% between Type #2 and #4 repairs in stiffness recovery rate compared with other pipes with smaller D/t_b ratios.

By comparing the cases with and without transverse welds, it is interesting to note that although stiffness recovery rate is decreased from the corresponding cases with transverse welds, the extent of decrease is within 15% for all cases and within 10% for the most cases. Moreover, it is found that Type #2 has a largest decrease among four repair types, and that Type #1 shows a little decrease when D/t_b is small as in the cases of Pipes 1 and 2 with D/t_b ratios of 21.4 and 25.0, respectively.

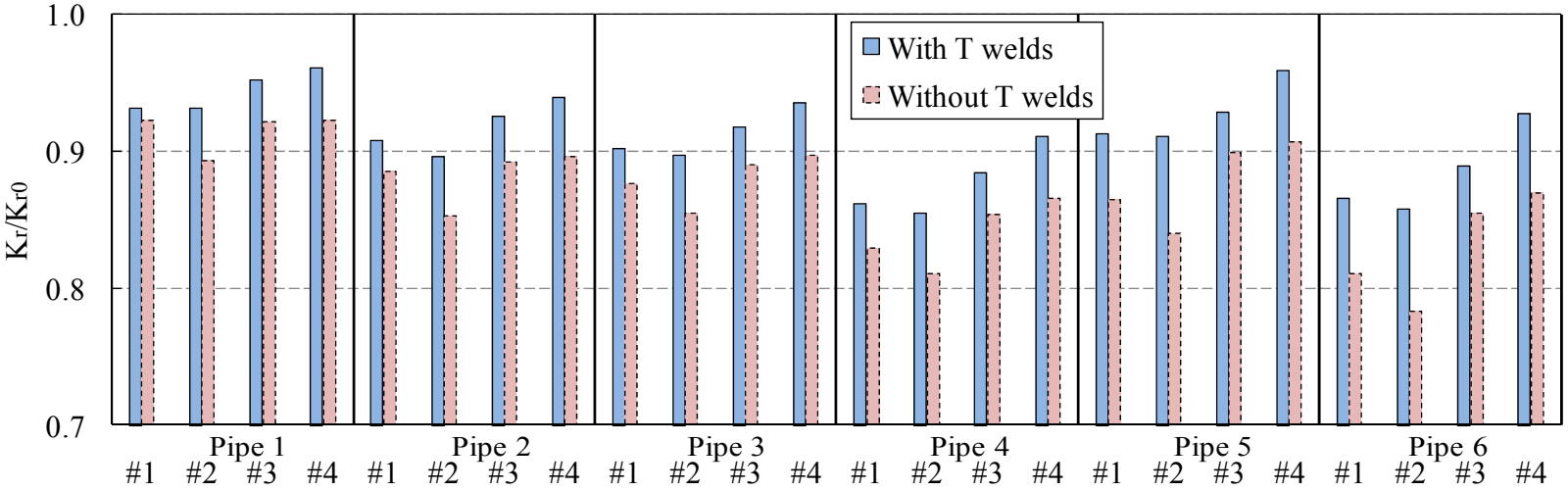

Fig. 4.4 Stiffness of different repair types

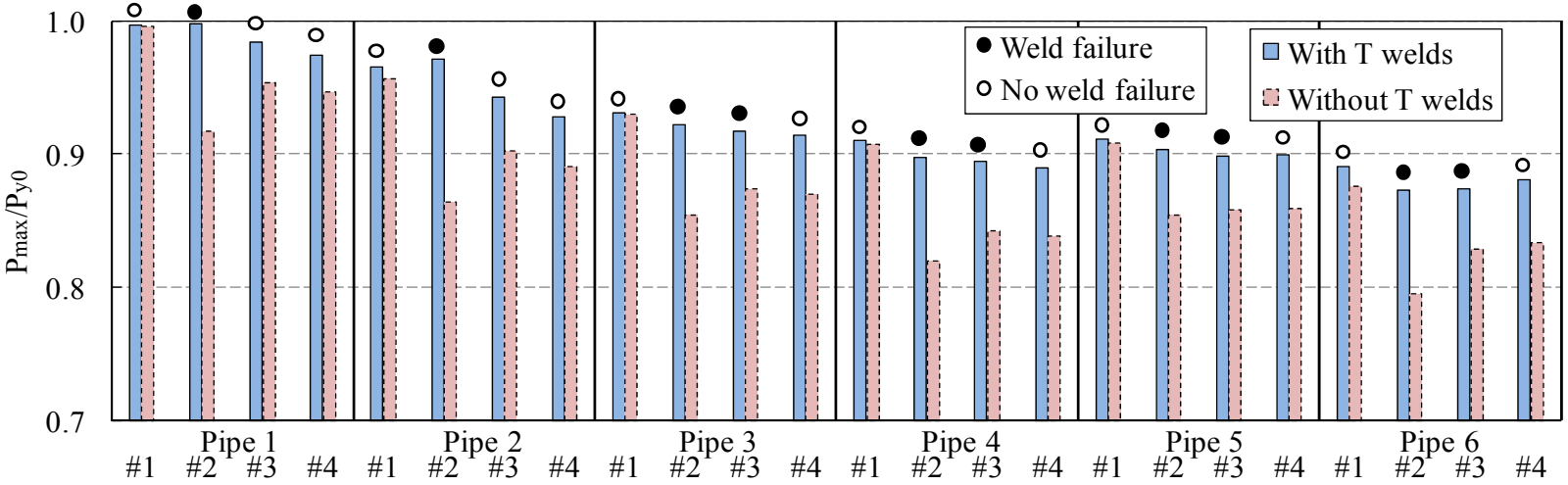

Fig. 4.5 Load-carrying capacity of different repair types

(3) Load-carrying capacity of repaired pipe piles

Load-carrying capacities of repaired pipe piles are summarized in Fig. 4.5. There is a general trend that the recovery rate of load-carrying capacity, represented as P_{max}/P_{y0}, decreases with the increase of D/t_b ratio. For Pipe 1 with D/t_b=21.4, P_{max}/P_{y0} ratios are close to 1.0, while for Pipe 6 with D/t_b=58.3, P_{max}/P_{y0} ratios are about 0.87 for four repaired types. By comparing different repair types within one pipe, it is found that for pipes with smaller diameters, i.e., Pipes 1 and 2, the recovery rate of load-carrying capacity decreases with the number of slits.

This dependency of load-carrying capacity on a number of slits can be explained by the loss of cross-sectional area of patch plates in each repaired type. The more slits are made in patch plates, the more cross-sectional area of patch plates would be reduced, which causes patch plates at the root of patch strips to have higher stress and eventually to yield as shown in Fig. 4.6, resulting in a lower buckling load of repaired pipe piles. This difference is more significant for the pipes with smaller diameters where a relative loss of cross-sectional area is larger than the pipes with larger diameters for the same number of slits.

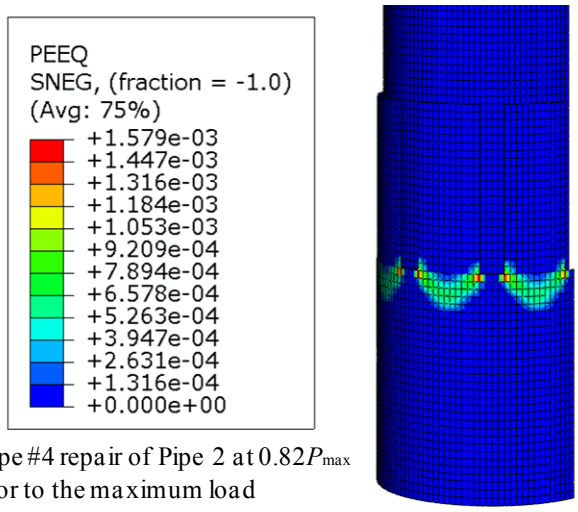

Fig. 4.6 Equivalent plastic strain of Pipe 2 Type #2 repair at 0.82P_{max} showing yielding of patch plate at the root of patch strips

It is of importance to note that load-carrying capacities of repaired pipe piles are below the theoretical yielding loads of their corresponding intact pipe piles, and this phenomenon is more significant in pipe piles with larger D/t_b ratios as an overall trend shown in Fig. 4.5.

In addition, more slits require more weld lines in the repair work, which would generate more residual stresses in welded steels and result in a lower load-carrying capacity of the repaired pipe. Although residual stresses are not considered in the FE model in this study, more slits in the repair design will result in a lower load-carrying capacity when there exist residual stresses caused by welding.

(4) Failure modes of repaired pipe piles

Analytical cases that showed weld failure are also indicated in Fig. 4.5. Weld failure is observed at the re-entrant corners of slits and is similar to that shown in Fig. 3.10 of the model validation pipe presented in Chapter 3. There is no weld failure found in Type #1 repair, and this is considered to be reasonable because the continuous longitudinal weld beads at the thickness-reduced portion would reduce the relative displacement between base steels and patch plates, resulting in a reduction of shear stresses in fillet welds. For other repair types, it is found that the repair type with more slits is beneficial to prevent fillet welds from failing, and that the larger a D/t_b ratio of pipe pile is, the larger number of patch slits is required to prevent weld failure. As indicated in Fig. 4.5, in order to have intact fillet welds, Pipe 1 and 2 only need four slits, while other pipes need eight slits.

Failure modes of repaired pipes are examined at $0.9P_{max}$ in the post-peak stage. Contour plots of equivalent plastic strains from Pipe 4 are selected here as a representative as shown in Fig. 4.7. It suggests that for all repair types, the base pipe at the thickness-reduced portion buckles first, as shown in Fig. 4.7(a), and buckling at patch plates follows in different ways as shown in Fig. 4.7(b). Patch plates at the mid-height of plates buckle in Type #1 and #2 repairs, while patch plates buckle near the inner transverse welds in Type #3 and #4 repairs, when the reduction of cross-sectional areas of patch plates is large.

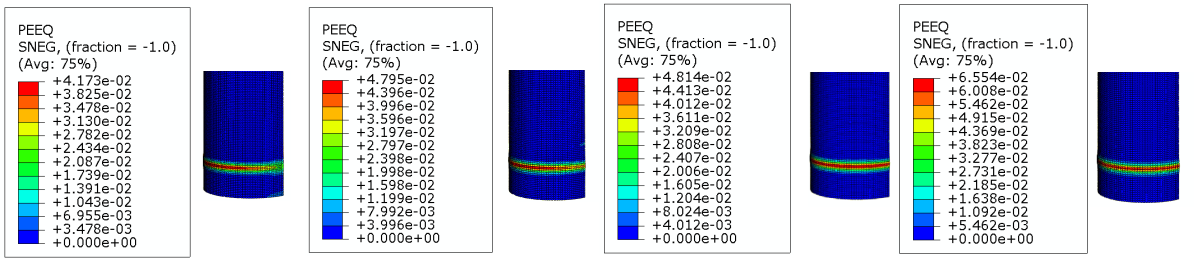

Type #1 Type #2 Type #3 Type #4

(a) Base pipe piles (total length is not fully depicted)

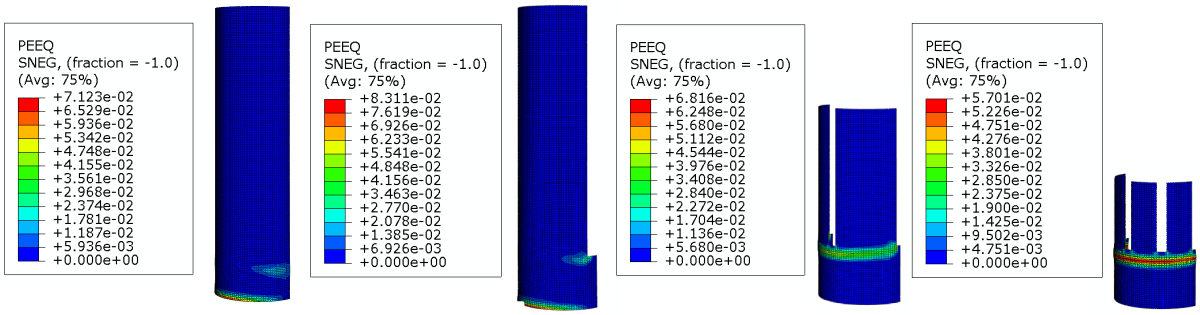

Type #1 Type #2 Type #3 Type #4

(b) Patch plates

Fig. 4.7 Failure modes of different repair types in Pipe 4
(1/4 of model at post-peak $0.9P_{max}$)

(5) Load-share ratio of patch plates

Load share ratios of patch plates P_{patch}/P_{total}, as summarized in Fig. 4.8, are calculated in an elastic phase when applied loads on the repaired pipe piles equal to $0.5P_{max}$. It is found that an overall trend of Fig. 4.8 is very similar to that of Fig. 4.4. Corresponding to stiffness recovery rate ranging from 0.85 to 0.95, P_{patch}/P_{total} ratio ranges from 0.35 to 0.47, meaning a larger portion of load is carried by the thickness-reduced base pipes rather than patch plates.

Examinations on load share ratios of patch plates in different repair types also suggest that a patch plate with more slits and accordingly shorter weld lines is a favorable welding pattern, which would transfer more loads to the patch plate and result in a larger stiffness recovery.

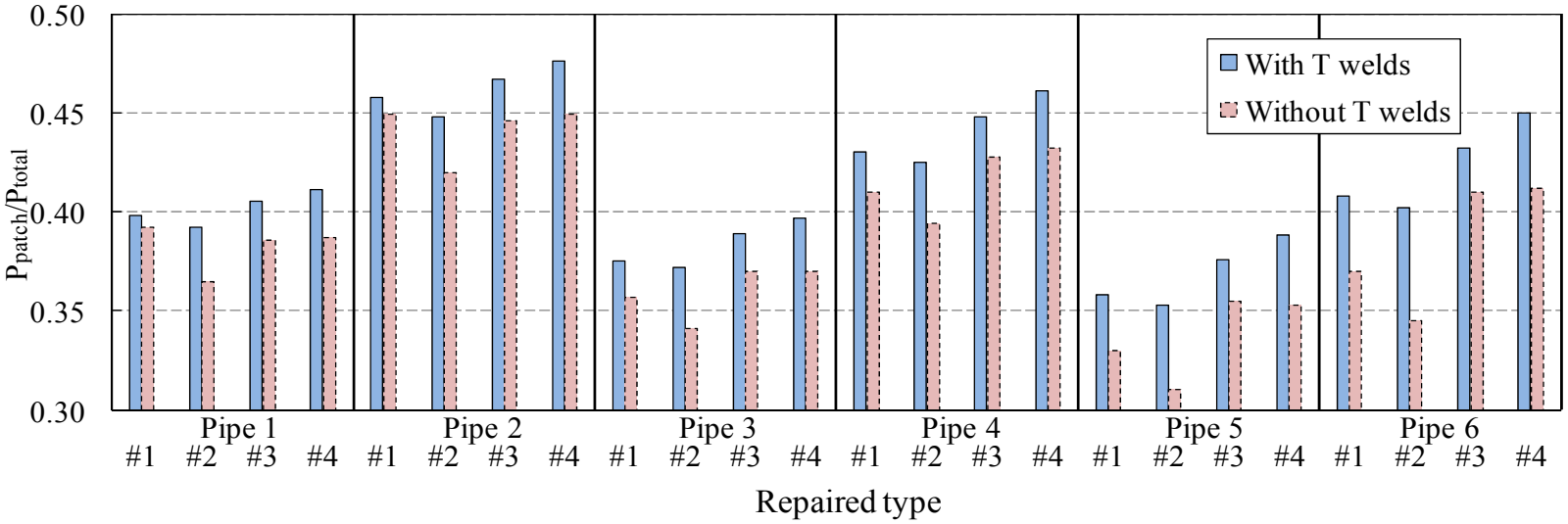

Fig. 4.8 Load share ratio of patch plates in different repair types

(6) Effectiveness of transverse welds

Because the load carried by patch plates, P_{patch}, must be transferred from base pipe piles through longitudinal welds and transverse welds if there are, Eq. (4.1) should be satisfied:

$$P_{patch} = P_{TL} = P_T + P_L \tag{4.1}$$

where, P_{TL} is the total load transferred by transverse and longitudinal welds, P_T is the load transferred by transverse welds, and P_L is the load transferred by longitudinal welds.

Load share ratios of different welds are shown in Table 4.4 for Pipe 4 case. Because different repairs have different P_{max}, the table is calculated at the same applied load at $0.5P_{y0}$ instead of $0.5P_{max}$. The ratios of the total weld length between transverse and longitudinal welds are 0.22 for Type #1 and 0.27 for other three types. It is noted that transverse welds carry more loads than longitudinal welds. The minimum load share ratio of transverse welds is found to be 0.62 in Type #4 repair, and the maximum value is 0.74 in Type #2 repair, implying transverse welds have a more significant role to transfer load in repair types where the number of slits is smaller.

Table 4.4 Load share ratio of welds and patch plates (Pipe 4)

	With transverse welds				Without transverse welds			
	Type #1	Type #2	Type #3	Type #4	Type #1	Type #2	Type #3	Type #4
P_T (MN)	1.05	1.05	0.98	0.94	0	0	0	0
P_L (MN)	0.44	0.37	0.49	0.58	1.35	1.30	1.42	1.44
P_{TL} (MN)	1.50	1.42	1.46	1.51	1.35	1.30	1.42	1.44
P_T / P_{TL}	**0.71**	**0.74**	**0.67**	**0.62**	0	0	0	0
P_L / P_{TL}	**0.29**	**0.26**	**0.33**	**0.38**	1	1	1	1
P_{patch} / P_{total}	0.42	0.43	0.44	0.45	0.40	0.39	0.43	0.43

This finding can explain the observation that Type #2 repair exhibits the largest decrease in stiffness and load share ratio when there is no transverse weld in the repair from the case with

transverse welds. It should also be noted that Type #1 repair that has no slit in patch plates has the second largest load share ratio of transverse welds of 0.71 among four types of repair. Type #1 repair has a smaller load share ratio of transverse welds than Type #2 repair because longitudinal welds in Type #1 are made on the thickness-reduced portion and a total length of longitudinal welds are longer than Type #2.

Although transverse welds carry more loads than longitudinal welds, in the absence of transverse welds, changes in the load share ratio are within 10% for all cases, suggesting that the amount of load carried by patch plates is not affected much by losing transverse welds as long as longitudinal welds remain carrying the load. Therefore, the specification in the current repair design manual is appropriate where transverse welds are not counted when designing a total weld length because the structural behavior of repaired pipe piles would not be influenced significantly whether there are transverse welds or not.

4.4 DESIGN IMPLICATIONS

In previous sections, the compressive behavior of thickness-reduced pipe piles repaired with welded patch plates was examined to understand structural performance of pipe piles repaired according to the current repair design manual. The results show that according to the current design philosophy, a baseline design, which uses the same thickness of patch plate as the reduced thickness in a base pipe and has a load share ratio of patch plates (*LSR*) of $t_p/(t_p+t_r)$, which is 0.5 in the baseline designs presented in this study, fails to recover the stiffness, and for the most cases, the load-carrying capacity of repaired pipe piles to their original status due to an overestimation of *LSR*, which is actually smaller than what is assumed in the base line design.

A comparison of different welding patterns within each pipe piles suggest that the repaired stiffness increases with the number of slits in the patch plates, while the repaired load-carrying capacity decreases with the number of slits. These two observations imply that a patch pattern with many slits is a more favorable type of repair design; however, the total number of slits should be limited to a certain value to avoid the loss of load-carrying capacity of repaired pipe piles. The question then is how to design an efficient repair, and the design procedure will be proposed to achieve an efficient repair in the following.

4.4.1 Load Share Ratio of Patch Plates

(1) Analytical derivation

A load share ratio of patch plates determines the stiffness of the repaired portion. The calculation of a required thickness of patch plates, one of the most important design variables in repair work, is based on a load share ratio of patch plates. The current repair design manual assumes an equal strain in the base pipe and the patch plate in the same cross section of the repaired portion, which results in a load share ratio of patch plates of that assumed when the thickness of patch plates is the same as the residual thickness of the base pipe[4.3)]. However, this is not the case as found in all baseline designs presented in Chapter 4. In fact, the load share ratio of patch plates tends to be smaller than 0.5 in baseline designs.

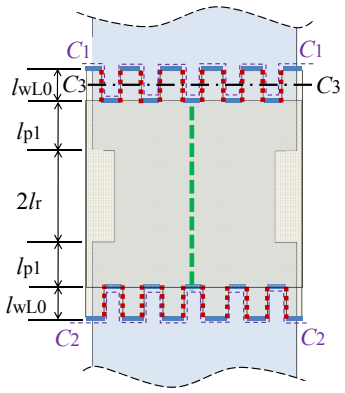

l_r : Half length of the thickness-reduced portion
l_{p1} : Overlap length of patch plates on non-reduced pipe
A_r : Cross-sectional area of the thickness-reduced base steels
A_b : Cross-sectional area of the intact base steels
A_p : Cross-sectional area of patch steels
E : Young's modulus of steel
K_w : Stiffness of all fillet welds
K_{w0T} : Stiffness of transverse fillet welds of per unit length
K_{w0L} : Stiffness of longitudinal fillet welds of per unit length
l_{wT} : Length of transverse fillet welds
l_{wL} : Length of longitudinal fillet welds
l_{wL0} : Length of one weld line of longitudinal fillet welds
$2n$: Number of longitudinal weld lines

(a) Parameters for load share ratio of patch plates

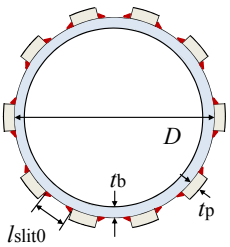

Cross section: C_3-C_3

l_{slit0} : Width of one patch slit
D : Outer diameter of the intact pipe
P_{total} : Applied design load
t_p : Thickness of patch steels
σ_{ypc} : Characteristic value of yielding stress of patch steels
n : Number of slits on patch plates
n_{max} : Maximum number of slits on patch plates

(b) Parameters for the maximum number of slits

Fig. 4.9 Parameters used in the analytical derivation

Therefore, the first task when designing a proper thickness of patch plates is to calculate load share ratio of patch plate accurately. For the repair type where many slits are used as an example showing in Fig. 4.9, this study first assumes that the base pipe and patch plates have an equal amount of shortening deformation between cross sections C_1-C_1 and C_2-C_2, and then the load share ratio of patch plates, *LSR*, can be written as:

$$LSR = \frac{P_{\text{patch}}}{P_{\text{total}}} = \frac{1}{1+\frac{P_{\text{base}}}{P_{\text{patch}}}} = \frac{1}{1+\frac{K_{\text{base}}}{K_{\text{patch}}}} \tag{4.2}$$

where, the compressive stiffness of base steel in the repaired portion, K_{base}, is:

$$K_{\text{base}} = \frac{A_{\text{b}} A_{\text{r}} E_{\text{b}}}{A_{\text{b}} l_{\text{p1}} + A_{\text{r}} l_{\text{r}}} \tag{4.3}$$

and the compressive stiffness provided by patch plates, K_{patch}, is a summation of the compressive stiffness of patch steel, K_{patch}', and the compressive stiffness of fillet welds, K_{W}, which is contributed from both longitudinal fillet welds and transverse fillet welds. Hence:

$$K_{\text{patch}}=(K_{\text{W}}K_{\text{pacth}}')/(K_{\text{W}}+K_{\text{pacth}}') \tag{4.4}$$

$$K_{\text{pacth}}' = \frac{A_{\text{p}} E_{\text{p}}}{l_{\text{p1}} + l_{\text{r}}} \tag{4.5}$$

$$K_{\text{w}} = k_{\text{w0T}} l_{\text{wT}} + k_{\text{w0L}} l_{\text{wL}} \tag{4.6}$$

For a pipe pile under concern, $l_{\text{wT}} = \pi D$ and $l_{\text{wL}} = 2n l_{\text{wL0}}$.

Considering Eqs. (4.5) and (4.6), Eq. (4.4) can be rewritten as:

$$K_{\text{patch}} = \frac{A_{\text{p}} K_{\text{W}}}{A_{\text{p}} + \frac{K_{\text{W}}}{E_{\text{p}}}(l_{\text{p1}} + l_{\text{r}})} \tag{4.7}$$

Dividing Eq. (4.3) by Eq. (4.7), and further assuming the young's modulus of base steel and patch steel are equal, i.e., $E_b=E_p=E$, then:

$$\frac{K_{base}}{K_{patch}} = \frac{A_b A_r}{A_p} \cdot \frac{l_r + l_{p1} + A_p E / K_w}{A_b l_r + A_r l_{p1}} \tag{4.8}$$

Further substituting Eq. (4.8) into Eq. (4.2) obtains the load share ratio of patch plate, *LSR*, considering the stiffness of fillet welds as Eq. (4.9):

$$LSR^{(1)} = \frac{P_{patch}}{P_{total}} = \frac{1}{1 + \frac{A_b A_r}{A_p} \cdot \frac{l_r + l_{p1} + A_p E / K_w}{A_b l_r + A_r l_{p1}}} \tag{4.9}$$

Definitions of variables used in Eq. (4.9) are shown in Fig. 4.9(a).

It is noted that the term A_pE/K_w in Eq. (4.9) is a relative stiffness of patch plates compared to fillet welds, and it represents the effect of weld stiffness on load share ratio of patch plates. According to the current repair design concept, the necessity to consider weld stiffness into structural behavior of welding patch repaired pipe piles is not addressed by thinking that fillet welds are stiff enough to be regarded as rigid connections between base steel and patch steel[4.3), 4.5)]. When K_w approaches to infinite, Eq. (4.9) then retrogresses to Eq. (4.10).

$$LSR^{(2)} = \frac{P_{patch}}{P_{total}} = \frac{1}{1 + \frac{A_b A_r}{A_p} \cdot \frac{l_r + l_{p1}}{A_b l_r + A_r l_{p1}}} \tag{4.10}$$

The results of load share ratio from Eqs. (4.9) and (4.10) are plotted in Fig. 4.10 with those obtained from FE analysis and experiments. There are four experimental results in the figure: KA2C and KW2C are described previously in Chapter 3, and KA4C and KW4C specimens, using four slits on patch plates and a thickness of patch plates of 12 mm, are also selected from Ref. 4.9).

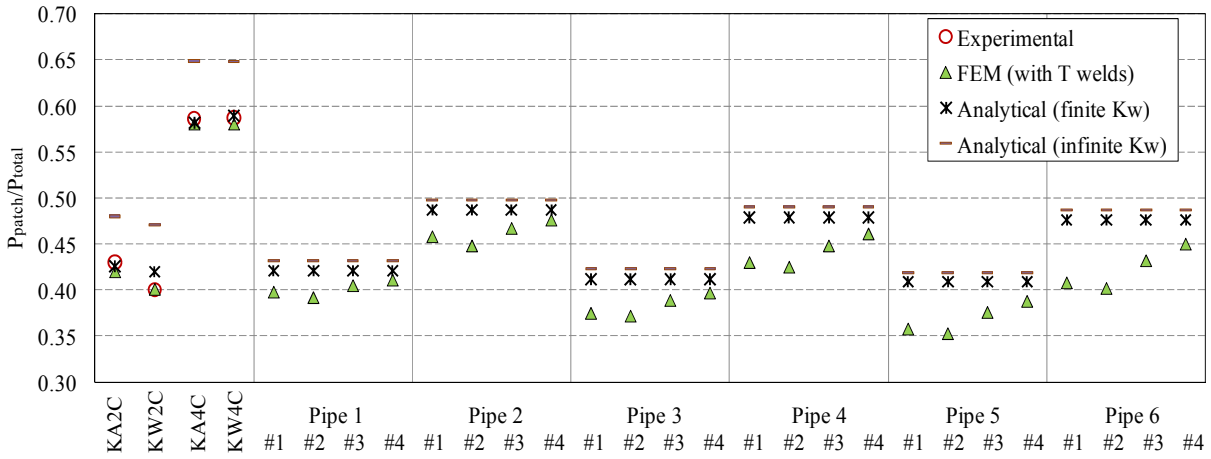

Fig. 4.10 Comparison between load share ratio of patch plates

It can be found that, firstly, FE analysis results as well as analytical results from Eq. (4.9) have good agreement with four experimental results. Moreover, due to the assumption introduced, Eq. (4.9) predicts FE analysis results better when the number of slits is larger as in the case of Type #4 than the repair types with less slits. It is also noted that for all analytical cases considered, there is a negligible difference of about 3% between Eq. (4.9) and Eq. (4.10) where welds are regarded to be infinitely stiff. However, Eq. (4.10) yields a considerable overestimation of about 12% when the assumption of rigid welds is applied to experimental cases.

(2) Error Examination

This finding as shown in Fig. 4.10 raises an important concern, which is that how much error it would bring into the calculation of load share ratio of patch plates when welds are assumed to be rigid. To examine the error, an error factor η is introduced as Eq. (4.11):

$$\eta = \frac{LSR^{(2)} - LSR^{(1)}}{LSR^{(1)}} \times 100\% = \frac{E}{\pi B} \cdot \frac{1}{\omega} \times 100\% \tag{4.11}$$

$$\omega = D\left(\frac{l_r}{A_r} + \frac{l_{p1}}{A_b} + \frac{l_r + l_{p1}}{A_p}\right) \tag{4.12}$$

$$B = K_{w0T} + \frac{l_{wL}}{\pi D} K_{w0L} \tag{4.13}$$

$$l_{wL} = \frac{A_b - A_r}{A_b} \cdot \frac{P_{total}}{\sigma_w a} \tag{4.14}$$

where, ω is structural size factor, B is weld equivalent stiffness, σ_w is the characteristic value of weld strength, and a is weld throat size. As an example, the change of η with ω is plotted in Fig. 4.11 using $P_{total}=P_{y0}$ and a=4.2 mm[4.8]. It is found that when the structural size factor ω is larger than, for example, 20, welds can be treated as rigid without introducing a large error in calculating the load share ratio of patch plates, while there is a rapid increase in the error factor η, which can be larger than 10% when ω is within 10.

To better understand this difference in the calculation, taking, Pipe 1 presented in Chapter 4, as an example, Pipe 1 has a structural size factor ω=27 and a corresponding factor η=3%. When the length of the thickness-reduced portion $2l_r$ changes from 500 mm to 200 mm, and the length of over-patch l_{p1} changes from 50 mm to 10 mm, the structural size factor ω then becomes 10, resulting in η of 7%. Therefore, it is recommended that 20 be a threshold value of ω to choose an appropriate equation for a load share ratio between Eqs. (4.9) and (4.10).

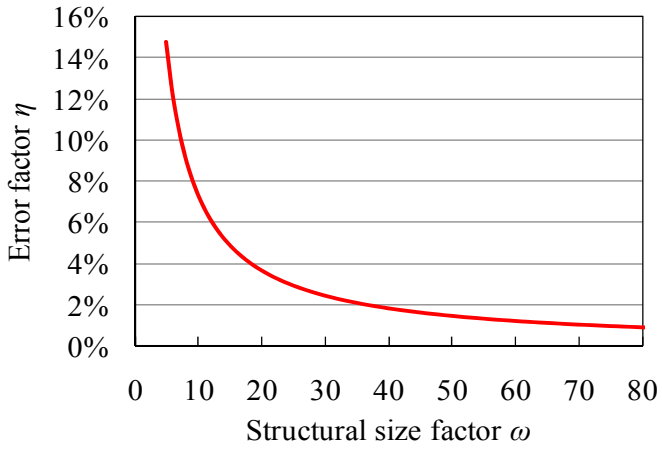

Fig. 4.11 Error on load share ratio by assuming welds as rigid

4.4.2 Minimum Thickness of Patch Plates

It was also found that by attaching patch plates of the same thickness as the thickness reduction of the base pipe cannot fully recover the stiffness of the pipe. Once a load share ratio can be predicted using Eq. (4.9), a proper thickness of patch plates to recover the target stiffness can be determined.

Under an axial loading, a repair to recover its stiffness of the corrosion-damaged portion requires patch plates to carry at least the same load as what the missing thickness once carried in the intact pipe pile. Therefore, the load share ratio of patch plates should satisfy Eq. (4.15):

$$LSR = \frac{P_{\text{patch}}}{P_{\text{total}}} \geq \frac{A_{\text{b}} - A_{\text{r}}}{A_{\text{b}}} \cong \frac{\Delta t}{t_{\text{b}}} \tag{4.15}$$

Considering the minimum diameter of steel pipe piles specified in JIS A5525 is larger than 300 mm, the required thickness of patch plates to recover the stiffness of the damaged pipe piles can be obtained according to a slight conservative calculation by assuming $A_{\text{p}}=\pi D t_{\text{p}}$:

$$t_{\text{p}}' = \frac{1}{\pi D} \cdot \frac{(l_{\text{r}} + l_{\text{p1}}) A_{\text{b}}}{\dfrac{A_{\text{b}} l_{\text{r}} + A_{\text{r}} l_{\text{p1}}}{A_{\text{b}} - A_{\text{r}}} - \dfrac{E}{K_{\text{w}}} \cdot A_{\text{b}}} \tag{4.16}$$

Moreover, as a common strategy used in the design manual, a sacrificial thickness of t_{ps}= 2 mm is added to the calculated minimum thickness of patch plates to protect the patches in the harsh offshore environment[4.3, 4.4]. Finally, the thickness of patch plates used in the repair work, t_{pd}, can be determined as:

$$t_{\text{pd}} = t_{\text{p}}' + t_{\text{ps}} \tag{4.17}$$

4.4.3 Maximum Number of Slits

Although patch plates with a larger number of slits is favorable to transfer loads from base pipe piles to patch plates, the number of slits should not exceed a certain value to avoid an excessive loss of cross-sectional area of patch plates, which would cause steel at the root of patch strips to yield. Hence, the stress in patch steels should satisfy Eq. (4.18):

$$\sigma_{\mathrm{p}} = \frac{P_{\mathrm{patch}}}{A_{\mathrm{strip}}} \le \gamma_{\sigma_{\mathrm{y}}} \sigma_{\mathrm{ypc}} \tag{4.18}$$

where, σ_{p} is the axial stress in patch plate, P_{patch} is the axial load taking by patch plates, A_{strip} is the cross-sectional area of patch plates at the root of patch strips, $\gamma_{\sigma\mathrm{y}}$ is the partial factor for material, and σ_{ypc} is the characteristic value of yielding stress of patch steel[4.5)].

P_{patch} and A_{strip} can be expressed as Eqs. (4.19) and (4.20), respectively:

$$P_{\mathrm{patch}} = P_{\mathrm{total}} LSR \tag{4.19}$$

$$A_{\mathrm{strip}} = t_{\mathrm{p}} \pi (D + t_{\mathrm{p}}) - n t_{\mathrm{p}} l_{\mathrm{slit0}} \tag{4.20}$$

where P_{total} is the total applied load, and load share ratio of patch plates, *LSR*, can be determined by Eq. (4.9) or Eq. (4.10), whichever appropriate. Then the maximum number of slits, n_{max}, can be determined by Eq. (4.21) when a width of one patch slit, l_{slit0}, is given. Definitions of variables in Eq. (4.18) to Eq. (4.21) are shown in Fig. 4.9(b).

$$n_{\mathrm{max}} \le \frac{1}{l_{\mathrm{slit0}}} \cdot \left[\pi (D + t_{\mathrm{p}}) - \frac{P_{\mathrm{total}} LSR}{\gamma_{\sigma_{\mathrm{y}}} \sigma_{\mathrm{ypc}} t_{\mathrm{p}}} \right] \tag{4.21}$$

4.4.4 Design Example

Take the Pipe 4 presented in this Chapter for exapmle. In order to recover the stiffness back to its original state, the load share ratio of patch plates should be 0.5. Selecting a length of over-patch l_{pl}=50 mm and a weld throat a=4.2 mm, the t_{p}' can be calculated by Eq. (4.16) to be 6.6 mm instead of 6 mm used in the baseline design. Summing a sacrifical patch thickness of 2 mm, the design thickness of patch plates is then equal to 9 mm. Setting the total appiled load $P_{\mathrm{total}}=\sigma_{\mathrm{ybc}} A_{\mathrm{b}}$, where σ_{ybc} is the characteristic value of yielding stress of base steel, and A_{b} is the cross-sectional area of the intact base steel. The maxmium number of slits is then calculated to be 12 using Eq. (4.21) when l_{slit0}=50 mm is used. When the patch thickness and the number of slits

are determined, the repair method to recover the stiffness of the thickness reduced pipe pile under compression can be applied.

4.5 CONCLUSIONS

This chapter presented a comprehensive numerical and complementary analytical study on the compressive behavior of thickness-reduced pipe piles repaired with welded patch plates. The current Japanese design manual regarding to welding repair were evaluated. The findings of this chapter are summerized as follow:

(1) A repaired type with many slits in patch plates and short weld lines is a more favorable type for welding repair of pipe piles under compression. However, the number of slits should be limited to avoid yielding of the patch plate.

(2) A baseline design, taking a value of $t_p/(t_p+t_r)$ as a load share ratio of patch plate in the design manual, has a smaller load share ratio of patch plates than that according to the design calculation. Consequently, the baseline design cannot recover the stiffness of pipe piles in repair under compressive load.

(3) The existence of transverse welds does not change structural performance of repaired pipe piles with welded patch plates significantly. Therefore, a repair design procedure for a welding patch plate in the current repair design manual where transverse welds are not counted when designing a total length of fillet weld is appropriate.

(4) A design equation to accurately estimate a load share ratio of patch plates is proposed by considering stiffness of fillet welds. When the structural size factor ω is larger than 20, fillet welds can be regarded as rigid in the calculation of a load share ratio without introducing the significant error.

(5) An equation for the minimum thickness of patch plates required to fully recover stiffness to the intact pipe pile level is proposed. A design equation for the maximum number of slits in patch plates is proposed to avoid yielding of patch plate.

REFERENCES

4.1) Perez-Guerrero, F., and Liu, S., Maintenance and repair welding in the open sea, *Welding Journal*, 84(11), pp. 54-59, 2005.

4.2) Wernicke, R. and Billingham, J., Underwater wet repair welding and strength testing on pipe-patch joints, *Journal of Offshore Mechanics and Arctic Engineering*, ASME, 120(4), pp. 237-242, 1998.

4.3) Coastal Development Institute of Technology, *Port Steel Structure Corrosion-Prevention and Repair Manual (version 2009)*, Coastal Development Institute of Technology, Japan, 2009 (in Japanese).

4.4) Coastal Development Institute of Technology, *Port Steel Structure Corrosion-Prevention and Repair Manual (version 1997)*, Coastal Development Institute of Technology, Japan, 1997 (in Japanese).

4.5) The Japan Port & Harbour Association, *Technical Specifications and Explanations on Port and Harhour Infrastructures*, The Japan Port & Harbour Association, Japan, 2007 (in Japanese).

4.6) Dassault Systèmes Simulia Corp., *ABAQUS/Standard user's manual*, *version 6.8*, 2008.

4.7) Kitane, Y., Itoh, Y., Watanabe, N., and Matsuoka, K., Compressive and flexural tests of thickness-reduced steel pipes repaired with patch plates using underwater wet welding, *Journal of Structural Engineering*, JSCE, 55A, pp. 889-902, 2009 (in Japanese).

4.8) Chen, X., Kitane, Y., and Itoh, Y., Evaluation of repair design on corrosion-damaged steel pipe piles using welded patch plates under compression, *Journal of Structural Engineering*, JSCE, 57A. pp. 756-768, 2011.

CHAPTER 5
REPAIRED PERFORMANCE AND DESIGN PROPOSAL OF PIPE PILES REPAIRED BY PATCH WELDING

5.1 INTRODUCTION

The structural performance of offshore and port structures is deteriorating rapidly from the moment they were built due to severe corrosive environment. Generally, it needs several repair works to extend the structural life to the designed service life. To achieve cost-effective functionality and quality and to enable offshore and port structures to generate maximum direct and indirect income for minimal Whole Life Cost (WLC), Life Cycle Management (LCM) is regarded as an effective management approach[5.1), 5.2)]. In order to implement LCM, structural performance during its life cycle as shown in Fig. 5.1 should be understood beforehand.

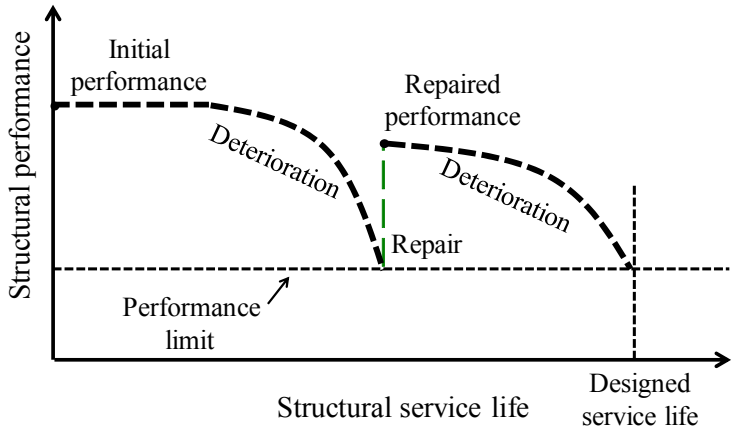

Fig. 5.1 A typical life cycle performance curve of a steel structure

Many researchers dedicate to understanding structural deterioration due to material loss and degradation, and many works have been done for countermeasures against corrosion and better design methods for repair[5.3) ~ 5.8)]. It is necessary to investigate not only how a structure is deteriorating and how it should be repaired, but also how it will continue to work after a certain repair, i.e., how is the repaired performance, to fully grasp the structural performance over a life

span. In addition, although extensive studies have examined the repair effect of corrosion-damaged structural members by various repair methods, most of them were conducted without applying any service loads on the specimens[5.9) ~ 5.12)]. The neglecting of the existing service loads is questionable because the existing service loads in the actual structural members vary and sometimes can be very large depending on their initial design loads, corrosion features, and the accidental load conditions, such as earthquake, tsunami, and vessel collision.

Particularly, in the area of welding repair of offshore structures, this study has investigated mechanical properties of underwater wet fillet welds in patch plate welding repair, evaluated the current design and revised some design calculations in the previous chapters. As a continuous work to supplement and complement the research, this chapter further studies the repaired performance of welding patched steel pipe piles with a special attention paid to the effect of the existing axial loads.

The chapter starts with a set of finite element analysis on patch repaired pipe piles under compression, and then presents an analytical study to clarify the mechanism of load transfer in the repaired pipe piles with preloads. By integrating research results, the design flow and practical solutions to use the design method of welding patch repair are proposed.

5.2 FINITE ELEMENT ANALYSIS

5.2.1 Finite Element Model

A typical type of steel pipe pile with an outer diameter of 500 mm and an intact wall thickness of 12 mm is used in the FE analysis, which is the same pipe pile as the one presented in Chapter 4. There are two reference piles, one is the intact pile, and the other is the thickness-reduced pile, where a uniform thickness reduction of 6 mm is introduced to represent corrosion damages. In this study, the thickness reduction is also referred to as the damages in the base pipe. As found in Chapter 4, a patch type with many slits is more favorable in terms of load transfer. One repaired pipe pile with eight patch slits, i.e., sixteen weld lines, and four preload levels are modeled according to the proposal. Patch plates used in the repair have a design thickness of 9 mm, which is a summation of the minimum required thickness of 7 mm (6.6 mm is the calculated value) and the corrosion sacrificial thickness of 2 mm. Four preload levels are $0.00P_{y0}$, representing a zero-

preload level; $0.12P_{y0}$, representing a small preload level; $0.29P_{y0}$, representing a medium preload level; and $0.47P_{y0}$, representing a large preload level, where P_{y0} is the theoretical yielding load of the intact pipe pile based on the yielding stress of base steel from tensile test. It is noted that $0.47P_{y0}$ is the preload level a little smaller than the one that could yield the damaged base pipe before repair due to a half reduction in the wall thickness. Other structural parameters of pipe piles can be found in Table 5.1.

Table 5.1 Structural parameters of pipe piles

Parameter	Notation	Value	Unit	Parameter	Notation	Value	Unit
Outer diameter	D	500	mm	Tested yielding stress of base steel	σ_{yb}	362	MPa
Intact thickness of base pipe	t_b	12	mm	Cross-sectional area of the intact base steel	A_b	18,397	mm^2
Thickness reduction	Δt	6	mm	Cross-sectional area of the thickness reduced base steel	A_r	9,085	mm^2
Thickness of patch plate	t_p	9 (7)*	mm	Cross-sectional area of patch steel	A_p	14,392 (11,150)*	mm^2
Pipe length	l_0	5,600	mm	Theoretical yielding load of the intact pipe	P_{y0}	6,660	kN
Length of the thickness-reduced portion	$2l_r$	500	mm	Theoretical shortening of the intact pipe at P_{y0}	δ_{y0}	9.99	mm
Length of over-patch	l_{pl}	50	mm	Stiffness of intact pipe with $2l_r$'s length	K_{ro}	7,465	kN/mm
Slit width	l_{slit}	50	mm	Slenderness ratio of the intact pipe pile	λ	16.5	-
Length of each weld line	l_{wl0}	440 (390)*	mm	Slenderness ratio parameter of the intact pipe pile	$\overline{\lambda}$	0.215	-
Number of slits	n	16	-	Radius-thickness parameter of the intact pipe pile	R_t	0.060	-

*Note: The values in "()" are for a repair with a patch thickness of 7 mm.

Because the slenderness ratio of pipe piles is 16.5, which is smaller than a specified threshold value of 18, the global buckling of pipe piles is not a concern[5.13)]. In addition, due to the uniform thickness reduction in the damaged base pipe and the symmetrical patch pattern, it is assumed that the local buckling of the damaged pile and four repaired piles has a symmetrical form about the central axis of pipe piles. As for the intact pipe pile, the geometrical imperfection is introduced as a small uniform thickness reduction of 0.01 mm in the base pipe with the same length as that in the damaged pile, this treatment would guide the intact pipe pile into a symmetrical local buckling form, also known as elephant's foot buckling.

Considering the conditions presented above, a quarter of FE model is constructed and analyzed in the general purpose FE analysis software ABAQUS[5.14] taking advantage of geometrical symmetry as shown in Fig. 5.2. Material properties for base steel, STK400, and patch steel, SM400B, are from tensile coupon tests performed by Kitane et al.[5.15] and are plotted in Fig. 5.3. Fillet welds and groove welds are modeled according to the method presented in Chapter 3 and Chapter 4.

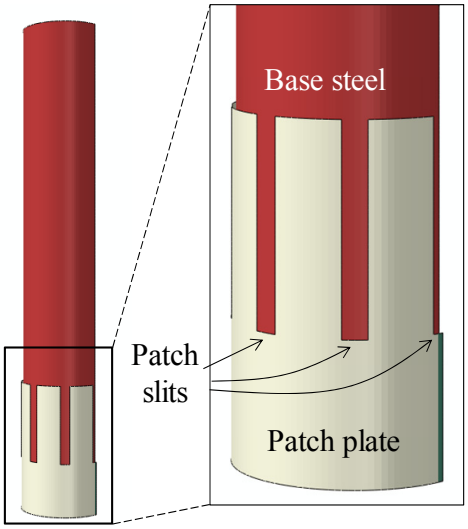

Fig. 5.2 A quarter of FE model

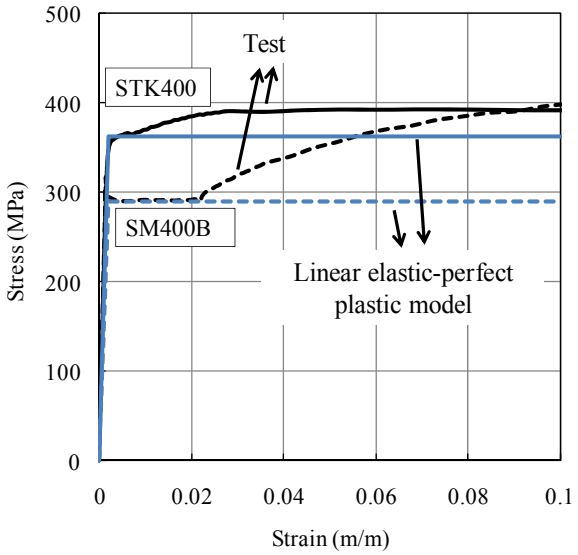

Fig. 5.3 Material constitutive curves

After applying symmetrical boundary conditions to proper model boundaries, two reference piles are applied with a compressive displacement loading to their post buckling phase. Four repaired piles are firstly applied with a designated preload level in compression with patch plates inactivated in the model, which represents the structural state before patch repair. After that, patch plates are activated in the model as a stress-free state, and then a compressive displacement loading is applied up to the post buckling phase of the repaired pipe piles.

5.2.2 Results and Discussions

The compressive responses of six analyzed cases are plotted in Fig. 5.4 in terms of the normalized pipe shortening and applied load. It can be found that the intact pile shows a maximum load carrying-capacity, P_{max}, larger than the design load, P_{y0}, i.e. $P_{max}/P_{y0}>1.0$, and this

is due to material hardening after yielding. The damaged pile shows a great decrease of load carry-capacity as well as the deformation capacity at P_{max}. Furthermore, four repaired piles show similar response curves regardless of different preload levels. The strength of repaired piles is recovered to the design strength, and the deformation capacity at P_{max} is also considerably enhanced, although none of them reaches the intact deformation capacity.

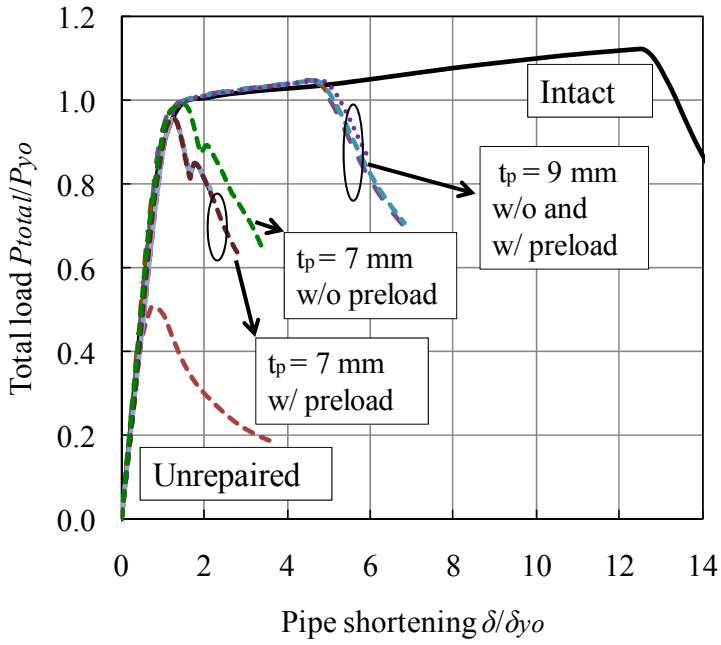

Fig. 5.4 Applied load vs. pipe shortening

The failure mode of four repaired piles is also examined through a contour plot of equivalent plastic strains, noted as PEEQ contour in ABAQUS[5.14], at $0.9P_{max}$ in the post peak phase. All repaired piles show the same failure mode as a local buckling at the intact base pipe adjacent to the repaired region as an example shown in Fig. 5.5(a).

These findings suggest that a patch repair can recover the strength of the damaged pipe pile to the design strength as long as the local buckling of the intact base pipe dominates the failure mode, and once a patch repair design satisfies this condition, it is not necessary to further increase the patch thickness, because the strength of repaired piles is determined by the intact base pipe instead of the patch repaired region.

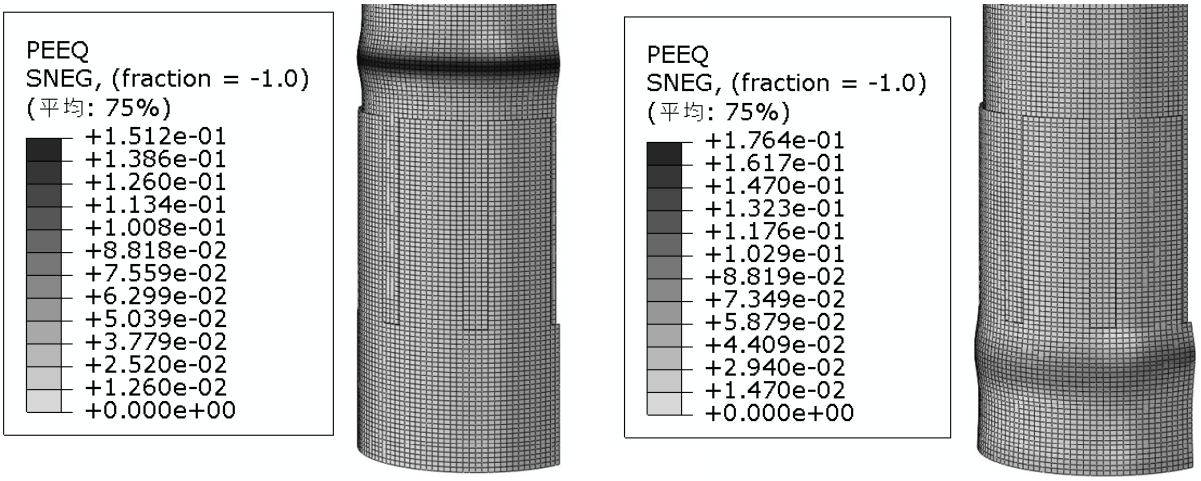

(a) P_{pre}/P_{y0}=0.47, t_p=9 mm (b) P_{pre}/P_{y0}=0.47, t_p=7 mm

Fig. 5.5 PEEQ contour plots at the post peak 0.9P_{max}

Based on the discussions presented so far, it seems that the proposed design method is appropriate and effective to repair a damaged pipe pile, and different preloads appear to have no obvious effect on the repaired performance. However, as previously noted, the patch thickness of 9 mm used in the repaired piles is a design thickness taking into account of the sacrificial thickness of 2 mm, which means that even with a patch thickness of 7 mm, the repaired pipe piles are expected to provide satisfactory structural performance. To check whether this expectation can be met, a new set of FE model is analyzed without introducing the sacrificial thickness into patch plates, i.e., the thickness of patch plates is changed from 9 mm to 7 mm, and correspondingly, the length of each weld line is re-calculated to be 390 mm instead of previous 440 mm. The compressive response of the new model is also plotted in Fig. 5.4 for comparison.

It is found that the repair with a patch thickness of 7 mm can just recover the strength when there is no preload. However, the cases with preloads fail to provide sufficient strength and to enhance the deformation capacity of pipe pile at P_{max}. More importantly, the failure mode of the repair with preloads, as representatively shown in Fig. 5.5(b), is the local buckling at the repaired region rather than the desired one at the intact base pipe, which suggests that the patch thickness of 7 mm is not adequate in this repaired pile. This finding implies that it is necessary to examine the minimum patch thickness required to recover the structural performance with the presence of preloads, which will be discussed in the following sections.

5.3 MECHANISM OF LOAD TRANSFER

5.3.1 Incremental Load Share Ratio

Patch plates are welded to the preloaded pipe piles and join the damaged base pipe to carry the additional loads coming into the pipe pile. The load share ratio is an essential parameter to understand the mechanism of load transfer in the repaired system. Although the load share ratio of patch plates was discussed thoroughly in Chapter 4, it does not include the effects of the existing loads and the loading history of the piles.

Because the material constitutive curve of STK400 steel obtained from the tensile coupon test does not have an obvious yielding plateau, and for both base and patch steel, the test material curves are not perfectly linear within 0.2% strain level. In order for the convenience in comparison between FE analysis results and the following analytical results, the linear elastic-perfect plastic model is used to simplify material curves as shown in Fig. 5.3. The FE analysis performed in Section 5.2 is re-analyzed by just simply substituting the test curves with the model curves of two steels, and the results of load share ratios of the damaged base pipe and patch plates are plotted in Figs. 5.6 and 5.7. In the figures, the load share ratios are calculated based on the incremental loads shared by patch plates and the damaged base pipe.

In the current design manual[5.16], the load share ratio of patch plates can be calculated easily as $t_p/(t_p+t_r)$, which is also equal to the incremental load share ratio of patch plates in the elastic phase. Therefore, it is calculated to be 0.60 and 0.54, when t_p=9 mm, and 7 mm is used respectively. This value is calculated to be 0.58 and 0.52 correspondingly according to Eq. (4.9) considering weld stiffness as proposed in Chapter 4. The load share ratios calculated by these two methods do not consider the effect of preloads. Therefore, they have the constant values at different preload levels along the loading as shown in Figs. 5.6 and 5.7.

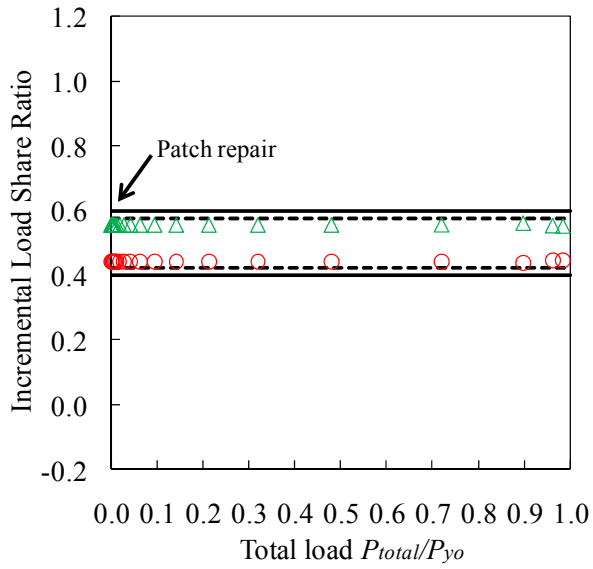

(a) P_{pre}/P_{y0}=0; t_p=9 mm

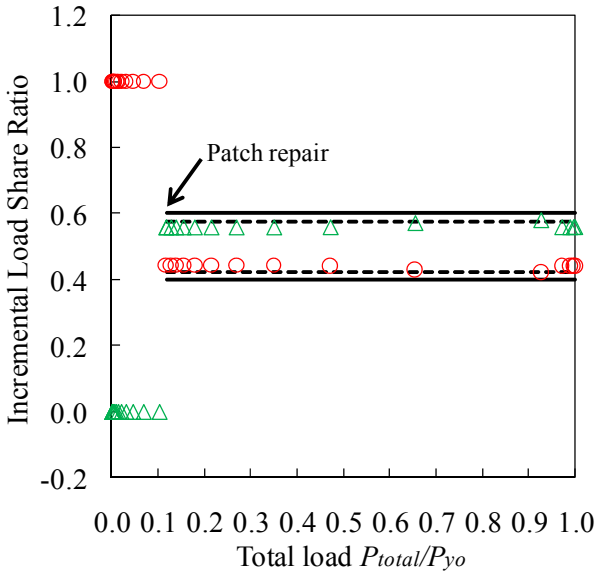

(b) P_{pre}/P_{y0}=0.12; t_p=9 mm

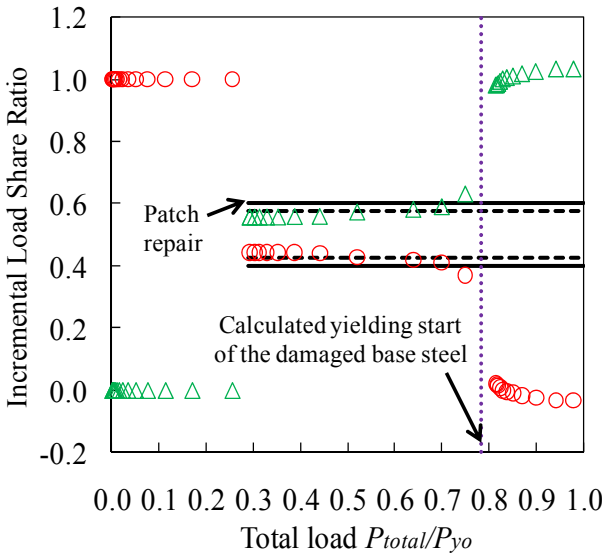

(c) P_{pre}/P_{y0}=0.29; t_p=9 mm

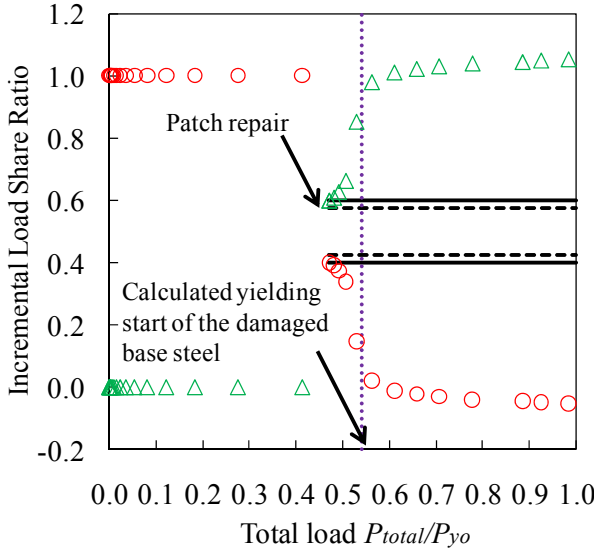

(d) P_{pre}/P_{y0}=0.47; t_p=9 mm

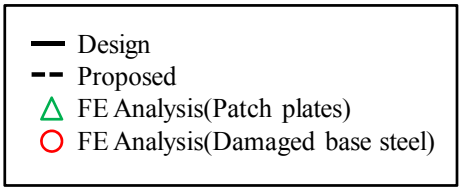

(e) Notation of legend

Fig. 5.6 Load transfer in the repaired piles with t_p=9 mm

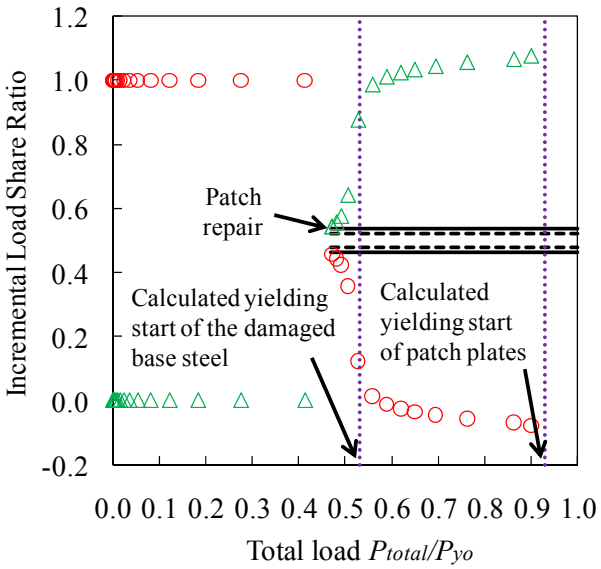

Fig. 5.7 Load transfer in the repaired piles with P_{pre}/P_{y0}=0.47 and t_p=7 mm

It is found in Fig. 5.6(a) that when there is no preload, the load share ratios of patch plates and the damaged base pipe from two calculated methods and FE analysis show good agreement within the total load level of P_{total}/P_{y0}=1. It is noted that the proposed load share ratios do not show much difference from the design values, although they are slightly closer to the results from FE analysis. This is reasonable because as already examined in Chapter 4, when a structural size factor ω is larger than 20, the error by neglecting the effect of weld stiffness in the calculation of load share ratio of patch plates is within 4%, and for repaired pipe piles in the current discussion, the value of ω is 25, resulting in a negligible error in the calculation.

When patch repair is applied to the damaged pipe pile at a small preload level of $0.12P_{y0}$, the load share ratio of the damaged base pipe decreases from 1 to about 0.42 once patch plates start to carry the loads as shown in Fig. 5.6(b). The load share ratios of patch plates and the damaged base pipe after patch repair are the same as those found in the repaired pile without the preload.

However, when a medium preload of $0.29P_{y0}$ is applied, a rapid increase (decrease) of load share ratio of patch plates (the damaged base pipe) is observed in the FE analysis at a total load level P_{total}/P_{y0} around 0.80 as shown in Fig. 5.6(c). By checking plastic strains in the FE model, it is found that the rapid change of load share ratios is caused by the yielding and the immediately following buckling of the damaged base pipe. Thereafter, patch plates alone have to carry all additional loads imposed on the repaired pile. A similar observation can be found in Fig. 5.6(d)

and Fig. 5.7, where the preload level of $0.47P_{y0}$ is close to the yielding load of the damaged base pipe before repair.

For four cases with t_p=9mm as shown in Fig. 5.6, the repaired strength reaches the design strength of the intact pile, i.e., $P_{max}/P_{y0}>1$. However, when t_p=7mm is used, the repaired strength cannot reach the design strength, and the maximum strength after repair is around $0.93P_{y0}$, which is also the total load level that yields patch steels by checking the FE model. This observation suggests that the strength of repaired pile in this repair is determined by the strength of patch plates, and the patch thickness has to be increased in order to further improve the repaired strength of pipe pile.

The aforementioned findings implicate that a cost-effective thickness of patch plates is the one with which patch plates yield just after the intact base pipe yields. If the thickness is thinner than that, the repaired strength cannot be recovered to the design value. On the other hand, if it is thicker, not only the repair cost would be increased due to the thicker patch steel and consequently the longer weld lines, but also the repaired strength cannot be further improved, because the yielding and the following buckling of the intact base pipe would dominate the repaired strength.

5.3.2 Yielding Loads of the Damaged Base Pipe and Patch Plates

In order to find out the cost-effective thickness of patch plates for repair, the yielding loads of the damaged base pipe and patch plates, which are two important load levels during the loading history of repaired piles, are discussed as follows:

Considering a repaired pile under axial compression, the following stress states exist:

$$\sigma_{bo} = \frac{P_{pre} + \Delta P}{A_b} \tag{5.1}$$

$$\sigma_{br} = \frac{P_{pre} + \Delta P_{br}}{A_r} \tag{5.2}$$

$$\sigma_p = \frac{\Delta P_p}{A_p} \tag{5.3}$$

where, σ_{bo}, σ_{br}, and σ_p are axial stresses in the intact base steel, the damaged base steel, and patch plates, respectively. P_{pre} is the preload applied to the damaged pile before patch repair. ΔP, ΔP_{br}, and ΔP_p are the additional loads, the additional loads carried by the damaged base pipe and patch plates, respectively. The relation between them exists:

$$\Delta P = \Delta P_{br} + \Delta P_p \tag{5.4}$$

When the base and patch steels are both in the elastic phase, the following relations exist:

$$\Delta P_{br} = (1 - LSR) \cdot \Delta P \tag{5.5}$$

$$\Delta P_p = LSR \cdot \Delta P \tag{5.6}$$

where, LSR is the load share ratio of patch plates.

With the increase of the additional compressive loads, the damaged base pipe would yield on the condition $\sigma_{br}=\sigma_{yb}$. At this moment, the normalized additional load and the total load applied to the repaired pile can be calculated by Eqs. (5.7) and (5.8), respectively. The subscript "ybr" in the equations means the yielding of the damaged base pipe.

$$\left(\frac{\Delta P}{P_{y0}}\right)_{ybr} = \frac{1}{1 - LSR} \cdot \left[\frac{A_r}{A_b} - \left(\frac{P_{pre}}{P_{y0}}\right)\right] \tag{5.7}$$

$$\left(\frac{P_{total}}{P_{y0}}\right)_{ybr} = \frac{1}{1 - LSR} \cdot \left[\frac{A_r}{A_b} - LSR \cdot \left(\frac{P_{pre}}{P_{y0}}\right)\right] \tag{5.8}$$

Eqs. (5.7) and (5.8) are useful when evaluating the yielding state of an existing patch repair. For the repaired piles presented in this chapter, the calculated yielding loads of the damaged base pipe according to Eq. (5.8) are indicated in Figs. 5.6(c), (d), and Fig. 5.7, and they show good agreement with the FE results. While they are not shown in Figs. 5.6(a) and (b) because the yielding of the damaged base pipe in these two preload levels occur beyond the total load level of $P_{total}/P_{y0}=1$.

Moreover, a repaired design that requires the damaged base pipe does not yield can be guaranteed if the following condition is satisfied:

$$\left(\frac{P_{total}}{P_{y0}}\right)_{ybr} > 1 \tag{5.9}$$

which can be rearranged considering Eq. (5.8) as:

$$LSR > \frac{A_b - A_r}{A_b} \cdot \frac{1}{1-\left(\frac{P_{pre}}{P_{y0}}\right)} \cong \frac{\Delta t}{t_b} \cdot \frac{1}{1-\left(\frac{P_{pre}}{P_{y0}}\right)} \tag{5.10}$$

However, it is noted that the repair design according to Eq. (5.10) is not cost-effective, because the residual strength of the damaged base pipe up to its yielding is not fully used in the repaired system and when the preload level is large, take P_{pre}/P_{y0} close to $(t_b\text{-}\Delta t)/t_b$ for example, the load share ratio of patch plates, *LSR*, should be close to 1 to avoid the forthcoming yielding of the damaged base pipe, which would require very thick patch plates in the repair.

Therefore, it is necessary to consider a further loading after the yielding of the damaged base pipe up to the yielding of patch plates. At the yielding of patch plates, the normalized load carried by patch plates can be calculated by:

$$\left(\frac{P_{patch}}{P_{y0}}\right)_{yp} = LSR \cdot \left[\left(\frac{P_{total}}{P_{y0}}\right)_{ybr} - \left(\frac{P_{pre}}{P_{y0}}\right)\right] + 1 \cdot \left[\left(\frac{P_{total}}{P_{y0}}\right)_{yp} - \left(\frac{P_{total}}{P_{y0}}\right)_{ybr}\right] \tag{5.11}$$

where, $(P_{patch}/P_{y0})_{yp}$ and $(P_{total}/P_{y0})_{yp}$ are the normalized loads in patch plates and the total normalized load in the repaired pile at the yielding of patch plates, respectively. The later can be calculated by:

$$\left(\frac{P_{total}}{P_{y0}}\right)_{yp} = \frac{A_r}{A_b} + \frac{A_p}{A_b} \cdot \frac{\sigma_{yp}}{\sigma_{yb}} \tag{5.12}$$

where, σ_{yp} and σ_{yb} are the yielding stresses of patch steel and base steel, respectively. The subscript "yp" in the equation means the yielding of patch plate. For the repair piles discussed in this chapter, $(P_{total}/P_{y0})_{yp}$ is calculated to be 1.06 and 0.93 for the analyzed cases with t_p=9 mm and 7 mm, respectively. The value of 0.93 is indicated in Fig. 5.7 and shows good agreement with that observed in the FE analysis. While the value of 1.06 is not indicated in Fig. 5.6 because the load level larger than the design strength is beyond the yielding of the intact portion of the pipe.

As the repair concept addressed previously, a patch repair is cost-effective when the yielding of patch plates occurs just after the yielding of the intact base pipe, therefore, the following condition should be satisfied:

$$\left(\frac{P_{total}}{P_{y0}}\right)_{yp} > 1 \tag{5.13}$$

Consequently, the required thickness of patch plates can be calculated as:

$$t_p > \sqrt{\frac{1}{4}D^2 + H} - \frac{1}{2}D \tag{5.14}$$

where,

$$H = (D \cdot \Delta t - \Delta t^2)\frac{\sigma_{yb}}{\sigma_{yp}} \tag{5.15}$$

Considering the minimum diameter of steel pipe piles specified in JIS A5525 is larger than 300 mm, Eq. (5.14) can be further simplified to a slight conservative calculation:

$$t_p > \frac{\sigma_{yb}}{\sigma_{yp}} \cdot \Delta t \tag{5.16}$$

It is of interest to note that unlike the thickness requirement, or the *LSR* requirement, to avoid the yielding of the damaged base pipe as shown in Eq. (5.10), the required thickness shown in Eq. (5.16) is not relevant to preload levels. This finding is considered to be reasonable regarding that the damaged base pipe and the intact base pipe carry the same amount of preload before patch

repair. If the preload level is larger, the damaged base pipe would yield earlier, patch plates would carry all additional loads earlier, and the intact base pipe would also yield earlier, vice versa. Therefore, as long as patch plates are thick enough to remain elastic until the yielding of the intact base pipe, the preload level does not affect the required pile to reach the design strength.

It is also important to note that t_p calculated by Eq. (5.16) satisfies the strength requirement of patch plates for the repaired piles. However, when the yielding stress of patch steel is larger than that of base steel, it does not mean that a patch thickness smaller than Δt can be used in the repair. This is because as an efficient repair, not only the strength should be recovered, but also the stiffness of the repaired portion.

Chapter 4 has already discussed a minimum patch thickness, t_p', to fully recover the initial stiffness of the damaged pipe piles when there is no preload. The calculation method is still applicable to the cases with preloads when the initial stiffness is the concern. Because base and patch steels remain in the elastic phase right after the patch repair is applied, the same derivations can be used to characterize the initial stiffness of the repaired potion. As shown in Figs. 5.6 and 5.7, the load share ratios of patch plates and the damaged base pipe right after patch repair, which determine the initial stiffness of the repaired portion, show good agreement among the results from the proposed calculation and FE analysis.

5.3.3 Two Special Preload Levels

Two special preload levels are discussed in this section, one is a zero-preload level, and the other is the maximum preload level of $P_{pre}/P_{y0}=(t_b-\Delta t)/t_b$, which yields the damaged base pipe before patch repair. For the former load level, it has been discussed thoroughly and a minimum patch thickness t_p' should be used to recover the initial stiffness of the damaged piles. It should be noted that Eq. (5.16) is not applicable to the piles without preload, because once t_p' is used to recover the initial stiffness, the strength can be simultaneously recovered when there is no preload. In this case, the yielding of the damaged base pipe would not occur before the yielding of the intact base pipe, which denies the premise to use Eq. (5.16) that the yielding of the damaged base pipe occurs within the total load level $P_{total}/P_{y0}=1$.

For the preload level which yields the damaged base pipe before patch repair, a patch thickness $t_p=t_b$ should be used to recover the initial stiffness of the repaired portion, because the

damaged base pipe cannot provide any stiffness due to yielding. Meanwhile, the patch thickness should also satisfy Eq. (5.16) to recover the repaired strength.

5.4 DESIGN PROPOSALS FOR WELDING REPAIR

5.4.1 Design Flow

By integrating all the findings presented in Chapter 4 and Chapter 5, the minimum patch thickness can be determined as shown in Table 5.2 to guarantee an efficient repair of pipe piles under axial compression depending on different preloads. The repaired performance of welding patched pipe piles under compression is also noted in the table according to the proposed design. A design flow towards an efficient repair is shown in Fig. 5.8. The corresponding explanations are listed in Table 5.3.

Table 5.2 Minimum patch thickness and the repaired performance

Preload level P_{pre}/P_{y0}	Minimum patch thickness t_{pmin}	Repaired performance		
		Initial stiffness K_r/K_{r0}^*	Ultimate strength P_{max}/P_{y0}	Failure mode
0	t_p'	≥1	≥1	Yielding and buckling in the intact base pipe
>0, <$(t_b-\Delta t)/t_b$	max(t_p' , $\sigma_{yb}/\sigma_{yp}\cdot\Delta t$)	≥1	≥1	
$(t_b-\Delta t)/t_b$	max(t_b , $\sigma_{yb}/\sigma_{yp}\cdot\Delta t$)	≥1	≥1	

*Note: K_r is the initial axial stiffness of the repaired portion under compression; K_{r0} is defined in Table 5.1.

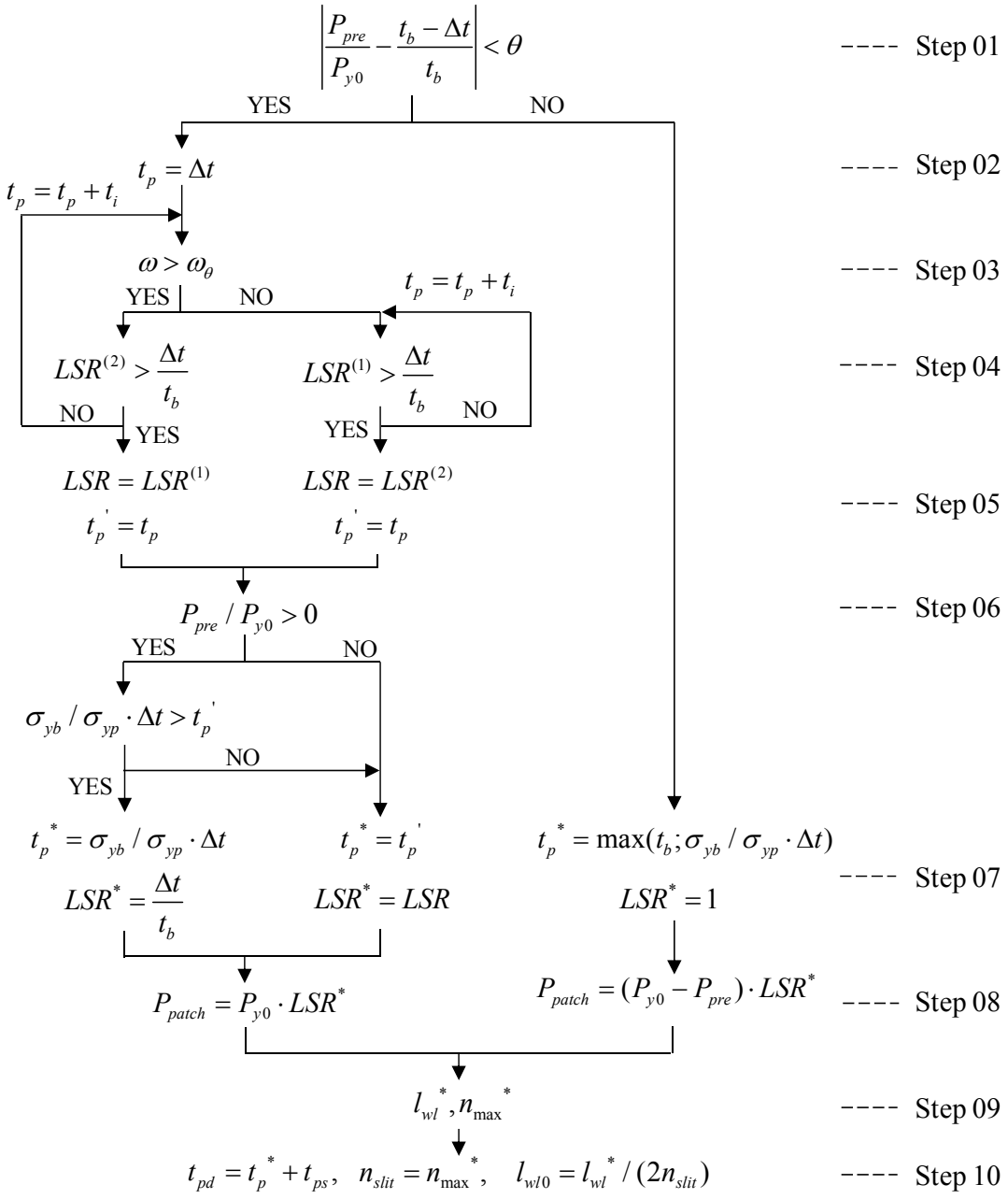

Fig. 5.8 Design flow of welding patch repair for pipe piles under axial compression

Table 5.3 Explanations on the design flow shown in Fig. 5.8

Step	Purpose	Related equations	Note
01	To judge whether the damaged base pipe has yielded before repair.	-	A threshold value of θ set by the user is used.
02	To assign an initial value of Δt to t_p.	-	t_p=Δt is the patch thickness used in the design manual.
03	To judge whether the weld stiffness should be considered in the calculation of *LSR*.	Eq. (4.12).	A threshold value of ω_θ set by the user is used.
04	To judge whether the *LSR* satisfies the stiffness requirement; if not, t_p is increased by a thickness increment t_i.	Eq. (4.9) for $LSR^{(1)}$, Eq. (4.10) for $LSR^{(2)}$.	When calculating $LSR^{(1)}$, the weld length l_{wl} should be known beforehand. A conservative value of zero is assigned to l_{wl} in the calculation.
05	To assign the satisfactory values to *LSR* and t_p'.	-	-
06	To judge whether there is a preload in order to use the appropriate equations for the strength check.	-	This is the start step to check the patch strength.
07	To assign the values of *LSR** and t_p*.	-	The values that satisfy both the stiffness and the strength requirements.
08	To calculate the loads carried by patch plates.	-	-
09	To calculate the corresponding weld length and the maximum number of patch slits.	l_{wl}*=P_{patch}/(σ_w×a), Eq. (4.21) for n_{max}*.	When using Eq. (4.21), $P_{total}LSR$ should be substituted by P_{patch} calculated in Step 08.
10	To calculate the design values for the patch repair.	-	The integral numbers may be necessary for the design values.

5.4.2 Some Practical Issues

In order to pave the way to use the proposed calculations in the actual repair design, there are some issues to be clarified, which will be discussed in the following.

① Corrosion Features

For offshore and port steel structures, the corrosion features, including the average wall thickness, thickness variation, surface roughness, local pits, etc. are too complex to be generalized as mathematical models with common acceptance, although the corroded specimens cut from fields have been delicately measured and tested [5.4), 5.12), 5.17)]. It is essential to capture the corrosion features as precise as possible when predicting the residual strength of steel members, especially when they are in compression, where the local buckling dominates the failure mode of steel members.

However, the demand of precise survey of corrosion features is not necessary when the repaired strength, instead of the residual strength, is in the concern. This is because the failure mode of the repaired pipe piles is expected to occur in the intact base pipe, which is the portion far beyond the corrosion-damaged base pipe. The corrosion features except the minimum and the average wall thickness of the damaged base pipe have little effect on the repaired strength.

Therefore, in the FE analysis and the analytical study presented in this study, an ideal uniform thickness reduction is introduced to represent corrosion damages in pipe piles. This treatment is not only for the connivance in the modeling, but also because it would not generate much difference in the results when evaluating the repaired performance of pipe piles.

② Determination of preloads

Generally, it is difficult or sometimes even impossible to accurately predict the existing loads in a corroded structural member even the design load in the as-built state and its current corrosion features are both known. This is because pipe piles rarely work independently with each other; instead, they are usually assembled as a pile group to support the superstructure as shown in Fig. 1.1. This means that the pile group is actually a structural redundant system and the existing load in one pile is determined not only by the conditions of its own, but also by those of the others.

Fortunately, a constant patch thickness $t_{pmin}=\max(t_p' ; \sigma_{yb}/\sigma_{yp}\cdot\Delta t)$ can be applied to a wide range of preload levels as long as the preload level is not at two special cases as discussed in Section 5.3.3. The zero-preload level is a rare load state existing in the actual structures and the use of

t_{pmin}=max(t_p' ; $\sigma_{yb}/\sigma_{yp}\cdot\Delta t$) would simply give a conservative repair design. The preload level, at which the damaged base pipe has already yielded before repair, exists when the corrosion damage is severe and the loss of steel is large. Although this preload level is difficult to determine quantitatively, the repair design manual provides some thumb rules to judge the severity of corrosion when the residual strength of steel is not expected, implicating the yielding of the damaged steel. For example, it is specified in the manual that when the residual thickness of steel is less than 5 mm, the residual strength of steel is not expected[5.16), 5.18)]; and another use of the thumb rule is stated in the design example in the manual that when pit corrosion is observed in a steel pipe pile all along the circumferential direction, the residual strength is not expected neither[5.18)]. By using thumb rules, this preload level can be estimated and further repair design is then possible.

③ Sacrificial thickness t_{ps}

Without fully understanding of the load transfer mechanism in the repaired piles, the sacrificial thickness t_{ps}, which is 2 mm used in the manual, sometimes provides indispensible stiffness and strength to the repaired piles, and this is actually beyond its intended purpose purely for corrosion sacrifice. In addition, it may be expected by some designers that the use of t_{ps} would give a conservative and safe repair design; however, it is not always the case by studying the load transfer in the repaired piles. For example, a patch thickness of 9 mm is too conservative when there is no preload, where only 7 mm is enough to satisfy the repaired performance; while the thickness of 9 mm is not adequate when the preload level is P_{pre}/P_{y0}=(t_b-Δt)/t_b, where a patch thickness of 12 mm is necessary. Even within two special preload levels, there are also the cases where a patch thickness after taking into account of t_{ps} is not sufficient to provide the satisfactory performance when the yielding stress of base steel is quite larger than that of patch steel.

After clarifying the mechanism of load transfer in the repaired piles, the use of t_{ps} can be reduced or even abandoned, and some other measures, such as FRP covering, tapping, epoxy coating, etc., can be employed to provide corrosion proof for the patch repaired pipe piles. Consequently, the repair cost may be reduced due to thinner patch plates and shorter weld lines without adversely affecting the structural performance.

It is noted that residual stresses due to welding are not modeled in the FE analysis, neither considered in the analytical study. This is because the distribution and the magnitude of residual stresses generated in welding process are difficult to characterize, especially when there are many

weld lines and different preloads in the repaired pipe piles as the cases presented in this study. The effect of residual stresses due to welding on the repaired performance of pipe piles remains as future study.

5.5 CONCLUSIONS

This chapter examined the repaired performance of steel pipe piles using patch welding considering the effect of the existing axial loads. The mechanism of load transfer in the repaired piles is investigated through the FE analysis and the analytical study. The design method using welding patches is proposed by integrating all the findings. The Main conclusions of this chapter can be drawn as:

(1) A minimum patch thickness to recover the design strength of the corrosion-damaged pipe piles to their intact state is proposed. When there is no existing load, t_p' calculated by Eq. (4.16) can be used; otherwise, $\sigma_{yb}/\sigma_{yp}\cdot\Delta t$ should be used, where σ_{yb}, σ_{yp}, and Δt are the yielding stresses of base steel and patch steel, and the thickness reduction in the damaged base steel, respectively.

(2) The load share ratio of patch plates calculated using the method proposed in Eq. (4.9) is proved to be accurate when base steel and patch steel are in the elastic phase.

(3) The minimum patch thickness to fully recover both the initial stiffness and the design strength of the damaged pipe piles under compression is proposed in Table 5.2. The failure mode of the repaired pipe piles that the yielding occurs in the intact base pipe is highlighted.

(4) The design redundancy of the sacrificial patch thickness, which is 2 mm in the current repair design, is clarified. The possibility to reduce the patch thickness without adversely affecting the repaired performance is pointed out.

REFERENCES

5.1) PIANC WG103, *Life cycle management of port structures-recommended practice for implementation*, International Navigation Association, PIANC report 103, pp. 1-56, 2008.

5.2) Kazuaki, Z., Corrosion and life cycle management of port structures, *Corrosion Science*, 47, pp. 2353-2360, 2005.

5.3) Watanabe, N. and Itoh, Y., Evaluation of surface roughness of a corroded steel angle exposed in oceanic environment for 19.5 years, *Journal of Structural Engineering*, JSCE, 54A, pp. 492-503, 2008.

5.4) Yamasawa, T., Nogami, K., Itoh, Y., Watanabe, E., Sugiura, K., Fujii, K., and Nagata, K., Corrosion shapes of steel angle member under oceanic exposure during 19.5 years, *Doboku Gakkai Ronbunshuu A*, JSCE, 64(1), pp. 27-37, 2008 (in Japanese).

5.5) Itoh, Y., Tsubouchi, S., and Kim, I. T., Corrosion deterioration characteristics of various repainted steels considering accelerated exposure test results, *Doboku Gakkai Ronbunshuu A*, JSCE, 64(3), pp. 556-570, 2008 (in Japanese).

5.6) Itoh, Y., Shimizu, Y., and Koyama, A., Durability of steel bridge metallic coating systems for combined cyclic corrosion tests with salt water spray and acid rain spray, *Doboku Gakkai Ronbunshuu A*, JSCE, 63(4), pp. 795-810, 2007 (in Japanese).

5.7) Kainuma, S., Hosomi, N., Goto, A., and Itoh, Y., Fundamental study on evaluation for time-dependent corrosion behavior of long steel members in marine environment, *Doboku Gakkai Ronbunshuu A*, JSCE, 65(2), pp. 440-453, 2009 (in Japanese).

5.8) Sugiura, K., Tamura, I., Watanabe, E., Itoh, Y., Fujii, K., Nogami, K., and Nagata, K., Simplified evaluation of compressive strength of corroded steel plates, *Doboku Gakkai Ronbunshuu A*, JSCE, 63(1), pp. 43-55, 2007 (in Japanese).

5.9) Fujii, K., Nakamura, H., Kondo, T., Hashimoto, K., Okimoto, H., and Nakamura, T., Experiments on bending buckling strength of corroded cylindrical shells, *Journal of Structural Engineering*, JSCE, 53A, pp. 784-793, 2007 (in Japanese).

5.10) Yamasawa, T., Nogami, K., Sonobe, Y., and Katakura, K., Experimental study of steel column member on severe corroding environment, *Journal of Structural Engineering*, JSCE, 55A, pp. 52-60, 2009 (in Japanese).

5.11) Nara, S., Inoue, N., Matsunaga, K., and Takeuchi, S., Evaluation of ultimate compressive strength of

corroded stiffened steel plates, *Journal of Structural Engineering*, JSCE, 55A, pp. 61-67, 2009 (in Japanese).

5.12) Morishita, T., Fujii, K., Morita, K., Horii, H., and Nakamura, H., On rehabilitation of corroded steel plates by adhesive and steel cover plates, *Journal of Structural Engineering*, JSCE, 57A, pp. 747-755, 2011 (in Japanese).

5.13) The Japan Port & Harbour Association, *Technical Specifications and Explanations on Port and Harbor Infrastructures*, The Japan Port & Harbour Association, Japan, 2007 (in Japanese).

5.14) Dassault Systèmes Simulia Corp., *ABAQUS/Standard user's manual*, *version 6.8*, 2008.

5.15) Kitane, Y., Itoh, Y., Watanabe, N., and Matsuoka, K., Compressive and flexural tests of thickness-reduced steel pipes repaired with patch plates using underwater wet welding, *Journal of Structural Engineering*, JSCE, 55A, pp. 889-902, 2009 (in Japanese).

5.16) Coastal Development Institute of Technology, *Port steel structure corrosion-prevention and repair manual (version 2009)*, Coastal Development Institute of Technology, Japan, 2009 (in Japanese).

5.17) Appuhamy, J.M.R.S., Kaita, T., and Fujii, K., Prediction of residual strength of corroded tensile steel plates, *International Journal of Steel Structures*, 11(1), pp. 65-79, 2011.

5.18) Coastal Development Institute of Technology, *Port steel structure corrosion-prevention and repair manual (version 1997)*, Coastal Development Institute of Technology, Japan, 1997 (in Japanese).

CHAPTER 6

EXPERIMENTAL STUDY ON CFRP-BONDED STEEL PLATES USING UNDERWATER EPOXY

6.1 INTRODUCTION

Previous chapters discussed a conventional repair method using steel patch plates by welding. To strengthen and repair structural components, CFRP composites have attracted a great deal of attention during the last two decades due to their favorable properties in terms of high strength, high stiffness, light weight, ease of handling, and superior corrosion resistance[6.1)]. Applications of CFRP to concrete structures have been reported extensively. More recently, the studies on structural performance of CFRP-bonded steel were conducted by different researchers[6.2) ~ 6.6)]. In the most studies, it is concluded that CFRP-bonded structural members exhibit a sound repair effect to enhance stiffness and strength. However, there are some cases where the effect of repair is not obvious when CFRP composites are applied to certain conditions with high humidity or in the wet environment, which can lead to degradation of its stiffness and strength[6.7) ~ 6.11)].

To repair corrosion-damaged offshore or port steel structures, as an alternative to the conventional patch welding repair and concrete jacketing repair, CFRP repair in underwater, due to the availability of epoxy adhesives that can cure in water, has competitive advantages over the conventional methods regarding to working time and handling space. However, the lack of a code for designing CFRP-bonded steel structures impedes the usage of this technique in repairing offshore structures, since the mechanical behavior of CFRP-epoxy-steel system bonded underwater has not been understood yet.

This chapter serves as an original investigation and presents an experimental study on the mechanical behavior of CFRP strand sheet-bonded steel plates under uniaxial tension and compression. Special attention is paid to the curing effect of epoxy adhesive used in the underwater through four sets of material tensile coupon tests. The repair effects are discussed in terms of stress and strain distributions, initial repaired stiffness, yielding strength, as well as

failure mode of the CFRP-bonded steel specimens. In addition, how material properties of underwater epoxy affect their repair performance is further highlighted in this study.

6.2 EXPERIMENTAL PROGRAM

6.2.1 Test Specimens

In the test, two uniaxial loading directions are considered as tension and compression. One and two CFRP layers are used to bond steel plates, which have a uniform thickness reduction of 2 mm on both sides of steel plates of a length of 40 mm. The configuration of CFRP-bonded steel plates is shown in Fig. 6.1. The steel plate used is SM490A with a nominal thickness of 19 mm, which is specified in JIS to have a nominal yielding stress and a nominal tensile strength of 315 MPa and 490 MPa, respectively. The corresponding values are 343 MPa and 498 MPa from the tensile coupon test as shown in Fig. 6.2. All the steel plates are sandblasted for the application of epoxy adhesive.

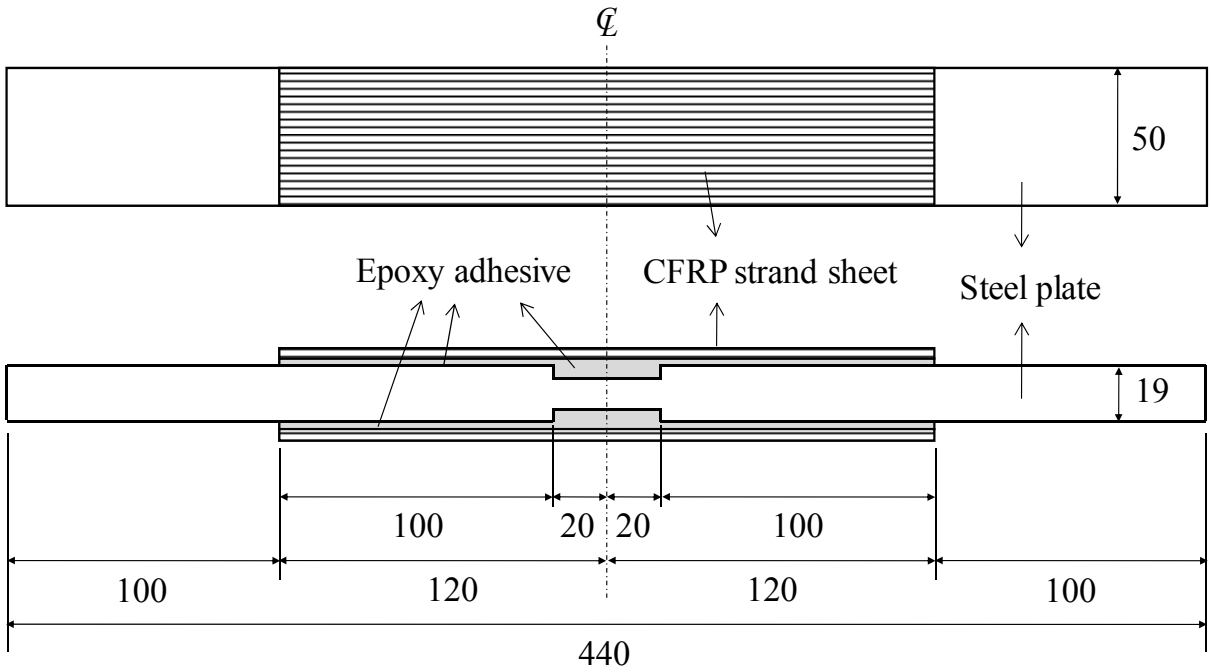

(a) Configuration of CFRP-bonded steel plate (in mm)

Fig. 6.1 CFRP-bonded steel plate used in the test

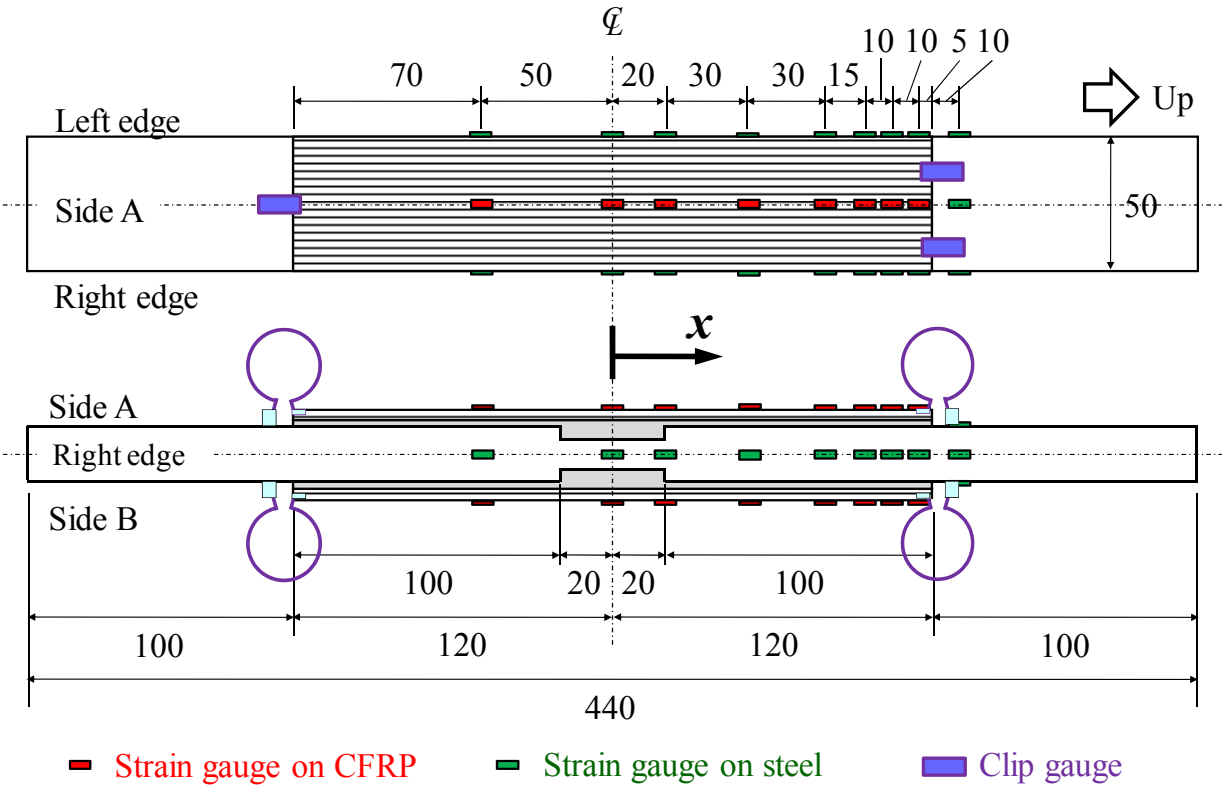

(b) Layout of gauges in the specimen (in mm)

Fig. 6.1 CFRP-bonded steel plate used in the test (continued)

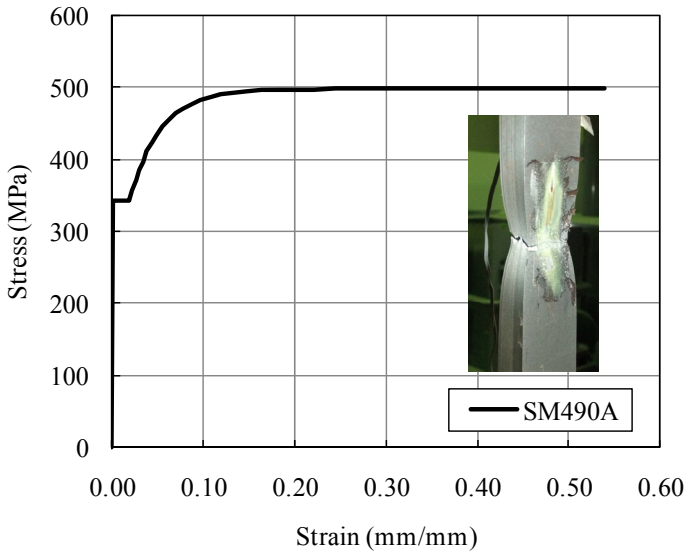

Fig. 6.2 Tensile test curve of SM490A steel

In this study, the specimen designation has a form of "L1T-3", in which, the location of "1" stands for the number of CFRP layers, which can be "0" (no repair), "1" (1 layer), and "2" (2 layers). The location of "T" stands for the loading direction, which can be "T" (tension) and "C" (compression). The location of "3" stands for the specimen number, which can be up to 4 for CFRP-bonded specimens and 2 for control specimens. In total, there are sixteen CFRP strand sheet-bonded steel plates and four control steel plates without repair as shown in Table 6.1.

Table 6.1 Test matrix

Tensile specimen		Compressive specimen	
Specimen notation	No. of CFRP layers	Specimen notation	No. of CFRP layers
L0T-1	0	L0C-1	0
L0T-2	0	L0C-2	0
L1T-1	1	L1C-1	1
L1T-2	1	L1C-2	1
L1T-3	1	L1C-3	1
L1T-4	1	L1C-4	1
L2T-1	2	L2C-1	2
L2T-2	2	L2C-2	2
L2T-3	2	L2C-3	2
L2T-4	2	L2C-4	2

Unlike the conventional CFRP plate, the CFRP strand sheet is used in the tests. The CFRP strand sheet is formed from CFRP strands each with a nominal diameter of d_c=1.5 mm, and the strands are spaced properly and further aligned into a sheet form using transverse threads for the ease of handling and deployment, A photo of CFRP strand sheet is shown in Fig. 6.3(a).

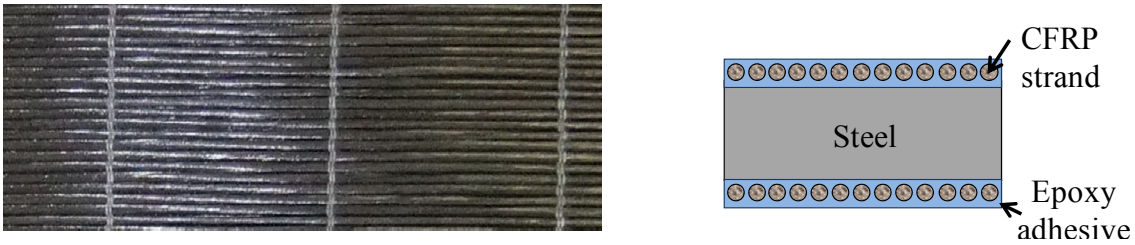

(a) CFRP strand sheet (b) The cross section of the specimen

Fig. 6.3 CFRP strand sheet used in the test

Mechanical properties of the CFRP strand sheet shown in the catalog include the Young's modulus of E_c = 640 GPa, the tensile strength of σ_t = 1,900 MPa, and the design thickness of t_c = 0.429 mm. The fiber volume fraction in the sheet is calculated to be $V_f = t_c/d_c = 0.286$, and that in the each strand is calculated to be $V_f' = 0.465$. Tensile coupon tests are performed on CFRP strand sheets. Each coupon has a nominal width of 15 mm, a nominal thickness of 2 mm, and an average strand number of 8. Test curves of representative coupons are shown in Fig. 6.4.

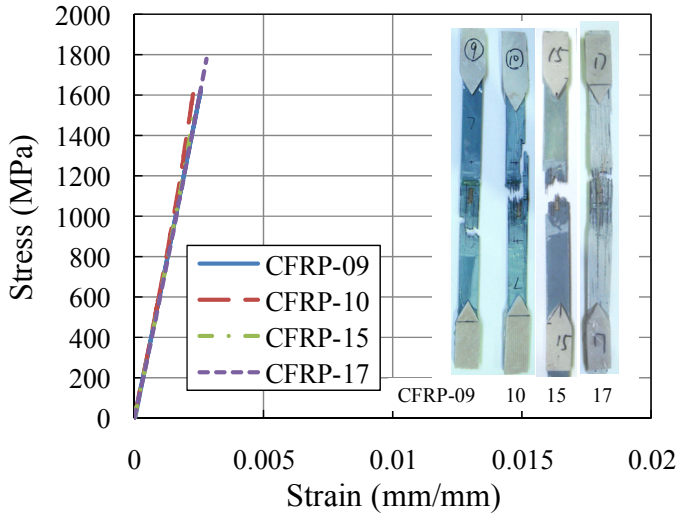

Fig. 6.4 Tensile test curves of CFRP strand sheets

All test curves show linear behavior up to the maximum strength of CFRP coupons. The test value of Young's modulus is 609 GPa, which is close to the catalog value. The test value of tensile strength is 1,645 MPa, which is about 13% smaller than the catalog value, and this is thought to be caused by the fact that all CFRP strands in the coupons do not fracture at the same time and some strands fail before others, resulting in a smaller load-carrying capacity and consequently a smaller maximum strength of CFRP strand sheet coupons.

It is noted that the use of this type of CFRP strand sheets does not require the application of primer, which is usually a necessary procedure after the surface treatment when the conventional CFRP sheet or plate is used. In addition, because the saturation of CFRP strands is not necessary for the sheet, the working procedures are further simplified and repair time is hence greatly shortened.

Fig. 6.5 shows a procedure to produce the CFRP-bonded specimens in this study. Firstly, epoxy adhesive is spread on the steel plate under water, and the epoxy is also applied to the portion where steel thickness is reduced. Secondly, a CFRP strand sheet is applied on the epoxy layer. Then, epoxy is spread over the strand sheet as a surface sealing layer. A target total thickness of CFRP strand sheet and epoxy layers is 2 mm, resulting in a thickness of epoxy layer of 0.25 mm assuming a diameter of a strand is 1.5 mm. The specimens are submerged under water for forty-eight hours for epoxy to cure, and then are taken out from the water and are kept in air at ambient temperature. Water temperature at the time of specimen fabrication was 22°C.

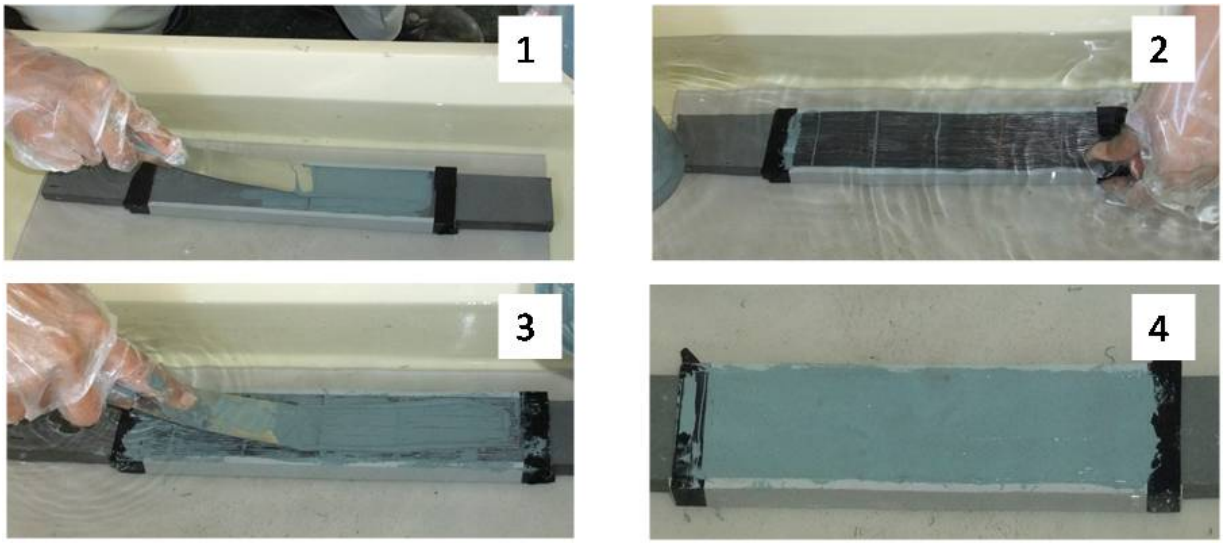

Fig. 6.5 The working procedure to produce the specimen

Epoxy adhesive used in the specimens is currently used in underwater structures for coating to prevent corrosion. The epoxy has high viscosity so that it will not flow down during the spreading underwater. At the same time as specimen fabrication, tensile test coupons of epoxy are also made. After forty-eight hour's underwater curing, epoxy coupons are taken out from the mould and are kept in air at ambient temperature. The CFRP-bonded steel plate specimens are placed in the room temperature for 24 to 60 days before they are tested. The layout of strain gauges and clip gauges is shown in Fig. 6.1(b), and the test setup is shown in Fig. 6.6. It is noted that when two CFRP layers are bonded in the specimens, the strain gauges are attached on the outside layer of CFRP.

Fig. 6.6 Test setup of CFRP-bonded steel plate

6.2.2 Material Properties of Epoxy

Epoxy coupons are divided into four sets and tested following the testing method for tensile properties of plastics specified in JIS K7113, at different curing times of 21, 65, 175, and 250 days, using a 500 kN MTS material testing machine under a displacement control at a rate of 0.015 mm/sec. The nominal width and thickness of epoxy coupons in the test region are 10 mm and 4 mm, respectively. Representative tensile test curves are shown in Fig. 6.7. Results from the different curing times are summarized in Fig. 6.8 to better understand the effect of the curing time on mechanical properties of epoxy. In the figure, E, σ_u, and ε_m are Young's modulus, tensile strength, and the strain at the tensile strength of epoxy coupons, respectively.

It is found that after 21 days of curing, the Young's modulus of epoxy has a mean value of 0.50 GPa, which is much smaller than the typical value of 2.0 GPa for the epoxy able to cure at ambient temperature[6.12)]. Considering the overall trend of property changes along the curing time, a nearly linear increase is found on both Young's modulus and tensile strength, while an exponential decrease is found on the strain at tensile strength of epoxy coupons. It is noted here

that even after 175 days of curing, the epoxy does not fully cured, and the properties continue to change up to at least 250 days as shown in Fig. 6.8. These features of epoxy, the small initial stiffness and strength, and the long curing time, are essential to understand mechanical behavior of CFRP-bonded steel plate specimens fabricated in this study as will be discussed in the following sections.

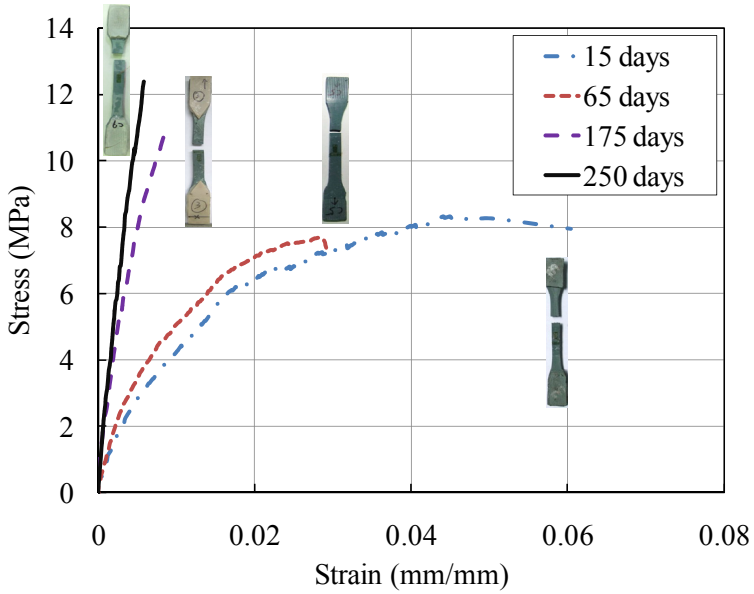

Fig. 6.7 Tensile test curves of epoxy coupons

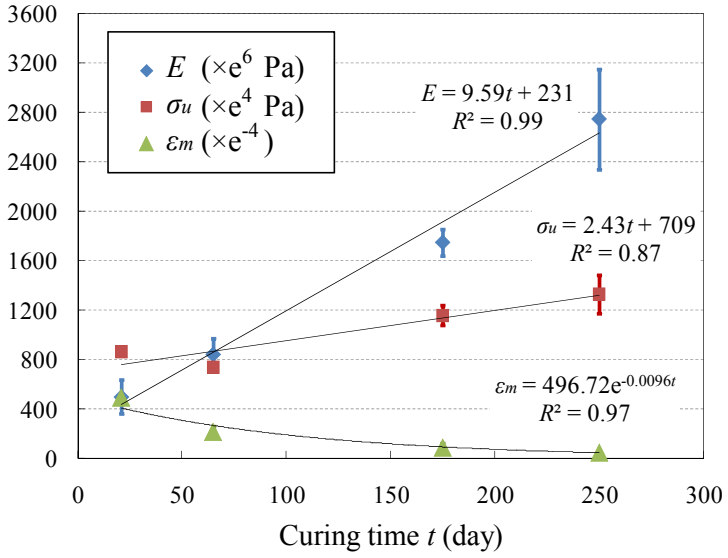

Fig. 6.8 Mechanical properties of epoxy changing with the curing times

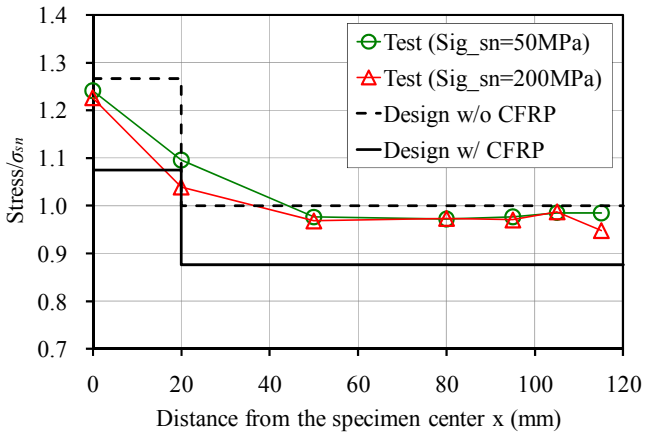

(a) L1T-4

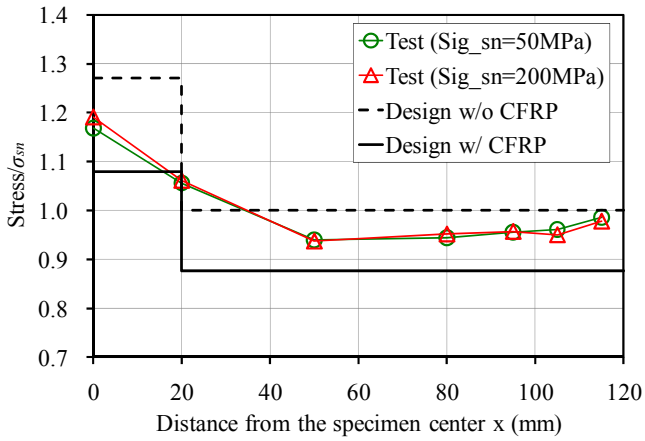

(b) L1C-1

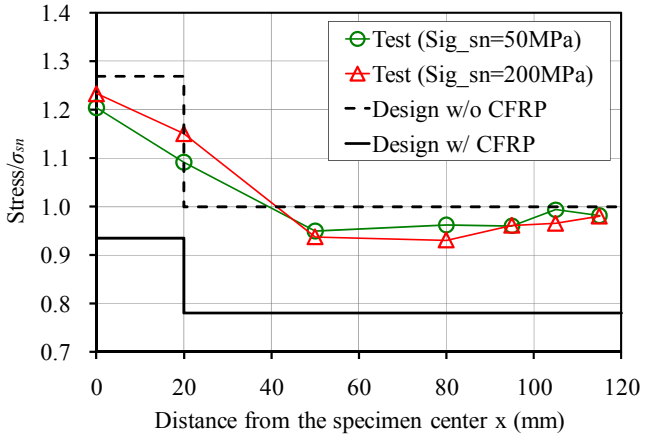

(c) L2T-4

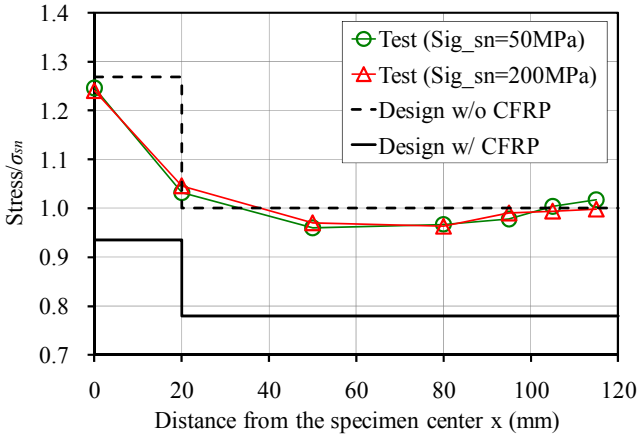

(d) L2C-4

Fig. 6.9 Typical stress distributions in steel

6.3 TEST RESULTS OF CFRP-BONDED STEEL PLATES

6.3.1 Stress and Strain Distributions

Fig. 6.9 shows stress distributions in the steel plate at the two stress levels of σ_{sn} = 50 and 200 MPa, where σ_{sn} is steel stress at the edge of specimen where no CFRP is bonded. The steel plates including the thickness-reduced portions are in the elastic phase at two stress levels. In the figure, stress is normalized by σ_{sn}, therefore, stress distributions are equivalent to the strain distributions as long as steel stress is in the elastic range. In addition, two design values for steel plate with and without CFRP repair are also plotted in Fig. 6.9, where the combined stiffness $EA=E_sA_s+2E_cA_c$ is

used to calculate the design value of stress distributions in the CFRP-bonded steel plate. E_s and A_s, and E_c and A_c are Young's modulus and the cross-sectional area of steel plates and those of CFRP sheets, respectively. The values from material tests and specimen size measurement are used in the calculations.

It can be seen that the stress distributions from the test lie between two design values. This is reasonable because the assumed combined stiffness is achieved only when epoxy adhesive is infinitely stiff. As long as there is shear deformation in the epoxy layer and in the CFRP layer, stresses in steel bonded with CFRP become larger than those of design values. In addition, due to the small stiffness of epoxy adhesive as observed in tensile coupon tests, the tested values are closer to the design values without CFRP repair than those with CFRP. As a result, the second layer of CFRP strand sheet does not improve the repair effect.

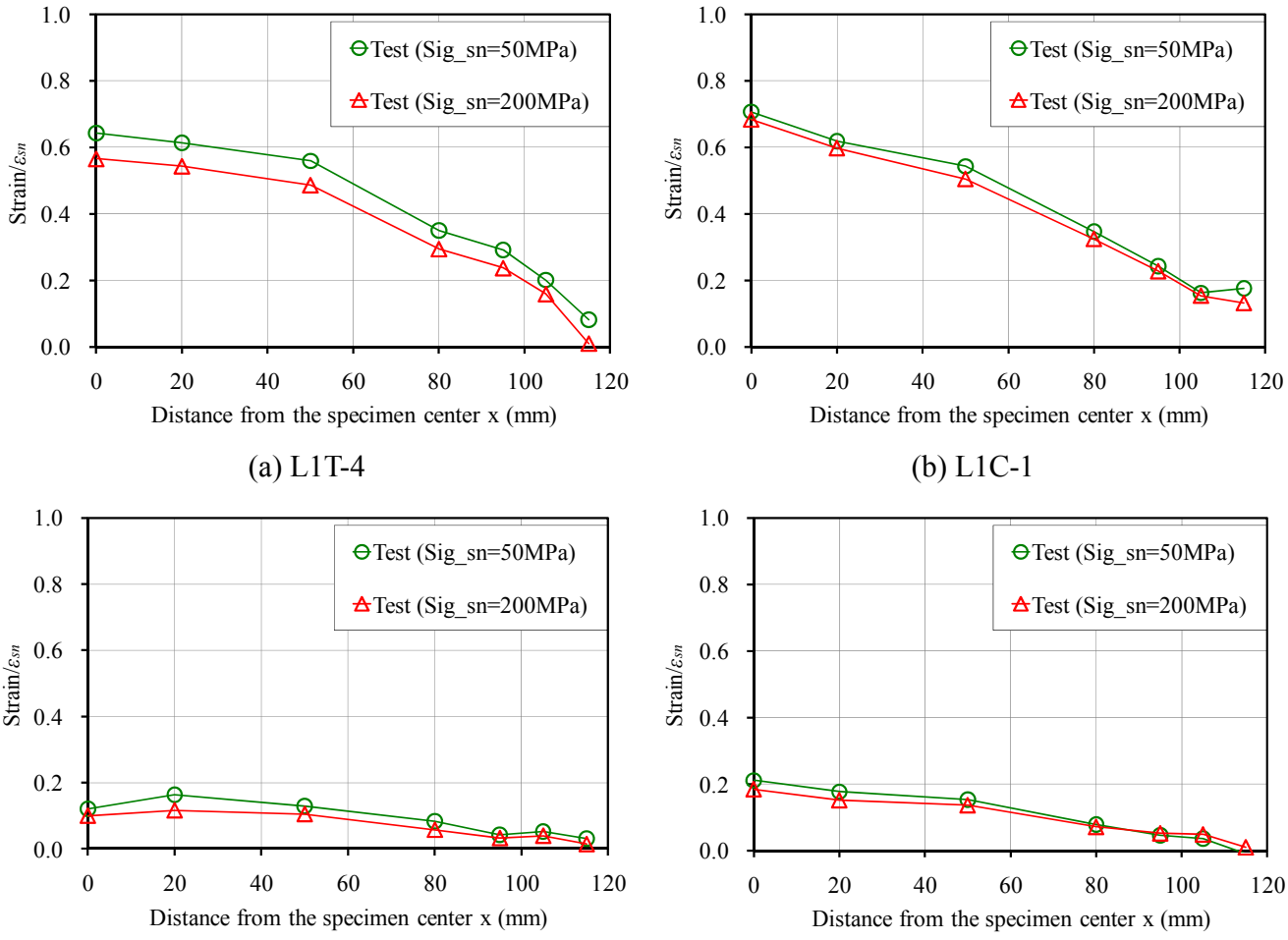

(a) L1T-4 (b) L1C-1

(c) L2T-4 (d) L2C-1

Fig. 6.10 Typical strain distributions in CFRP

Strain distributions at the top of CFRP layers are shown in Fig. 6.10. CFRP strain is the largest at the center of specimens and gradually approaches to zero with the increase of the distance x from the specimen center to the end of CFRP sheet. In addition, it can be observed that the magnitude of strains decreases with the applied stress level. This phenomenon is caused by the material nonlinearity of epoxy adhesive. As shown in Fig. 6.7, the stiffness of epoxy decreases considerably with the applied stress level when the curing time is 21 or 65 days. However, the similar trend is not obvious in the steel strain because the load share of CFRP is not large in the specimens. Moreover, it can be seen that CFRP strains when two layers are used, as shown in Fig. 6.10(c) and (d), are considerably smaller compared to those obtained from one-layer CFRP specimens as shown in Fig. 6.10(a) and (b), implying that the second layer carries insignificant load and does not provide much contribution to share the load.

6.3.2 Repaired Stiffness and Yielding Loads

It is noted that according to the design, the stiffness provided by one CFRP layer and two CFRP layers is equivalent to that provided by the steel plate of 1.3 mm and 2.6 mm's thickness, respectively. Correspondingly, the CFRP-bonded steel plates with 2 mm's thickness reduction at two sides are expected to recover 0.93 and 1.06 times of the stiffness of the virgin steel plates. Repaired performance of CFRP-bonded thickness-reduced steel plate is examined in terms of the initial stiffness and the yielding load. The initial stiffness is defined as 0.7 times of the yielding load of each specimen divided by the corresponding steel strain at the center of specimen. The test results are normalized by the value of one-layer CFRP design as shown in Fig. 6.11. Design values are calculated using the average dimensions of all specimens, and the average values and the standard deviations of the test results from the same set of specimens are plotted.

It can be found in Fig. 6.11(a) that the repaired stiffness does not reach the one-layer design value even in the specimens with two layers of CFRP, and that there is actually no noticeable difference between one and two layers of CFRP, which results from the weak epoxy adhesive as discussed before. It should be noted that in the average sense, the repaired stiffness of steel plates with one CFRP layer is around 0.9 times of the design value, and 1.1 times of the stiffness of the unrepaired steel plates, if the stiffness of the epoxy is increased to a common value of 2 GPa

instead of the current 0.5 GPa as obtained in the coupon tests, the repaired stiffness is expected to be larger than the 0.9 times of the design value.

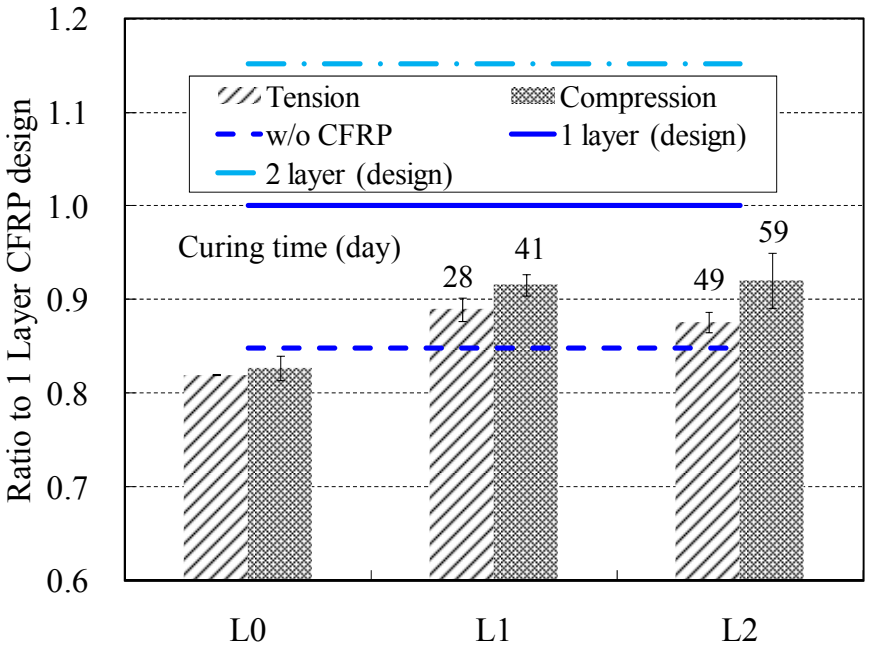

(a) Comparison of repaired stiffness of specimens

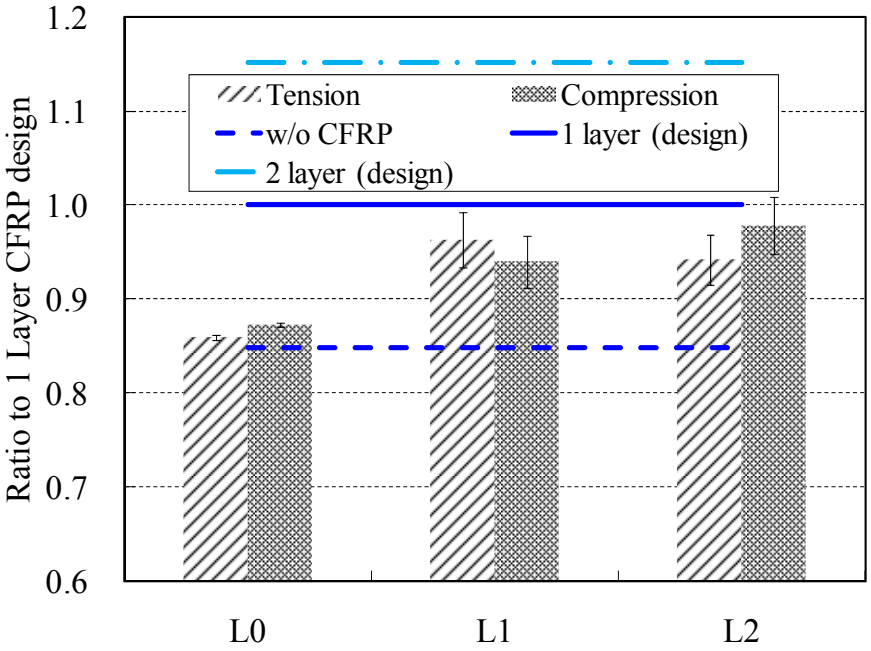

(b) Comparison of yielding loads of specimens

Fig. 6.11 Repaired performance of CFRP-bonded steel plates

It is also observed that the CFRP-bonded specimens tested in compression exhibit the larger repaired stiffness than their counterpart specimens tested in tension. This difference may be caused by the curing effect of epoxy adhesive. Because the specimens are not tested at the same time, and the tensile specimens are tested about two weeks before the compressive specimens. This means that the epoxy adhesive in the compressive specimens is actually cured for a longer time before test and consequently gains larger stiffness, resulting in a larger repaired stiffness. The average curing time of specimens in the same set is indicated in Fig. 6.11(a).

The curing time of specimens with two CFRP layers are generally two weeks longer than that of one CFRP layer specimens. For example, the L2 specimens tested in tension and in compression have an average curing time of 49 and 59 days, respectively. While the corresponding L1 specimens have an average curing time of 28 and 41 days. This difference in the curing time, however, does not cause an obvious increase in the repaired stiffness of L2 specimens compared with L1 specimens. It is suspected that the epoxy adhesive in the two-layer CFRP specimens does not have larger stiffness compared with that in the one-layer CFRP specimens. This finding implies that the epoxy cures more slowly in the two-layer specimens than in the one-layer specimens. This is probably due to the larger thickness of epoxy adhesives in the two-layer specimens. However, in order to draw the conclusion quantitatively, more study is needed on the effect of multiple layers of CFRP on the repaired performance of CFRP-bonded steel plates.

When the attention is paid to the yielding loads of the specimens as shown in Fig. 6.11(b), it is observed that the yielding loads after repair cannot reach the one-layer design value even when two CFRP layers are used. Despite of loading directions and the number of CFRP layers, the yielding loads are around 0.95 times of the design value and 1.1 times of the yielding loads of the unrepaired steel plates. In addition, there is no obvious improvement in the yielding loads when the second CFRP layer is applied to the specimens as the similar observation to that found in the repaired stiffness.

Due to the small stiffness of epoxy adhesive in the CFRP-bonded specimens, the consequent large shear deformation in the epoxy layers impedes the applied load to transfer to CFRP layers and causes the large amount of applied loads to be carried by the steel. Because the yielding of CFRP-bonded specimens is controlled by the yielding of the thickness-reduced steel, smaller

epoxy stiffness would therefore reduce the yielding loads of the CFRP-bonded specimens. On the other hand, if the stiffness of epoxy is larger, the yielding loads would be consequently larger.

It is noted that although both the stiffness and the strength of CFRP under compression loads are usually not expected when the fiber direction is parallel to the loading direction. The specimens using CFRP strand sheets in this study show comparable repaired stiffness and yielding loads regardless of the loading directions. This suggests that there is potential to take account of CFRP strand sheets into the design when they are used in the compression zone of the structures, such as the compressive side of a beam or a column under bending.

6.3.3 Failure Modes

Failure modes of specimens after test are shown in Fig. 6.12. The tensile specimens, regardless of the number of CFRP layers, show a yielding in the thickness-reduced region of steel plate first, which results in the increased relative deformation between steel and CFRP, and eventually the debonding of CFRP sheets. In the compressive test, the yielding in the thickness reduced region also occurs first, and the global buckling follows soon after the yielding of the steel. The out-of-plane bending deformation due to buckling causes the CFRP sheet on the compressive side of bending to rapture at the center of specimens, and the debonding is found to occur in the tensile side of bending if the bending deformation is further increased.

In the tensile specimens, the debonding failure occurs in the epoxy adhesive first, which causes the specimens could not fully utilize the strength of CFRP sheets. While in the compressive specimens, the debonding failure occurs after the rapture of CFRP. This is partly because CFRP in compression has smaller strength than that in tension, and partly because the epoxy in the compressive specimens is stiffer and stronger than that in the tensile specimens due to the longer curing time.

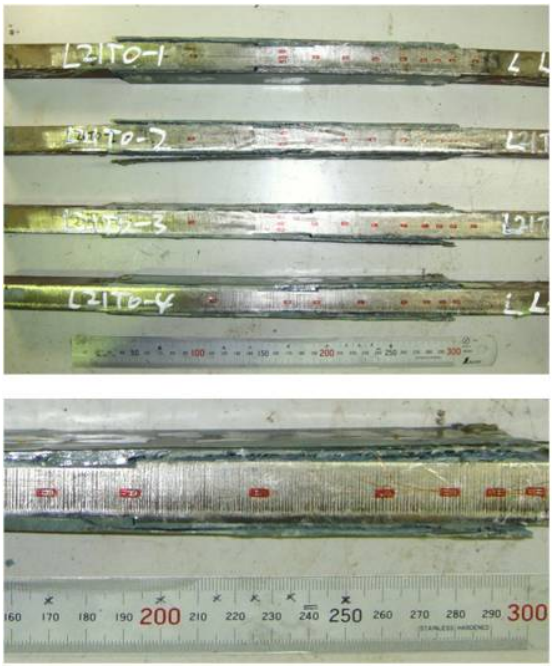

(a) Tension, one CFRP layer (L1-T)

(b) Compression, one CFRP layer (L1-C)

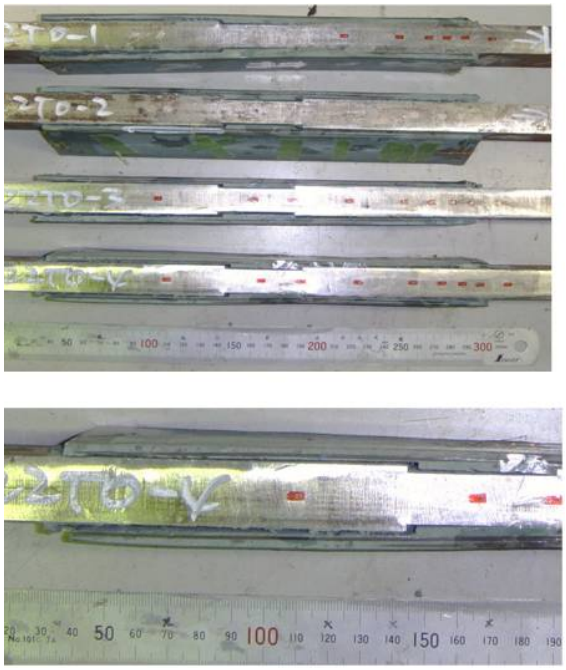

(c) Tension, two CFRP layers (L2-T)

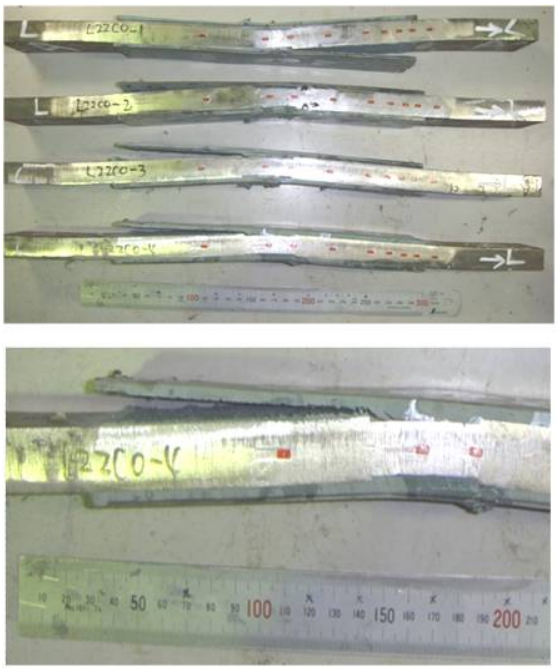

(d) Compression, two CFRP layers (L2-C)

Fig. 6.12 Failure modes of CFRP-bonded steel plates

6.4 CONCLUSIONS

This chapter presents an experimental study on CFRP strand sheet-bonded steel plates using underwater epoxy as adhesive. The repaired performance is examined considering the curing effect of epoxy. It is concluded that:

(1) The curing time necessary for the underwater epoxy used in this experiment is at least 250 days, which is well beyond the curing time of a few days for the ordinary structural epoxy. In addition, the stiffness and the strength of epoxy after 21 days' curing are also smaller than the expected value.

(2) The repaired stiffness and yielding loads of CFRP-bonded steel plates can be recovered to 0.90 and 0.95 times of the design values of one CFRP layer. The repair performance of specimens with two layers of CFRP show the similar performance as those with one-layer of CFRP due to the weak epoxy.

(3) The CFRP strand sheets used in compression, with a fiber direction parallel to the direction of the compressive loads, exhibit comparable contributions to the repaired performance of CFRP-bonded steel plates compared with those used in tension.

In this study, it is found that the epoxy used in the experiment is not suitable for structural repair especially when applying to the emergency repair, where the epoxy is expected to reach the desired stiffness and strength in a short time. When the stiffness and the strength of epoxy adhesives are larger than those presented in this study, the repaired performance of CFRP-bonded steel plates is expected to be larger than the results obtained in the current study. CFRP bonding to steel structures in underwater environment using appropriate epoxy is still possible to provide satisfactory repaired performance.

REFERENCES

6.1) Bakis, C. E., Bank, L. C., Brown, V. L., Cosenza, E., Dayalos, J. F., Lesko, J. J., Machisa, A., Rizkalla, S. H., and Triantafillou, T. C., Fiber-reinforced polymer composites for construction-state-of-the-art review. *Journal of Composites for Construction*, ASCE, 6(2), pp. 73-87, 2002.

6.2) Al-Saidy A. H., Klaiber, F. W., and Wipf, T, J., Repair of steel composite beams with carbon fiber-reinforced polymer plates. *Journal of Composites for Construction*, ASCE, 8(2), pp. 163-173, 2004.

6.3) Bocciarelli, M., Colombi, P., Fava, G., and Poggi. C., Prediction of debonding strength of tensile steel/CFRP joints using fracture mechanics and stress based criteria. *Engineering Structures*, 76, pp. 299-313, 2009.

6.4) Haghani, R., Analysis of adhesive joints used to bond FRP laminates to steel members-a numerical and experimental study. *Construction and Building Materials*, 24, pp. 2243-2251, 2010.

6.5) Ishikawa, T., Okura, I., and Komura, K., Theoretical analysis on increase in debonding load by stepping ends of CFRP strips. *Doboku Gakkai Ronbunshuu A*, JSCE, 65(2), pp. 362-367, 2009(in Japanese).

6.6) Zhao, X.L., and Zhang, L., State-of the art review on FRP strengthened steel structures. *Engineering Structures*, 29, pp. 1808-1823, 2007.

6.7) Abanilla, M. A., Karbhari, V. M., and Li, Y., Interlaminar and intralaminar durability characterization of wet layup carbon/epoxy used in external strengthening. *Composites*, *Part B: Engineering*, 37, pp. 650-661, 2006.

6.8) Abanilla, M. A., Li, Y., and Karbhari, V. M., Durability characterization of wet lay-up carbon/epoxy composites used in external strengthening. *Composites*, *Part B: Engineering*, 37, pp. 200-212, 2006.

6.9) Frigione, M., Aiello, M. A., and Naddeo, C., Water effects on the bond strength of concrete/concrete adhesive joints. *Construction and Building Materials*, 20, pp. 957-970, 2006.

6.10) Frigione, M., Lettieri, M., and Mecchi, A. M., Environmental effects on epoxy adhesives employed for restoration of historical buildings. *Journal of Materials in Civil Engineering*, 18, pp. 715-722, 2006.

6.11) Karbhari, V. M., and Ghosh, K., Comparative durability evaluation of ambient temperature cured externally bonded CFRP and GFRP composite systems for repair of bridges. *Composites*, *Part A*: *Applied Science and Manufacturing*, 40, pp. 1353-1363, 2009.

6.12) Sugiura, H., Kobayashi, A., Ohgaki, K., Inaba, N., Tomita, Y., and Nagai, M., Analytical study on the bonding method of carbon fiber sheets in the repair of corroded steel members. *Doboku Gakkai Ronbunshuu A*, JSCE, 64(4), pp. 806-813, 2008(in Japanese).

CHAPTER 7
CONCLUSIONS

7.1 CONCLUSIONS OF THIS STUDY

Severe corrosive environment threats the safety and durability of offshore and port steel structures. As corrosion damage is inevitable, the proper repair to restore their structural as well as functional performance is an essential work to prevent a possible dangerous situation. To repair corrosion-damaged offshore and port steel structures, underwater wet welding patch is one of the most common methods used in practice. An efficient repair, aiming to fully recover the structural performance with a minimum cost, requires comprehensive understanding of mechanical behavior of wet welds, mechanism of load transfer, as well as the current design provisions. Motivated by the imperative demand from offshore and port engineering industry, this study presented a series of experimental, numerical, and analytical studies towards a cost-effective design method to repair corrosion-damaged steel pipe piles using underwater wet welding technique. In addition, an innovative repair method, CFRP bonding using underwater epoxy, was also examined experimentally as an alternative to the conventional repair method. The main findings of the study are summarized as follow:

Chapter 2 investigated the mechanical properties of underwater wet fillet welds used in the welding repair through tensile test on forty-six fillet welded specimens. Mechanical behavior of wet welds was thoroughly examined in terms of strength, ductility, failure mode. Moreover, the weld profile features, weld defects, hardness distributions, and weld microstructures were also inspected and analyzed to better understand the mechanical properties associated with wet welds. It was concluded that underwater fillet welds have larger strength but smaller ductility than their counterpart in-air welds. Strength increases vary from 6.9% to 41% depending on weld assembly types, while ductility decrease is about 50% for the most weld assemblies. The underwater welds on the corroded SY295 steel show a brittle failure in BOND due to underbead cracks and hardness mismatching in the region. In addition, underwater welds have considerably larger hardness in HAZ, which can be over 500 Hv, than in-air welds, which show the hardness less

than 350 Hv. In addition, the thickness of base plate exhibits little influence on the hardness distribution of underwater welds, which is different from the in-air case.

Chapter 3 proposed two finite element modeling methods to simulate the mechanical behavior of wet fillet welds based on the experimental findings from Chapter 2. It is found that by estimating material properties of welds from Vickers hardness and assuming a uniform cross-section along the weld bead with average dimensions, the maximum load of weld joints can be accurately predicted in the FE analysis for both in-air and underwater welds. Furthermore, a concise weld model by connector elements to be used in the complex structural analysis is constructed and validated. The weld model shows good accuracy to predict the nonlinear behavior and to estimate the failure of fillet welds.

Chapter 4 presented a numerical study to evaluate the current repair design using the proposed weld model in Chapter 3. The welding patch pattern, load share ratio of patch plates, and the effectiveness of transverse welds were investigated. A complementary analytical study was followed according to the design implications obtained from the numerical study. It was found that among different welding patch types, the one with many slits in patch plates and correspondingly short weld lines is a more favorable type for welding repair of pipe piles under compression. The study also pointed out that the current design procedure does not yield a load share ratio expected in the design, and an accurate equation considering the weld stiffness was proposed as:

$$LSR^{(1)} = \frac{1}{1 + \frac{A_b A_r}{A_p} \cdot \frac{l_r + l_{p1} + A_p E / K_w}{A_b l_r + A_r l_{p1}}} \tag{7.1}$$

where,

$LSR^{(1)}$ is the proposed load share ratio of patch plates,

A_b is the cross-sectional area of the intact base steel,

A_r is the cross-sectional area of the thickness-reduced base steel,

A_p is the cross-sectional area of patch plates,

l_r is the half length of the thickness-reduced portion,

l_{pl} is the overlap length of patch plates on the non-reduced pipe pile,

E is the Young's modulus of steels, and

K_w is the total weld stiffness, which can be calculated as:

$$K_{\mathrm{w}} = k_{\mathrm{w0T}} l_{\mathrm{wT}} + k_{\mathrm{w0L}} l_{\mathrm{wL}} \tag{7.2}$$

where, l_{wT} and l_{wL} are the total length of transverse and longitudinal fillet welds, respectively; and k_{w0T} and k_{w0L} are the unit stiffness of the corresponding fillet welds with the values shown in Table 3.1.

Furthermore, the condition to be allowed to neglect the effect of weld stiffness in the calculation of load share ratio was given as follows:

$$\omega = D\left(\frac{l_{\mathrm{r}}}{A_{\mathrm{r}}} + \frac{l_{\mathrm{p1}}}{A_{\mathrm{b}}} + \frac{l_{\mathrm{r}} + l_{\mathrm{p1}}}{A_{\mathrm{p}}}\right) > 20 \tag{7.3}$$

where, D is the outer diameter of the pipe pile.

In addition, the study proved the rightness of the current design manual on the provision that transverse fillet welds are not counted in the calculation of the total weld length in the repair design. Finally, the minimum patch thickness to fully recover the stiffness of corrosion-damaged pipe piles can be calculated as:

$$t_{\mathrm{p}}{}' = \frac{1}{\pi D} \cdot \frac{(l_{\mathrm{r}} + l_{\mathrm{p1}}) A_{\mathrm{b}}}{\dfrac{A_{\mathrm{b}} l_{\mathrm{r}} + A_{\mathrm{r}} l_{\mathrm{p1}}}{A_{\mathrm{b}} - A_{\mathrm{r}}} - \dfrac{E}{K_{\mathrm{w}}} \cdot A_{\mathrm{b}}} \tag{7.4}$$

The maximum number of patch slits can be calculated as:

$$n_{\max} \le \frac{1}{l_{\mathrm{slit0}}} \cdot \left[\pi (D + t_{\mathrm{p}}) - \frac{P_{\mathrm{total}} LSR}{\gamma_{\sigma_{\mathrm{y}}} \sigma_{\mathrm{ypc}} t_{\mathrm{p}}} \right] \tag{7.5}$$

where,

l_{slit0} is the width of one patch slit,

P_{total} is the applied design load,

σ_{ypc} is the characteristic value of yielding stress of patch steel, and

$\gamma_{\sigma\mathrm{y}}$ is standard value of partial factor for materials.

Chapter 5 studied the repaired performance of welding patched pipe piles under compression with emphasis on the effect of the existing axial loads. The necessity of considering the existing loads in the repair was pointed out through a set of finite element analysis. And then, the analytical study was conducted to examine the mechanism of load transfer in the repaired pipe piles. The minimum patch thickness to fully recover the strength of the corrosion-damaged pipe piles was proposed when there are preloads applied to the pipe piles, and it can be calculated as:

$$t_p = \frac{\sigma_{yb}}{\sigma_{yp}} \cdot \Delta t \tag{7.6}$$

where, σ_{yb} and σ_{yp} are yielding stresses of base and patch steel from tensile coupon test, respectively. Δt is the thickness reduction in base pipe.

Integrating the findings obtained in Chapter 4 and Chapter 5, the repair design method to recover the structural performance of the corrosion-damaged pipe piles with the minimum patch thickness and the minimum weld length was proposed. The related issues in the practical use of this method were discussed and the counterpart solutions were also proposed.

Chapter 6 investigated experimentally an innovative method to repair offshore steel structures by CFRP bonding. Four control specimens and sixteen CFRP-bonded steel plates were tested under unidirectional loading. The curing effect of underwater epoxy on the repaired performance was examined. It was found that the epoxy used in the study showed a very long curing time of at least 250 days, and small stiffness about 0.5 GPa after 21 day's curing. The repaired stiffness and yielding loads of CFRP-bonded steel plates can be recovered to 0.90 and 0.95 times of the design values of one CFRP layer. In addition, it was found that the second CFRP layer is not effective to repair the steel plate when epoxy is weak. The CFRP strand sheets used in compression shows comparable contributions to the repaired performance compared with those used in tension. It is also concluded that if the epoxy could provide larger stiffness and strength, the repaired performance of CFRP-bonded steel plates is expected to be larger than the results obtained in the current study.

7.2 FUTURE WORK

As for the further work to supplement the study on the repair methods of corrosion-damaged offshore steel structures, the following directions are considered to be of interest:

(1) This study focused on the unidirectional loading condition of pipe piles and steel plates to be repaired. Since many possible loading conditions exists in the actual structures, the repair method of structural members under monotonic and cyclic bending is necessary. In particular, the repaired performance of welding patched pipe piles under the dynamic actions such as earthquake, wave, and vessel collision is of most concern due to the low ductility of underwater wet welds.

(2) As another type of piles commonly used in offshore steel structures, steel sheet piles have different profiles and usually have a small width of flange, where the use of many slits on patch plates are not possible. The repair method using underwater welding needs to be examined next.

(3) Although corrosion proof measures such as FRP covering are usually provided to pipe piles after welding patch repair, the seawater can still go inside the covers and corrode the base pipe and welds. Because underwater wet welds have martensite microstructures, which are susceptible to corrosion[7.1)], the long-term performance of wet welds exposed to seawater needs to be assessed.

(4) The epoxy used in this study is found to cure too slowly to be used in practical applications. Because epoxy adhesive is the essential part in the repaired system in charge of load transfer, the proper epoxy that can cure underwater in a short time and provide sufficient bond stiffness and strength is the key to the success of CFRP bonding repair. The study on mechanical properties of the epoxy under seawater environment remains as further work to repair offshore steel structures efficiently.

REFERENCES

7.1) Sarkar, P. P., Kumar, P., Manna, K. M., and Chakraborti P. C., Microstructural influence on the electrochemical corrosion behavior of dual-phase steels in 3.5% NaCl solution. *Materials Letters*, 59, pp. 2488-2491, 2005.